Design and control of lightweight, active space mirrors

by

Dave Baiocchi

A Dissertation Submitted to the Faculty of the

Department of Optical Sciences

In Partial Fulfillment of the Requirements
For the Degree of

Doctor of Philosophy

In the Graduate College

The University of Arizona

2 0 0 4

Get the official approval page
from the Graduate College
before your final defense.

Statement by Author

Signed: ________________________________

Acknowledgments

Several individuals have contributed to the success of this work. Brian Cuerden (Steward Observatory), opto-mechanical engineer extraordinare, has endured a lot of painful conversations over the past six years while he tried to explain the basics of mechanical and thermal analysis. Ralph M. Richard (Optical Sciences Center) provided some key insights on using unit cells to represent structured mirrors. Norm Schenk, Bob Crawford, and Marty Valente (Optical Sciences Center) were always helpful in the matters of machining, tinkering, and general scavenging; in particular, Bob always had nice things to say about my hair. Charles Burkhart (Optical Sciences Center) patiently taught me clever tricks whenever I was in the machine shop, even though it was always obvious that there were more important things that he should be doing. Brian Stamper is a jack-of-all-trades: mechanical engineer, photography model, LaTeX wrangler, and technical accomplice for several of my whiz-bang ideas. Iwonka Palusinski (Aerospace Corporation) provided helpful information about the current status of SiC mirrors.

Buddy Martin spent several days reading the manuscript, re-deriving the results, and working through all of the examples. Every student should be so lucky as to have a thorough, patient editor on his dissertation committee.

Jim Burge has proved to be an excellent mentor for the past six years. His scary finger-tip knowledge of optics and his approachable personality make him a pleasure to work with. Watching him take down the large ego-ed engineer whenever we attended meetings together is something that I loved to witness. (And I'm going to miss this very much.) I am very thankful to have worked in such a productive partnership.

Dan G. Smith carries a wealth of scientific knowledge about in his well-coiffed head, and he was kind enough to share portions of it with me during my stay at Optical Sciences. In addition to this, he proved to be an excellent conversationalist, adventure-seeker, beer drinker, and best friend.

Finally, my mom may have been under the [mistaken] impression that the late-night phone calls about my insecurities, fears, career plans, and personal victories, should have ended upon graduating with my *previous* degree in 1998. Lucky for us, this was not the case. How do you thank someone who is so generous and thankless with her time and support? Thanks, Mom.

This document was composed on an Apple PowerBook G4, and it was typeset using LaTeX. All of the illustrations were drawn in Adobe Illustrator unless noted otherwise. All of the illustrations and images used in this dissertation are in color. A color copy is available in the Optical Sciences Center Library (1630 E. University Blvd, Tucson AZ 85721) or from the author.

Dave Baiocchi (`bi-O-key`)
August 2004, Tucson AZ

Table of Contents

Table of Contents—*Continued*

Table of Contents—*Continued*

List of Figures

List of Figures—*Continued*

List of Figures—*Continued*

List of Figures—*Continued*

List of Figures—*Continued*

List of Figures—*Continued*

List of Figures—*Continued*

List of Tables

Abstract

The success of the Hubble Space Telescope created a great interest in the next generation of space telescopes. To address this need, the University of Arizona (UA) has designed and built several lightweight prototype mirrors ranging in size from 0.5 m to 2 m in diameter. These mirrors consist of three key components: a thin, lightweight glass substrate holds the reflective surface; the surface accuracy is maintained by an array of position actuators; and the stiffness is maintained by a lightweight carbon-fiber/epoxy support structure. The UA mirrors are different from conventional mirrors in that they are actively-controlled: their figure may be changed after they leave the optics shop.

This dissertation begins with an overview of the technical issues for placing large optics in space, and I also discuss the current state-of-the-art in active mirror design. Chapters 3 and 4 discuss ways to design mirrors such that the optical performance is maximized while the mass is minimized. Chapter 3 looks at the best way to distribute the mass between the reflective substrate and the actuators, and Chapter 4 looks at the optimum geometries for structured mirrors.

The second half of this work looks at the practical aspects of controlling active mirrors. Chapter 5 discusses the University of Arizona's 2 m NMSD prototype mirror. Specifically, I review the system that I developed to measure and control the mirror. I also provide some details on using a least-squares solution to solve for the actuator commands. Chapter 6 discusses the UA ultralightweight 0.5 m prototype mirror. I describe the techniques that I developed for attaching loadspreaders to the reflective surface, the metrology system, and a software package used to remotely-control the mirror.

Design and control of lightweight, active space mirrors

Dave Baiocchi, Ph.D.
The University of Arizona, 2004

Director: J. H. Burge

The success of the Hubble Space Telescope created a great interest in the next generation of space telescopes. To address this need, the University of Arizona (UA) has designed and built several lightweight prototype mirrors ranging in size from 0.5 m to 2 m in diameter. These mirrors consist of three key components: a thin, lightweight glass substrate holds the reflective surface; the surface accuracy is maintained by an array of position actuators; and the stiffness is maintained by a lightweight carbon-fiber/epoxy support structure. The UA mirrors are different from conventional mirrors in that they are actively-controlled: their figure may be changed after they leave the optics shop.

This dissertation begins with an overview of the technical issues for placing large optics in space, and I also discuss the current state-of-the-art in active mirror design. Chapters 3 and 4 discuss ways to design mirrors such that the optical performance is maximized while the mass is minimized. Chapter 3 looks at the best way to distribute the mass between the reflective substrate and the actuators, and Chapter 4 looks at the optimum geometries for structured mirrors.

The second half of this work looks at the practical aspects of controlling active mirrors. Chapter 5 discusses the University of Arizona's 2 m NMSD prototype mirror. Specifically, I review the system that I developed to measure and control the mirror. I also provide some details on using a least-squares solution to solve for the actuator commands. Chapter 6 discusses the UA ultralightweight 0.5 m prototype mirror. I describe the techniques that I developed for attaching loadspreaders to the reflective

surface, the metrology system, and a software package used to remotely-control the mirror.

Chapter 1

Introduction

1946 was a big year for space optics. Elsewhere in the world, World War II had just ended, and the United States was poised to become a superpower. The birthrate in America would increase by 15% over the previous year, officially starting the Baby Boom. Meanwhile, the important optics contribution would come from Princeton University: while working in the astronomy department, Lyman Spitzer proposed using a telescope in space. He noted that an on-orbit telescope would result in increased resolution and stability. At the time, the idea must have seemed outlandish: the United States was still sixteen years away from putting *anything* in space, let alone a telescope. Spitzer's vision persevered through the next several decades, and forty five years later NASA launched the Hubble Space Telescope (HST) in 1990.

The HST has proven to be a major public relations coup for both NASA and the US space program at large. Few Americans realize how many thousands of technical satellites are currently orbiting the Earth, but the Hubble is certainly one of the most familiar. The HST has changed the way we view ourselves in the universe. The HST has provided evidence that the universe is accelerating, and this has reshaped the way that scientists view the composition of the universe.[1]

[1] If the universe is accelerating, then Einstein was correct when he suggested that some other, previously-undiscovered form of energy must exist. Einstein proposed using a "cosmological constant" to account for this energy, but he later referred to this idea as his greatest scientific blunder. Recent results from the HST suggest that such dark energy exists.

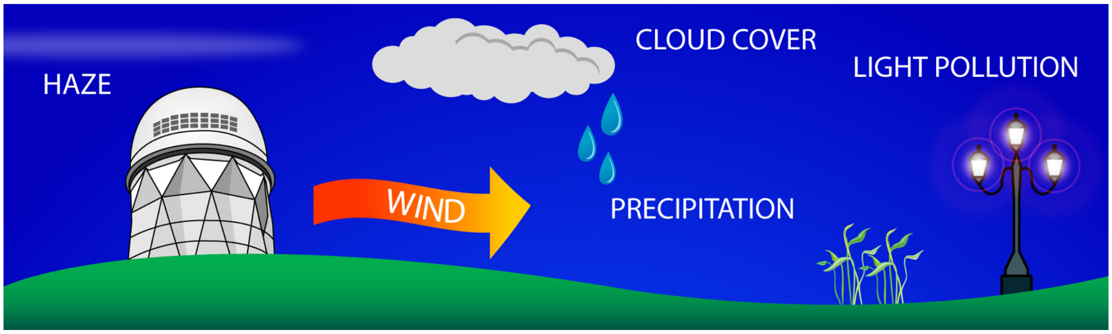

FIGURE 1.1. The hazards of working under an atmosphere. Weather is a significant concern: if there is cloud cover, the telescope cannot be used at most wavelengths. Wind is also a factor. Breezy conditions near the ground cause instability of the telescope structure and enclosure. There are also turbulent layers above the ground, and this will affect the imaging performance. The atmosphere also reflects some of the man-made light back to Earth, compounding the effect of light pollution.

1.1 Why space?

There are several reasons why space is an excellent place for a telescope. First and foremost, the instrument is above the Earth's atmosphere, and the atmosphere is the source of several concerns. The biggest issue is atmospheric absorption over portions of the near infrared spectrum. If an astronomer is looking for something that has a wavelength in one of these absorption bands, the visibility of this object will be very poor. The atmosphere also contains the weather, as illustrated in Figure 1.1. Ground telescopes suffer from reduced visibility during weather events like clouds, precipitation, and high winds. In addition to the weather, the atmoshere contains turbulent wind layers that degrade the image quality.[2] Modern ground-based telescopes are currently using adaptive optics (AO) systems to subtract this effect, but these systems are expensive: there are currently only a handful of telescopes that use AO to any degree of success.

[2]You don't have to be an astronomer to appreciate this effect. If you look across town on a clear night, the city lights appear to twinkle. The atmosphere causes a varying index of refraction across the horizon.

On Earth, most telescopes are used at night, but the idea of night and day is effectively meaningless in space. Depending on where the telescope is placed and what it's pointed at, the user can get more than the eight hours of viewing that he would get on Earth. This results in a more efficient use of the instrument: the ratio of science information gained per day is higher for a space telescope.

One of the biggest concerns in constructing modern-day ground-based telescopes is selecting a location. Ideally, the location should have good seeing[3] and little light pollution. Environmental concerns are also a big factor in selecting a location for telescopes built in the United States. Many of the potential sites that fit all of the criteria are located in pristine forest or in sensitive environments. Putting a telescope in space bypasses these concerns.

1.2 The challenges of putting large optics in space

There are several concerns that must be addressed when putting large optics into space.[4] First, the launch vehicle limits the payload in two ways, and this is illustrated in Figure 1.2. The United States has an existing fleet of rockets used to carry technical payloads into orbit, and one of these vehicles must be used for launching a space telescope: NASA isn't going to design and build new rockets for this purpose. Thus, the telescope must fit within the payload shroud for the current selection of launch vehicles. Most current vehicles have a payload faring of four or five meters. Notice that this is the total *payload* diameter: this includes both the telescope's primary mirror and the rest of the satellite that surrounds it. Finally, the engines attached to a particular rocket limit the payload's mass. Thus, the launch vehicle places an

[3]While it may look like a non-scientific term, "seeing" is a technical word. It refers to the optical quality of the column of air that a telescope must image through to see the stars. A telescope site with "good seeing" means that the atmospheric turbulence above the site is small compared to other locations on Earth.

[4]Within the context of this discussion, a "large" optic constitutes anything 0.5 meters (20") in diameter or larger.

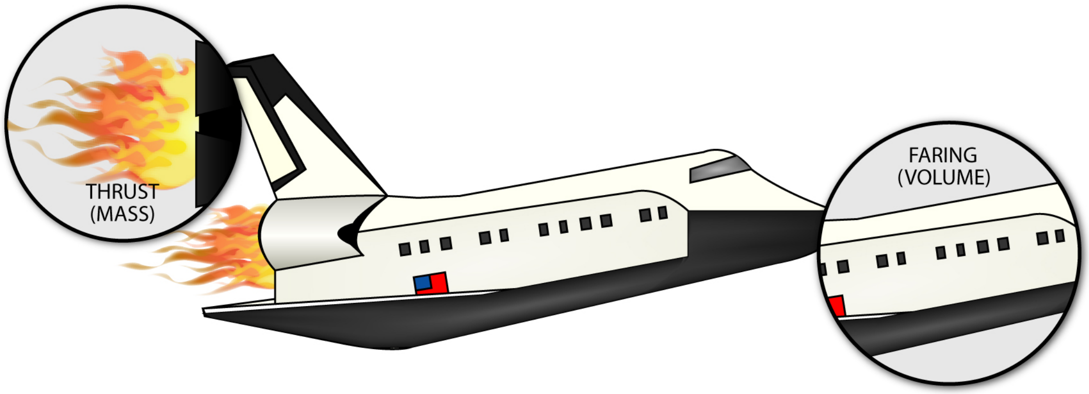

FIGURE 1.2. Limitations of putting large optics in space, using the Space Shuttle as an example. The launch vehicle limits the payload's size in two ways. The rocket(s) have a limited amount of thrust, and this will put an upper limit on the payload's mass. The vehicle's payload bay is a particular size, and this puts an upper limit on the payload's volume.

upper bound on the payload's mass and volume.

The journey, itself, is also a concern for putting large optics into space. The ride up through the atmosphere is rough: the payload must be able to survive the journey into orbit. In addition to this, space is potentially a harsh environment to work in. Depending on whether or not the satellite spends time in direct sunlight, the payload can experience temperature swings of tens of degrees. As a result, the materials for both the optics and the metering structure must be chosen appropriately such that their materials properties (i.e. coefficient of thermal expansion) match.

1.3 The University of Arizona MARS mirror design

1.3.1 Conventional optics

Conventional telescope mirrors are made from thick, heavy plates of glass. This is because the substrate[5] serves two purposes: it supports the reflective coating (often

[5]Throughout this work, I will use the terms "facesheet", "substrate", and "reflective surface" interchangeably. The word "substrate" is appropriate because the glass only serves as a *support* for

only a few hundred atoms thick), and it also serves as the structural support. For a solid plate, the bending stiffness goes as the cube of the plate thickness, so there is a significant advantage to be gained by making an optic thicker. Conventional mirrors are also passive: the figure that is applied in the optics shop is the figure the mirror will have for the rest of its life. This is another reason why conventional mirrors are thick: because the figure is permanent, it is advantageous that they be stiff, rigid structures.

Modern ground-based telescopes use passive mirrors with active supports. The passive mirror with an active support uses the support to remove errors with large spatial scales. For example, the Multiple Mirror Telescope's primary on Mt. Hopkins is 6.5 m in diameter, and it's supported by 160 actuators. These actuators can't correct for errors on the order of a few inches: they're spaced too far apart to do this. Instead, they are used to correct for gross astigmatism or trefoil caused by self-weight or wind loading.[6]

Conventional mirrors have an advantage in that they have a significant legacy in mirror fabrication. Opticians have been making conventional passive mirrors for over one hundred years, and the processes and tooling are well understood, standardized, and readily available. This means that conventional mirrors usually don't require complicated new tooling or additional research, and this is an important consideration for ground-based telescopes.[7]

---

the reflective coating. (The glass, by itself, doesn't reflect much light. The reflective coating is the real mirror.)

[6]There is a distinction between an active mirror and a passive mirror with an active support. An active mirror generally has more control over its surface: it has the ability to correct errors over a smaller spatial period. (This is referred to as a "high authority" mirror.) Passive mirrors tend to be a lot thicker, and this makes them harder to control over smaller spatial periods.

[7]The Hubble's primary is a lightweighted conventional mirror. It was made by taking three components of ULE and fusing them together at a high temperature. The Hubble's primary is basically a giant sandwich: there is a facesheet and a backsheet that surround a series of ribs in between.

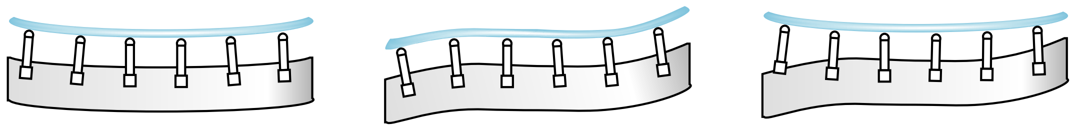

FIGURE 1.3. Left: The University of Arizona MARS mirror design. The mirror consists of three key components: a thin, glass facesheet serves as a reflective substrate; the surface accuracy is maintained by an array of actuators; and the stiffness is maintained by a lightweight, carbon-fiber and epoxy support structure. Middle: The added advantage of using an active mirror design. If the structure should deform for some reason (due to temperature effects, for example), the glass facesheet will deform, too. Right: This error is readily corrected using the actuators.

1.3.2 The MARS design: a Membrane with Active Rigid Support

The University of Arizona has been working on a mirror concept for the past ten years that satisfies all of the concerns discussed in the previous section.[8] The design replaces the use of a single, monolithic piece of glass with an entirely active design that has three key components, Figure 1.3. The substrate that will eventually receive the reflective coating is still made from glass, but instead of being several inches thick (in the case of the Hubble's primary) it is only a few millimeters thick. However, because the glass is so thin, it is also very flexible. As a result, the substrate is mounted on an array of position actuators. These are little motors that have the ability to move up and down to correct the substrate's surface figure. Finally, the system stiffness is maintained by a lightweight support structure (sometimes called a *reaction structure*) that is generally made from a carbon-fiber/epoxy composite material. Together, these three elements make up the Univ. of Arizona lightweight "MARS" mirror design: Membrane with Active Rigid Support.

The design details of the support structure and the actuator mechanics are mostly a mechanical problem, and therefore they will not be discussed in great detail. For

[8] The University of Arizona got into the space mirror business because of their work in adaptive secondary mirrors for ground-based telescopes. The MARS design is basically a lightweighted version of an adaptive secondary mirror.

FIGURE 1.4. Actuator spacing and error correction. Left: if errors occur within the actuator spacing, they cannot be fixed. Right: errors with periods twice that of the actuator spacing (and larger) can be removed.

example, the geometry of the support structure is based entirely on the system's dynamic mechanical requirements (i.e. resonant frequency properties). These issues are worked out by mechanical engineers.

The layout of the actuator geometry is an important consideration, and the design details of this are discussed in Chapter 3. For the time being, it's important to point out that errors in the mirror can only be removed if they are on spatial scales greater than twice the actuator spacing, Figure 1.4. For example, the left side of Figure 1.4 shows a surface error with a period smaller than the actuator spacing. This error cannot be removed using the actuators.

1.3.3 The original MARS prototype mirrors

The initial MARS mirrors were three identical, half meter prototypes [1] built as a proof-of-concept for NASA in 1997, Figure 1.5. The mirrors contained all of the three key components described in the previous section. The glass facesheet was 53 cm in diameter and 2.1 mm thick. It was fabricated from a Zerodur[9] disk, and the final mass of the substrate was 1.25 kg.

New Focus Picomotors were chosen as the actuators for these mirrors. The Picomotors each had a mass of 40 g, and they used an 80 pitch screw as the actuator. Picomotors are driven via cylindrical piezo-electric[10] stacks: they move in discrete

[9]Zerodur is a glass/ceramic that has a very low coefficient of thermal expansion.
[10]A piezo-electric material is one that changes linear shape when a voltage is applied.

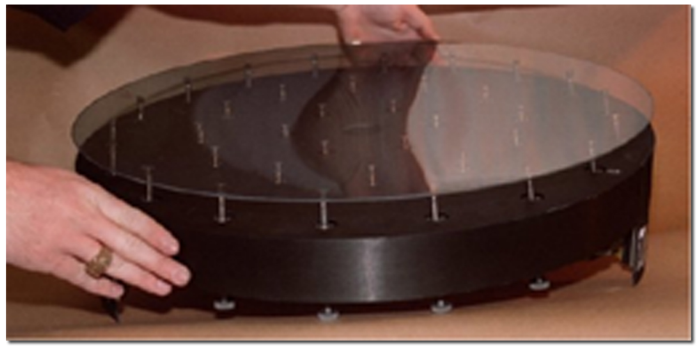

FIGURE 1.5. The original MARS mirror, circa 1997. All three components of the active mirror design are clearly illustrated in this picture: the [uncoated] glass substrate, the composite support structure, and the New Focus Picomotor actuators. This now-famous picture illustrates a curious phenomenon in prototype engineering: some pictures casually taken as snapshots end up becoming ubiquitous. If Phil Hinz had known this, do you think he would have worn a ring that day?

steps of 30 nm with very little hysteresis.

The support structure was made from a carbon-fiber/epoxy composite material. It was designed at the Univ. of Arizona and fabricated at Composite Optics, Inc. in San Diego. This particular support structure was 53 cm in diameter and 4 cm thick. The facesheets are 1 mm thick, and the internal portion of the structure was composed of tangetial and radial ribs. The mass of the support structure was 2.0 kg, and the entire assembly (including the actuators and the support structure) was 4.73 kg.

The mirror's surface quality was measured using visible interferometry . The resulting surface was 53 nm rms ($\lambda/11$ at HeNe), Figure 1.6. The bumps in the surface are the result of gravity: the glass membrane is so thin that it slumps about all of the support points. In space, gravity doesn't exist, and this effect would not be as dominant. The effective surface error in the absence of gravity was calculated to be 33 nm.

The original MARS mirrors were successful on several fronts. First, they proved that the lightweight design was feasible and that it could be successfully fabricated.

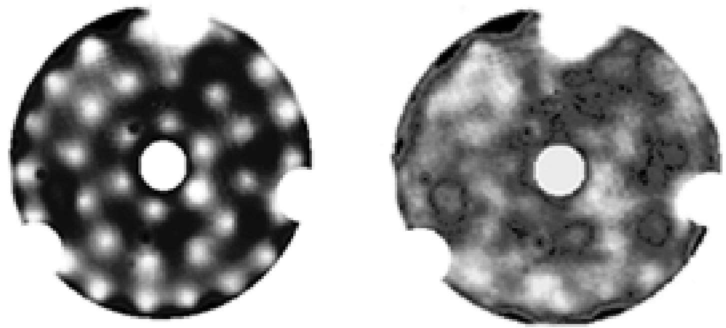

FIGURE 1.6. The final surface map for the original MARS mirror. Left: gravity-limited surface figure (53 nm rms). The glass is so thin that it slumps about the support points, and this is what causes the bumps shown in the figure. Right: predicted surface in a zero-gravity environment (33 nm rms). The missing portions of data were masked out during data reduction. Due to a tooling error, these portions of the mirror exhibited unusually high errors. This systematic error was corrected in future mirrors.

The following results are the important technical conclusions that came out of this project:

- Zerodur, the material used for the facesheet, exhibited low internal stress, and it was a good material for this application. There was also very little residual stress due to the fabrication process.

- The prototype used magnets as the interface between the actuators and the facesheet. This was done for two reasons. First, it allowed the actuators to exert a small downward force of 1.5 N (five times the local self-weight on each actuator). It also allowed for a fail safe method in case one actuator was extended too far: if this happened, the surrounding magnets would release from their actuators and the facesheet would not be damaged. The prototype showed that this interface scheme worked well, with "little evidence [of] parasitic forces from bending moments or lateral friction." [1]

- The prototype met the design goal of being light enough for the next generation of space telescopes. The areal density of these mirrors was 21 kg/m^2. By comparison, the Hubble's primary mirror has an areal density of 180 kg/m^2.

- This 0.5 m prototype was a success, but the fabrication team realized that scaling the mirror up to the next larger size (meter class) would represent a significant challenge.

1.3.4 The 2 m NGST demonstration mirror

After the success of the 0.5 m prototype, the Arizona team looked into building a larger prototype, and the two meter, NGST[11] demonstration was the result. A cartoon of the mirror is shown in Figure 1.7. This mirror is basically a larger, advanced version of the 0.5 m prototypes that were discussed in the previous section. The glass facesheet is 2 mm thick and 2 m in diameter. The facesheet is supported by 166 actuators, and nine-point loadspreaders are used to interface the glass with the actuators. The loadspreaders are used to spread the influence function out over a larger surface area. The reaction structure is made from a carbon-fiber/epoxy composite material.

Although the 2 m is significantly larger than the 0.5 m prototype, it is also significantly less massive. The areal density of the 2 m is 13 kg/m^2, nearly half that of the original protoype. In fact, the total mass (including the glass, the actuators, the loadspreaders, the support structure, and all of the on-board wiring) is 39 kg (86 lbs on Earth).

The 2 m prototype was a major technical undertaking at the University of Arizona, and the details of the metrology schemes used to measure and actuate the mirror are discussed in Chapter 5.

[11]Next Generation Space Telescope. The NGST has since been renamed the James Webb Space Telescope.

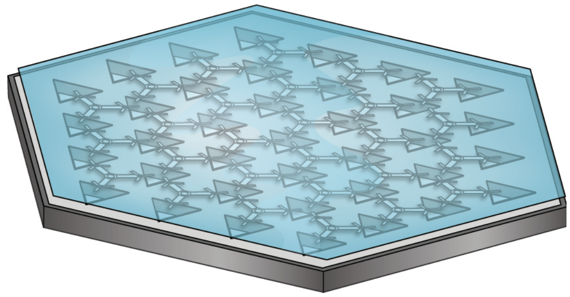

FIGURE 1.7. The 2 m NGST demonstration mirror. The glass facesheet is 2 mm thick and 2 m in diameter. The glass is supported by 166 actuators that are each coupled to the glass via a nine-point loadspreader. The support structure is made from a carbon-fiber/epoxy composite.

1.3.5 The ultralightweight half-meter mirror

The ultralightweight half-meter mirror arose from the need for a mirror technology that was light enough to be used at geosynchronous orbit. Geosynchronous orbit is ideal for Earth-imaging because the satellite remains fixed over a particular location on the ground. The Earth-imaging community has determined that a successful geosync mirror technology must have an areal density of 5 kg/m^2. Based on this determination, the 2 m demonstration discussed in the previous section is not light enough for this task. Thus, the ultralightweight prototype is a super lightweighted version of 2 m demonstration mirror.

A cartoon of this prototype is shown in Figure 1.8. The glass facesheet is 1 mm thick and 2 m in diameter. The facesheet is supported by 31 actuators, and three point aluminum loadspreaders are used to interface the glass with the actuators. Again, the reaction structure is made from a carbon-fiber/epoxy composite material.

The half meter ultralightweight prototype was a very successful project, and the details of its integration and system testing are described in detail in Chapter 6.

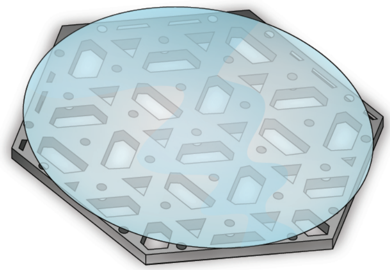

FIGURE 1.8. The 0.5 m ultralightweight demonstration mirror. The glass facesheet is 1 mm thick and 0.5 m in diameter. The glass is supported by 31 actuators that are each coupled to the glass via a three-point aluminum loadspreader. As with the other MARS mirrors, the support structure is made from a carbon-fiber/epoxy composite. Unlike the other mirrors, the support structure was aggressively lightweighted.

1.4 The next generation of space telescopes

The technology demonstrated in Arizona's recent prototype mirrors are designed for use in the next generation of space telescopes. Future missions have ambitious science goals, and they will require much lighter mirrors than what is currently available.

For example, the James Webb Space Telescope (JWST) is being designed to replace the aging Hubble at the end of the decade.[12] The HST was only designed to last for five years, but recent service missions have stretched its useful lifetime out to eighteen years. Eventually, the HST will be brought offline, and the JWST will start answering the next set of science questions.

The James Webb is an ambitious project. The planned aperture is 6 meters in diameter, with a projected areal density of roughly 25 kg/m^2. The primary mirror will consist of eighteen 1.2 m segments made of beryllium. (Beryllium mirrors are discussed along with other competing mirror technologies in Section 1.4.1.)

The science goals of JWST will be different than for Hubble. First, the Hubble's four instruments cover a spectral range from 115 nm to 2.5 microns. By contrast, the Webb will observe over a much larger range of wavelengths: 0.6 to 28 microns. The

[12] A launch date of August 2011 is currently scheduled.

Webb's larger aperture and spectral range will be used to observe the first stars and galaxies created in the universe. To do this, the Webb must be able to detect objects 400 times fainter than those seen with the largest ground-based telescopes (Keck and Gemini) and yet still maintain the same spatial resolution as the Hubble.

The other major telescope mission[13] is the Terrestrial Planet Finder (TPF). Astronomers currently have strong evidence suggesting that Earth-like planets exist within the universe, but they have yet to directly observe these planets. TPF will be a telescope designed to directly image these extra-solar planets.

Imaging these extra-solar planets is difficult because the planets are orbiting nearby stars, and the stars are several orders of magnitude brighter than the planets. In fact, astronomers estimate that the optical systems needed to image these planets must be able to distinguish contrast to a part in 10^{10}!

At the present date, two competing designs exist for TPF, and both are being studied at the Jet Propulsion Lab in Pasadena CA. One scheme consists of using a coronagraph and a 4 m class telescope to physically block the light from the adjacent star. A coronagraph uses a physical mask to block the light coming from the star with the hopes that the planet will then be detectable in the star's corona. The other scheme uses a proposed space interferometer with 3.5 m class apertures along a 20 meter baseline. An interferometer takes advantage of the wave-like nature of light to destructively interfere light. If this destructive interference occurs where the star is, perhaps the light from the planet can be detected in the neighboring constructive bands. Regardless of which design is ultimately selected, one fact will remain: TPF will require a 4 m class space optic.

Figure 1.9 shows the progression of areal densities for recent telescopes and planned missions. Notice that the future missions (labeled in green) demand that the pro-

[13]There are plenty of planned telescopes on the horizon. However, these "major" missions have the following things in common: NASA has invested heavily in their enabling technologies; they have very ambitious science and technology goals; and they have scheduled launch dates on the calendar.

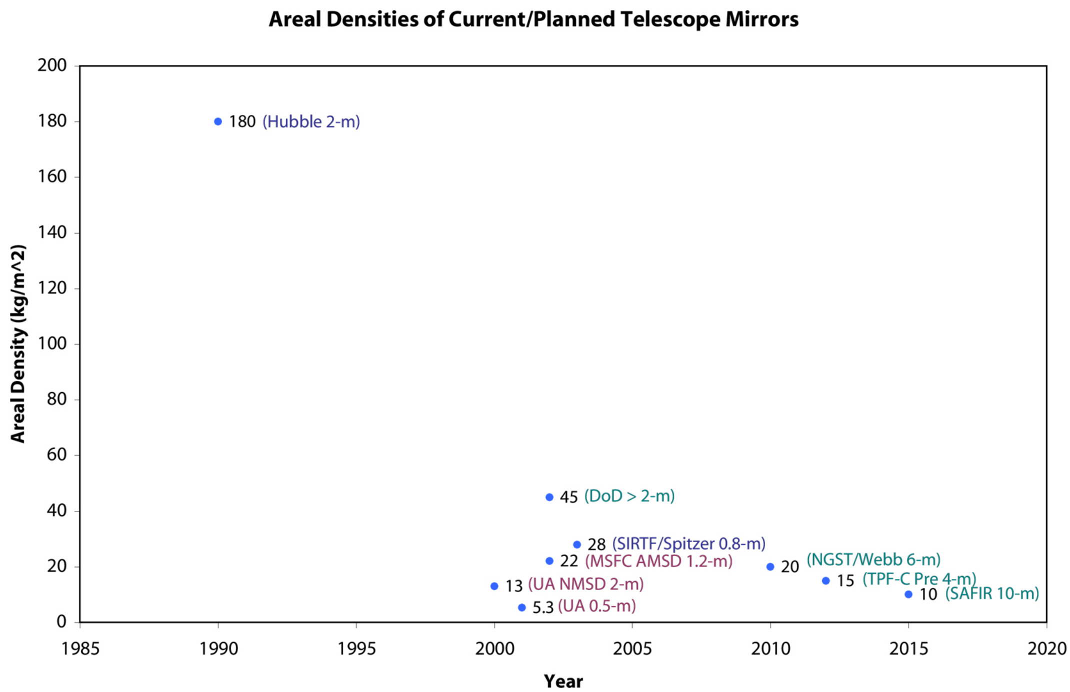

FIGURE 1.9. Areal densities for current and planned telescopes. Notice the negative exponential curve as the years progress. Launched telescopes are labeled in blue; successful technology demonstrations (prototypes) are labeled in violet; and planned missions are shown in green.

gression started by Hubble and the Spitzer[14] continue along a negative exponential trend. Recent prototype mirrors (shown in plum) developed by NASA and the Univ. of Arizona meet the design goals, but these mirrors are not flight-ready. In addition to this, the future missions require apertures that are much larger than the current state of the art.

Clearly, there is a great desire within the astronomical community to improve the current technology of space optics. The success of these future missions depend on the optical community's ability to fabricate larger and lighter mirrors.

[14]The last of NASA's Great Observatories to be launched, the telescope was placed on orbit on 24 August 2003.

1.4.1 Competing technologies

The Arizona MARS design isn't the only lightweight mirror technology available for future space telescopes. Several other competing technologies exist, and they are summarized below.

Beryllium Beryllium (Be) mirrors are similar in construction to the Arizona MARS design, except that Be is used as the mirror substrate. However, fewer actuators are necessary because Be is much stiffer than glass. Beryllium's biggest advantage as a mirror substrate is its specific stiffness. Specific stiffness is defined as E/ρ, where E is Young's modulus[15] and ρ is the mass density (m/V). Ideally, lightweight mirrors should be constructed from something that has a large E (takes lots of stress with little strain) and a low density (lightweight for its size). Thus, large values of specific stiffness are ideal for building lightweight, stiff mirrors. Figure 1.10 shows the density and Young's modulus for several common materials. Beryllium stands by itself on the lower right-hand corner of the chart. Beryllium is one of the stiffest, lightest materials that mirror-making money can buy. For example, the specific stiffness for Be is over five times that of optical glass (BK7), yet it is 27% less dense than glass.

Beryllium is, on paper, an ideal material for mirror construction. There are, however, some important disadvantages to using Be. First, because the material is so stiff, it is very time-consuming to polish. Be has a very low yield stress: unlike spring steel, Be cannot be stressed very much before it does not spring back to its initial shape. Also, the particulate form of Be is toxic, so it must be polished in special, controlled environments. Finally, there isn't the established legacy for Be as there is for glass. As such, few optics shops have the tooling and experience needed to successfully polish Be. All of these factors mean that Be is several times more expensive to work with than glass.

[15] Young's modulus is a measure of how much stress (force/area) you can put into something before it yields a given amount. Rubber has a small Young's modulus compared to that of steel.

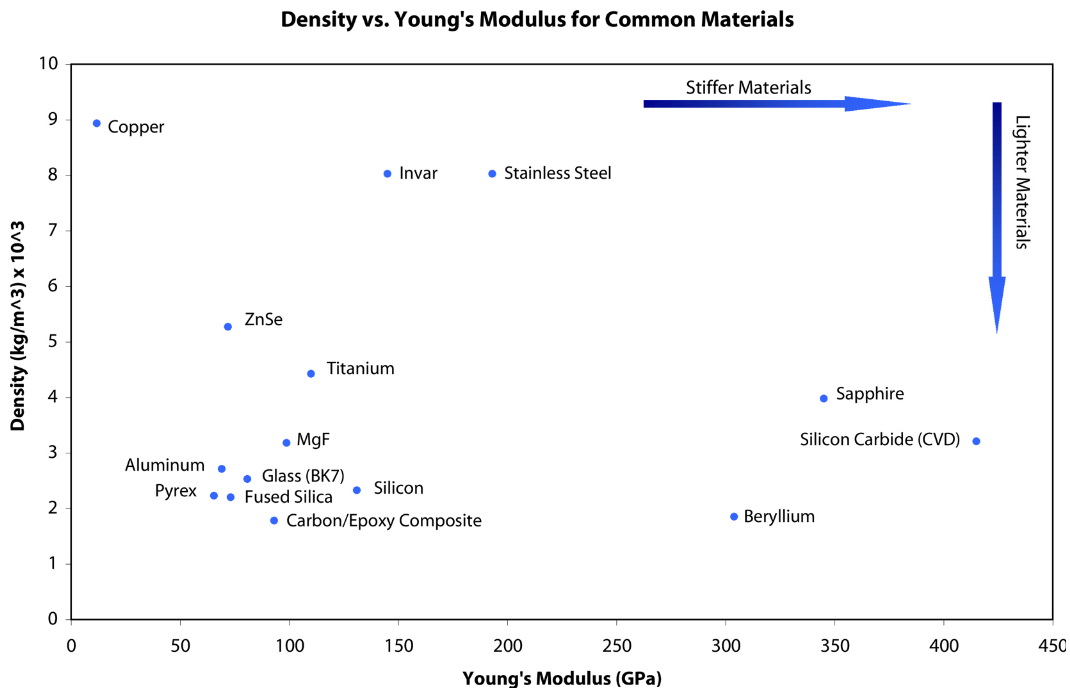

FIGURE 1.10. Density versus Young's modulus for various opto-mechanical materials. Specific stiffness is defined as the mass density divided by Young's modulus. Ideally, space mirrors should be made from materials that are both lightweight (low density) and stiff. Beryllium and silicon carbide both meet these requirements.

The current state of the art in Be mirror demonstrations is Ball Aerospace's Advanced Mirror System Demonstrator (AMSD) [15]. This 1.39 m mirror was successfully completed in the summer of 2003. The total areal density is 15.6 kg/m^2, and this includes substrate, flexures, actuators and reaction structure. The optical figure at ambient temperatures was measured to be 70.0 nm surface rms.

Silicon carbide Silicon carbide (SiC) is another potential mirror substrate, although no parts have been fabricated at any large ($>$ 0.5 meter) scale. SiC is an attractive material because it is inexpensive to produce, and it can be formed into non-conventional shapes rather easily. SiC's biggest advantage is that it has a very high specific stiffness. The material also has a high fracture toughness which makes it an excellent candidate for the telescope structure, as well. There is a big advantage in constructing a telescope's structure and primary mirror out of the same material: the system is athermalized and it will not be affected by temperature change.[16]

SiC presents several challenges, as well. First, the material is very hard, and this makes the polishing effort difficult and time-consuming. SiC also faces challenges becoming accepted into the space mirror community because it lacks the successful legacy of glass or even beryllium. There are currently few funded projects that use a SiC mirror. Finally, because so few mirrors have been created, the long-term stability of these systems is unknown.

1.4.2 The next century

The next century will yield some exciting innovations in the field of space optics. Most important, the limitations in space mirror design will not be due to fabrication limits. Instead, the optical performance will be limited by the inherent properties of the materials used to construct the system. In Chapters 3 and 4, I discuss an approach

[16] If the entire telescope is made out of one material, *everything* will change shape with temperature, and the entire design is just scaled up or down with no degradation in optical performance.

to maximizing the system performance using the least amount of mass. These design strategies will be necessary as the current generation of fabrication techniques mature.

1.5 A quick tour of this dissertation

This work is designed to address the following technical aspects of mirror design and control:

- Chapter 2 is a review of opto-mechanical principles. I don't introduce any novel material in this chapter. Instead, I explain the basics of material properties: stress, strain, Young's modulus, moment of inertia, and the coefficient of thermal expansion. I am including this chapter because all of this information is essential to understanding the material in Chapters 3 and 4.

- Chapter 3 looks at a method for optimizing the design of active mirrors. Ultimately, this chapter answers the following question: "How do I build the best mirror using the least amount of mass?" Currently, mirrors are designed based on the availability and ease of component fabrication. In this chapter, I assume that *anything* is possible, and I derive a set of design conditions assuming that the limiting factors are the inherent mechanical properties of the materials used.

- Chapter 4 looks at the effects of lightweighting the facesheet. By using the structural efficiency as a metric for mirror "goodness", I derive a set of conditions that shows how to get the stiffest substrate for the least amount of mass.

- Chapters 5 and 6 describe the two most recent Arizona MARS mirror demonstrations. Chapter 5 discusses the UA 2 m NMSD mirror. In particular, I discuss the unique challenges associated with measuring a high-authority meter-class active mirror. Chapter 6 discusses the UA ultralightweight 0.5 m mirror. This mirror was built as a technology demonstration for use in geosynchronous orbit, and I discuss the design details that allowed us to meet the areal density specification set forth by the customer.

In addition to covering the aforementioned technical issues, I have incorporated several features into this dissertation which will make it a valuable reference for future researchers:

- I've made an effort to explain the concepts in such detail that a non-specialist can understand what I've done. I assume little prior knowledge about optics or mechanics. This may prove tedious to the experienced optical engineer, but I am confident that it will benefit more often than it frustrates.

- This work should be self-contained. Chapter 2 contains all of the important background information such that outside background reading should not be necessary.

- Most of the concepts that I discuss are drawn from the aerospace industry, which is famous for using a myriad of acronyms. As such, there is a glossary of terms, acronyms, and abbreviations in Appendix A.

- Footnotes are used liberally throughout to explain concepts, add anecdotes, and clarify some words.

- References are denoted by a number within square brackets. [π] References can be found at the end of this book, preceding the Appendix.

- Each chapter includes a summary at the end. In it, I summarize the important conclusions, equations, and lessons learned that were described in the preceding chapter.

- Most important, I have included an index. By using the index, glossary, and the table of contents, the reader should be able to find information very quickly.

1.6 Chapter summary

This chapter was intended to set the context for the remainder of this dissertation. Specifically, I discussed the following important concepts:

- Space telescopes offer several advantages over their ground-based cousins. Most important, they are above the atmosphere: in space there isn't any weather and the imaging system is unaffected by atmospheric turbulence or absorption.

- There are several challenges to building a successful space telescope. First, the launch vehicle limits both the payload mass and volume. The launch process is also rigorous, and the payload must be robust enough to survive the journey into space.

- The University of Arizona MARS (Figure 1.3) design meets the challenges involved for building a lightweight mirror. The reflective surface is a thin glass membrane, and the surface accuracy is maintained by an array of position actuators. The stiffness is maintained via a lightweight support structure.

- The family of MARS mirrors include the original legacy mirrors as well as the current generation of prototypes. The original MARS mirrors were three identical 53 cm prototypes. The contemporary set of mirrors includes the 2 m and 0.5 m prototypes. These mirrors will be discussed in Chapters 5 and 6, respectively.

- I talked about other mirror technologies that are currently under development at other institutions. Several alternative to the MARS design exist, and each of these designs, including the MARS mirrors, have their advantages and disadvantages.

- For ease of use, this work includes chapter summaries, a glossary, and an index, such that the information contained within can be easily located.

Chapter 2
Basic opto-mechanical principles

Chapters 3 and 4 describe the ideal design space for creating lightweight, active mirrors. These chapters will most likely appeal to the optical engineer, but the derivations are based on mechanical principles. As a result, I am including this chapter as a primer to the material discussed in Chapters 3 and 4. In this chapter, I review some basic mechanical principles that I will use in the remaining chapters. Specifically, I will explain mechanical quantities such as Young's modulus, the stress/strain curve, and flexural rigidity. The material in this chapter is *not* novel—I am not reporting any new results—and readers who understand these concepts should skim or skip this chapter. I am including these explanations for two reasons. First, in later chapters, I will occasionally refer to the equations that I discuss in this chapter. Also, this summary will prevent the reader from having to research any outside sources about the mechanical concepts discussed in future chapters.

2.1 Mechanical quantities

2.1.1 Forces & moments

The force is at the heart of all classical mechanical situations. Forces make things happen. A force is classically defined by Newton's second law ($\vec{F} = m\vec{a}$), and it exists whenever a mass m is accelerated by acceleration $\vec{a}$. Force has units of $\mathrm{kg} \cdot \mathrm{m/s^2}$, which is equivalent to a Newton (N).

A moment[1] is a force applied through a distance, and this is illustrated in Figure 2.1. Moments tend to make things rotate. A moment is defined as follows:

[1] Physicists refer to moments as *torques*. It's the same thing.

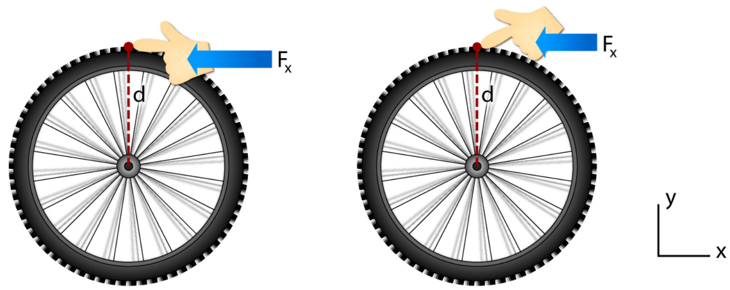

FIGURE 2.1. Moment demonstration. The finger exerts a force at the red dot (at the edge of the tire). Left: the hand exerts a force along a direction perpendicular to the line that contains the tire hub and the red dot, and the wheel starts spinning. Right: The hand exerts a force along a direction other than the perpendicular. Only the x component of F contributes to spinning the wheel.

$$\vec{M} = \vec{F} \times \vec{d}, \tag{2.1}$$

where $\vec{F}$ is a force exerted through distance $\vec{d}$. M is a vector because it represents the cross product of two individual vectors. The units of M are Newton-meters ($\mathrm{N} \cdot \mathrm{m}$). Notice that, because the moment is a cross product, only the component of the force that is perpendicular to the distance vector is used to calculate the moment. This concept is illustrated in Figure 2.1.

2.1.2 Stress, strain, and Young's modulus

When a material is subjected to an external force or moment, it's helpful to have a set of quantities available that describe how the material reacts to those forces. For example, if a steel I-beam is subjected to a moment, it will bend a little bit, Figure 2.2. Stress is what causes the I-beam to bend; strain describes how much it will bend; and Young's modulus is the constant that relates the two.

Stress, usually denoted by a σ, is defined as a force per unit area:

$$\sigma = \frac{F}{A}, \tag{2.2}$$

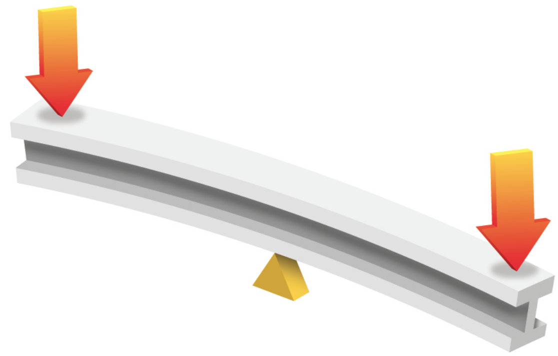

FIGURE 2.2. A bending I-beam. A stress is applied (in the form of a moment) at the ends of the I-beam, and the beam bends a little bit.

and it has units of N/m^2 (Pascals). Note that stress and pressure are the same thing: they both represent a force per area.

Strain, usually denoted by an ϵ, is defined as a change in dimension over the initial dimension due to an external stress σ:

$$\epsilon = \frac{\Delta L}{L}, \tag{2.3}$$

where this is the relationship for a one-dimensional example. Notice that strain is dimensionless. Stress and strain are related: the more stress (force) is applied, the more something will strain, or yield.

Young's modulus is the constant that relates these two quantities:

$$\sigma = E\,\epsilon. \tag{2.4}$$

Because ϵ is a dimensionless quantity, Young's modulus has the same units as stress σ, N/m^2. Equation 2.4 is analogous to Hooke's Law, which relates force F and displacement x for a spring: $F = kx$, where k is usually referred to as the spring constant. In either case, a force is exerted, something reacts (by changing dimension), and a constant relates the two quantities.

Figure 2.3 shows a typical stress-strain curve. There are several features in this graph which help illustrate the relationship between stress, strain and Young's modulus. First, notice that the first portion of the line is linear. In this region of the curve, the material behaves linearly. Linear materials obey the relationship described in Equation 2.4. As such, the slope of the line is Young's modulus. Materials with a larger value of E will change dimension less given the same amount of stress: steeper slopes mean the material is less likely to deflect under stress.[2] Within this linear portion of the curve, the material is subjected to stress, and it will always return to its initial dimensions when the stress is removed.

The curve shown in Figure 2.3 also has a non-linear portion. In this region, the material will *not* snap back to its original dimension when the stress is released. Instead, the material will follow a different path (the dotted line in Figure 2.3), and the material will remain permanently changed. Ultimately, of course, a material will eventually break if subjected to enough stress, and this breaking point is illustrated by the red 'x' in Figure 2.3.

The stress-strain curve shown in Figure 2.3 is typical of metals. For glass, the curve is slightly different: the relationship is linear right up to the breaking point. Also, the location of the breaking point is highly dependent on the glass quality. Glass sheets with no inclusions or microfractures can tolerate large amounts of strain.

2.1.3 Poisson's ratio

Poisson ratio's is best understood by considering a rubber cube, Figure 2.4. If a compressive force is exerted along one axis, the rubber will expand out along another axis. This effect is common in most materials, and it is quantified using Poisson's ratio. Specifically, Poisson's ratio is a measurement of how an object's dimensions change (relative to one another) as a force is exerted. Poisson's ratio ν is defined as

[2] For example, the stress-strain curve for steel will feature a much steeper slope than a similar chart for aluminum.

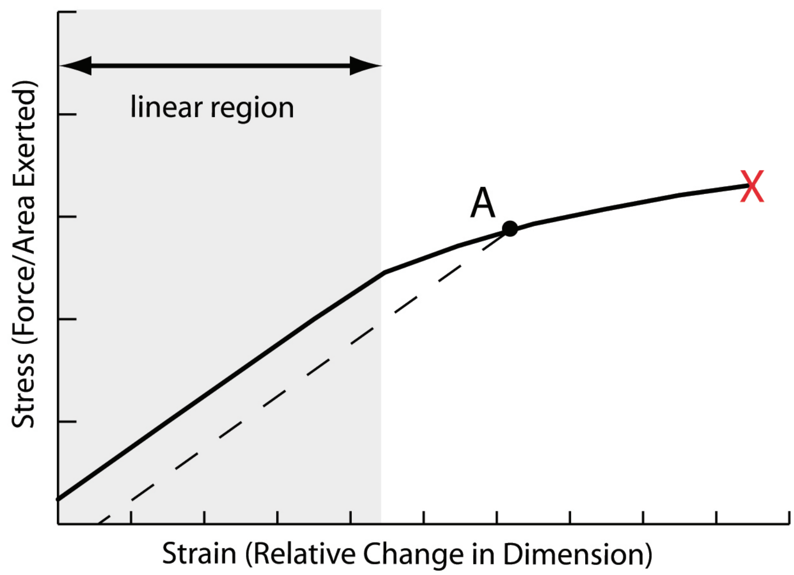

FIGURE 2.3. The stress-strain curve. Stress σ is plotted along the vertical axis, and strain ϵ is plotted along the horizontal axis. The slope of the linear region is Young's modulus E. For most of the curve, the material behaves according to a linear relationship: $\sigma = E\,\epsilon$. If the material is stressed outside of its linear region (to point A, for example), the material will suffer a permanent shape change. For example, if stressed to point A, the material will *not* follow the solid line back to the origin when the stress is released. Instead, it will follow the dotted line, and the dimensional change will be permanent. There is, of course, an amount of stress which will cause the material to break, and this breaking point is noted by the red "X" on the curve. The stress at this point is called the ultimate strength.

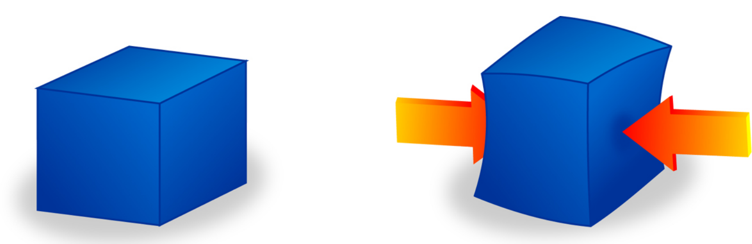

FIGURE 2.4. The Poisson effect. Left: a rubber cube. Right: a rubber cube with a stress applied along one axis. Because of this force the rubber is compressed along one direction, but it expands along another. The Poisson ratio quantifies this effect.

$$\nu = \frac{\text{unit lateral contraction}}{\text{unit axial elongation}}. [24] \tag{2.5}$$

Poisson's ratio is positive for normal materials.[3] Rubber has a relatively large Poisson ratio ($\nu = 0.5$); stainless steel has a smaller value ($\nu = 0.29$).

2.1.4 Flexural rigidity

The flexural rigidity D is the bending analogue of Young's modulus. It tells how much, given a particular moment, something will bend:

$$\frac{1}{r} = \frac{M}{D},$$

where M is the moment exerted on the plate, and r is the resulting radius of curvature of the plate. [25] As D increases, it takes more force (or moment) to bend the piece by an equivalent amount.[4]

The flexural rigidity is a little different than the other quantities previously described because it is heavily dependent on the geometry of the plate or member. For example, I-beams are used because they are almost as stiff as a solid beam, but they can be significantly lighter. Clearly, there is something about the geometry of an I-beam that allows this to be the case. Timoshenko derives an expression for D that holds for thin plates and shells:

$$D = \frac{E}{1 - \nu^2} \frac{I}{B}, \tag{2.6}$$

where E is Young's modulus, ν is Poisson's ratio, B is the width of a cross-sectional element, and I is the moment of inertia[5]. [25]

[3] Lateral contraction usually leads to axial elongation.

[4] In other words, larger values for D mean that the plate or shell is more difficult to bend.

[5] The moment of inertia is discussed in Section 2.3.

2.2 Coefficient of thermal expansion

Most materials change shape when they change temperature, and the coefficient of thermal expansion (CTE) is a way of quantifying this effect. CTE is usually represented by the Greek letter α, and its units are part-per-million/^{o}C. For example, if a 1 meter-long bar has a CTE of 7 ppm/^{o}C and it uniformly changes temperature by +1^{o}C, it will expand in length by 7 millionths of a meter.

This change in length is related to the CTE and temperature by the following relationship:

$$\Delta l = l\,\alpha\,\Delta T, \tag{2.7}$$

where α is the CTE and ΔT is the temperature change.

Finally, it is interesting to note that, by dividing both sides of Equation 2.7 by l, the quantity $(\alpha\,\Delta T)$ is equal to strain:

$$\epsilon = \frac{\Delta l}{l} = \alpha\,\Delta T. \tag{2.8}$$

This relationship is used in Chapter 3.

2.3 The moment of inertia

As a body rotates, two geometrical properties determine how it will behave: the location of the point about which the body rotates, and the distribution of mass about the rotation point. The moment of inertia quantifies both of these parameters.

Figure 2.5 shows a two-dimensional area A. The moment of inertia of A about the respective x or y axis is

$$\begin{aligned} I_x &= \int y^2\,dA \\ I_y &= \int x^2\,dA. \end{aligned}$$

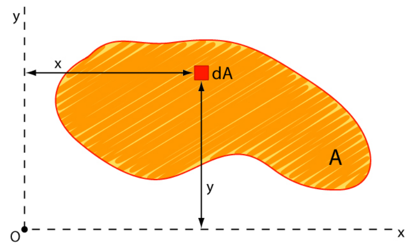

FIGURE 2.5. Calculating the moment of inertia for an area A. The moment of inertia is always calculated with respect to an axis. In this example, the moment is calculated about the x or y axis.

For common geometries, the moment of inertia can be found in a table like the one shown in Figure 2.6. Figure 2.6 reiterates the fact that the moment of inertia is highly dependent on the structural member's geometry. For example, the I for a solid rectangular beam and an I-beam with the same overall dimensions will be very different.

In the context of this work, the moment of inertia is an important component of the flexural rigidity (Equation 2.6), and it's important to understand how it's calculated.

2.3.1 Center of mass

The illustrations that appear in Figure 2.6 show a set of axes through each cross-section. This is because the moment of inertia must be calculated with respect to some point. This point is usually chosen to be the center of mass.

The center of mass is essentially a weighted average, and it is mathematically defined as follows:

$$\vec{r} = \frac{1}{M}\int \vec{r}\,\mathrm{d}m = \frac{\sum_i \vec{r_i}\,m_i}{\sum_i m_i}, \tag{2.9}$$

where $\vec{r_i}$ points to an infinitesimally small unit of mass m_i, and the total mass is $\sum_i m_i = M$. [14] Notice that the center of mass is a vector: it is a particular location

Cross Section	Area	Moment of Inertia
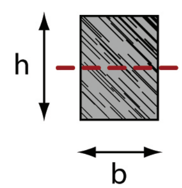	bh	$\frac{bh^3}{12}$
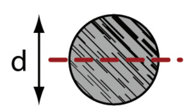	$\frac{\pi d^2}{4}$	$\frac{\pi d^4}{64}$
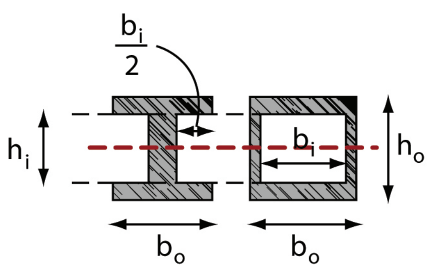	$h_o b_o - h_i b_i$	$\frac{1}{12}(h_o^3 b_o - h_i^3 b_i)$

FIGURE 2.6. Common moments of inertia. Notice that each case has a red axis drawn through it. This is the centroidal axis: it passes through the center of mass, described in Section 2.3.1, and it is the axis about which the moment is calculated. If a different axis is appropriate for a calculation, Equations 2.10 and 2.11 can be used to shift the axis to any arbitrary location.

in space.

2.3.2 Transfer of axes

Sometimes it is necessary to calculate the moment of inertia about a point other than the center of mass. There is a simple method available for transferring from the centroidal axes to an arbitrary set of axes. (The centroidal axes intersect at the center of mass.) The moment of inertia about an arbitrary set of axes x and y is

$$I_x = \overline{I_x} + A\, d_x^2 \tag{2.10}$$

$$I_y = \overline{I_y} + A\, d_y^2, \tag{2.11}$$

where I_x and I_y are the moments of inertia about arbitrary axes x and y; $\overline{I_x}$ and $\overline{I_y}$ are the moments of inertia about the centroidal axes x_{o} and y_{o}; and d_x and d_y are the respective distances between x & x_{o} and y & y_{o}.

2.3.3 Practical example: calculating I for a ruler

As an example, I will calculate the moment of inertia for a ruler. The cross section of a ruler is approximately 1" tall and 0.25" wide. The equation for the moment of inertia for a rectangular cross section can be found in Figure 2.6: it is $b\,h^3/12$. I'll assume that the ruler is mounted in a springboard fashion on the edge of the table such that the increment numbers are touching the table, Figure 2.7. In this case, the moment is

$$I = \frac{1 \cdot 0.25^3}{12} \approx 0.0013 \text{ in}^4.$$

As expected from experience, the ruler will be very flexible if a force is exerted on the free end. However, now consider what happens if the ruler is turned such that its

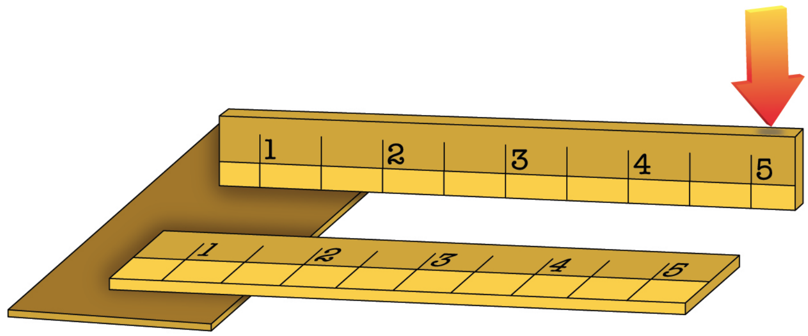

FIGURE 2.7. Rulers and the moment of inertia. The moment of inertia for a rectangular cross section is $\frac{1}{12}bh^3$. When the ruler rests flat on the table (bottom ruler), $b > h$. When the ruler is turned such that its narrow width rests on the table (upper ruler), $h > b$. In fact, the upper ruler has a moment of inertia that is roughly 16 times greater than the lower ruler. This means that it will be 16 times harder to bend when pushing down at the end of the ruler.

short width is touching the table. The geometry has changed, and it's necessary to recalculate the moment of inertia:

$$I = \frac{0.25 \cdot 1^3}{12} \approx 0.021 \text{ in}^4.$$

Notice that this value is roughly sixteen times larger than the previous case! Flexural rigidity is directly related to the moment of inertia (Equation 2.6); as a result, the ruler is *sixteen times* harder to bend. This example emphasizes that stiffness is directly related to the moment of inertia and the beam geometry.

2.4 Chapter summary

In this chapter, I reviewed the following basic mechanical and material properties:

- **Force** A force accelerates a mass. Forces make things move. They have units of Newtons ($\text{kg} \cdot \text{m/s}^2$).
- **Moment** A moment (or torque) is a force applied through a distance. Moments typically make things bend or spin. They have units of $\text{N} \cdot \text{m}$.

- **Stress** A stress is a force per unit area. Stress σ has units of Pascals (N / m^2).
- **Strain** A strain is a reaction to stress: it characterizes how the material changes shape when a force is exerted on it. Strain is dimensionless.
- **Young's modulus** Young's modulus is a constant that relates stress and strain in a linear relationship. It quantifies how easily a material resist yielding to a stress. Young's modulus has the same units as stress: Pascals (N / m^2).
- **Flexural rigidity** The flexural rigidity is the bending analogue of Young's modulus. D has units of N $\cdot$ m.
- **Coefficient of thermal expansion** The coefficient of thermal expansion quantifies the dimensional change that occurs when a material is heated or cooled. It typically has units of parts-per-million per degree Celsius.
- **Moment of inertia** The moment of inertia tells how the mass is distributed across the cross section of a body. The moment of inertia for most common geometries is available in a table like the one shown in Figure 2.6.

Chapter 3

Optimized, active space mirrors

3.1 Building a better active mirror

Today, mirror designs come about due to strange circumstances: funding, schedule, and legacy all play an important role in the final specifications of a mirror. Because of this, mirrors are rarely mass-optimized during the design process. This chapter provides an optimum mirror design that is independent of schedule, cost, and ease of fabrication.[1]

Figure 3.1 is an illustration of the UA MARS mirror design. There are several ways to make this mirror lighter. First, the support structure can always be made lighter by using thinner laminates and/or more aggressive lightweighting. However, the design of the support structure is governed entirely by system dynamics. The resulting structure must satisfy the design requirements for resonant frequency, stiffness and thermal specifications. These are issues best solved by mechanical engineers. As a result, the support structure will not be considered a variable in this analysis.

There are two ways to make the MARS design lighter, and both variables are intertwined with each other. One way to make the mirror lighter is to reduce the thickness of the facesheet.[2] If the thickness is reduced, more actuators are necessary to maintain the same surface quality. The alternative is to make the facesheet thicker (and stiffer). This adds mass, but the mirror will lose some mass because fewer actuators are necessary for maintaining the same surface accuracy.

---

[1] To be fair, the design algorithm isn't going to require the use of 1 nm thick reflective membranes or actuators that weigh half a gram. In Section 3.2.4, I will work an example that shows that the model provides designs that can be fabricated using today's technologies.

[2] The stiffness goes as the cube of the thickness: using a facesheet half as thick results in a reduction in stiffness by a factor of eight!

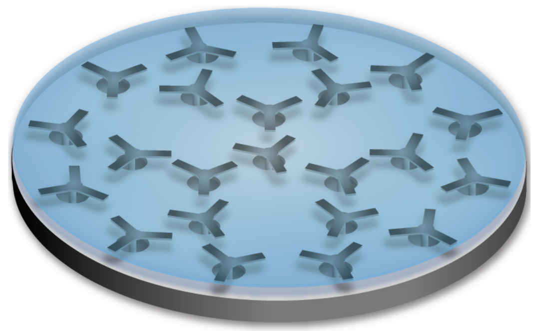

FIGURE 3.1. The University of Arizona lightweight active mirror design. There are two ways to make this mirror lighter. The first way is to reduce the thickness of the glass facesheet. This results in less mass due to the glass, but more actuators are necessary to maintain the same surface accuracy. Alternatively, the glass thickness could be increased, and this would result in the use of fewer actuators because the facesheet would be stiffer. Clearly, there must be a way to distribute the mass between the facesheet and actuators such that performance is optimized while the mass is minimized. This chapter works towards answering that question.

Looking at these concerns raises the obvious question: is there an ideal way to distribute the mass between the actuators and the facesheet? This chapter works through a derivation for finding this solution. I will show that there *is* an ideal solution, provided that a few assumptions are made.

Unlike conventional mirrors that derive their stiffness from their thickness, the surface quality for a thin, active mirror isn't determined by the structural geometry of the substrate.[3] The design uses an array of force or position actuators to correct for any localized figure errors. These figure errors can be from several sources: self-weight deflection (gravity), temperature gradients across the material, or fabrication errors. Whatever the cause, all of these sources cause localized stresses in the membrane.

Throughout this entire chapter, I will assume that all of the practical aspects of the mirror behave the way they were designed. For example, the actuators will move the correct distance when they are instructed to do so, and the glass will be

[3]I define "thin" as having an aspect ratio of over 100. That is, the diameter is at least 100 times larger than the thickness.

polished to the proper specification. I will assume that inherent material properties and environmental effects are to blame for errors in the surface figure.

3.2 Discrete temperature/CTE patches

In this section, I will derive a set of design rules that specify how to distribute the mass between the substrate and the actuators for the best possible performance with the least mass. To do this, however, it's necessary to look at what causes errors in the mirror's surface.

Even if a mirror is fabricated to the specifications provided by the design team, there are still several outside factors which may degrade the optical performance. All science instruments are subject to the effects of their environment, and space mirrors are no exception. An extreme example of this is that orbiting satellites risk being destroyed by space debris. Temperature is a more subtle effect. If different parts of the mirror have different temperatures, the optical performance will be affected.

The inherent material properties also affect the optical performance. For example, most materials expand when heated and contract when cooled. The coefficient of thermal expansion (CTE) is a physical value that quantifies this effect.[4] For most situations, engineers assume that the CTE of all bulk materials (i.e.: a rod of steel or a sheet of glass) is homogenous throughout the material. However, when dealing with optical tolerances, it's important to realize that the CTE is *not* constant throughout the material.

For this derivation, I will assume that surface errors in the membrane are caused either by discrete temperature differences (patches of hot and cold spots on the membrane), regions with different coefficients of thermal expansion combined with a global temperature change, or both. However, while I do assume that these patches exist, I also assume that each patch is homogeneous, Figure 3.2. Combined, these two

[4] CTE is discussed in Section 2.2.

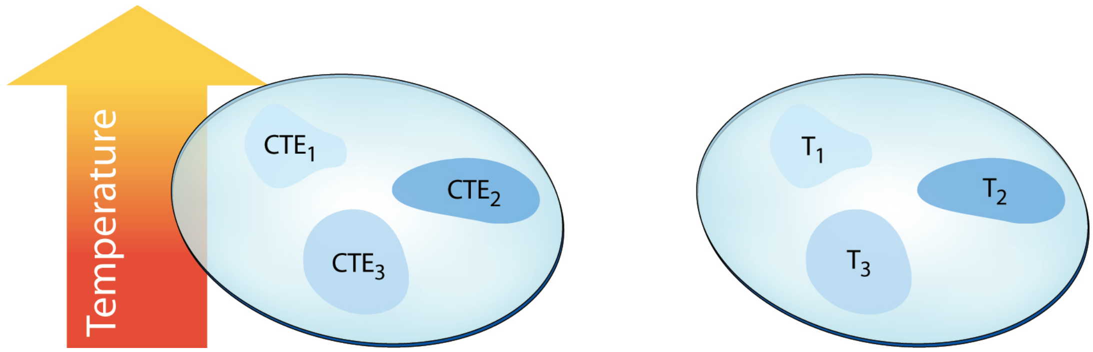

Figure 3.2. The two effects that can affect the shape of the mirror's surface. Left: patches of different CTEs combined with a global temperature change result in regions of the mirror that expand and contract at different rates with a change in temperature. Right: patches of the mirror at different temperatures result in non-uniform expansion/contraction of the mirror's surface. Both of these effects distort the substrate. Notice that, within each patch, I will assume that the CTE or temperature is constant.

effects can cause errors in the mirror surface at various spatial frequencies, and the errors that are larger in scale than the actuator spacing can be fixed by moving the actuators.[5]

The following derivation assumes that errors in the mirror result from the two effects described above. Given a target mass budget for the entire mirror, I will derive the optimum fabrication parameters (membrane thickness, membrane mass, and number of actuators) that produce the lightest, most accurate mirror. In an effort to concentrate on the big picture, the mathematics are only briefly described during the derivation. The full derivation is included in Sections 3.2.6 and 3.2.7.

3.2.1 Supporting a membrane with a discrete number of points

Both of the effects illustrated in Figure 3.2 will cause a disturbance in the membrane. If this occurs, a region on the membrane will expand or contract, pushing or pulling against the area around it, and a "blister" will form. Of course, if this occurs over

[5]This concept is illustrated in Figure 1.4

several actuator lengths, the actuators can be used to remove this error from the surface figure.

In order to fix the blisters, the actuators must exert a force on the membrane. Because the membrane is supported by a discrete number of points, the surface will consist of local bumps over every actuator.[6] Obviously, these bumps will affect the surface quality of the membrane, and this effect is quantified by using a relationship that Nelson developed [20] that describes the rms surface error of a plate that is supported by N points:

$$\delta_{\mathrm{rms}} = 0.0012\,\frac{P}{D}\left(\frac{A}{N}\right)^{2}. \tag{3.1}$$

The rms surface error δ_{rms} is a function of the force per unit area P applied by N actuators, and it is the starting point for the derviation. A is the total plate area, and N is the number of support points. D is the flexural rigidity, and it depends strongly on the geometry of the membrane.[7] Equation 3.1 has two key assumptions associated with it:

- The substrate is a thin shell.
- The actuators are arranged in a triangular, periodic pattern. A triangular geometry is more effective at correcting the surface error[8] than a hexagonal, circular, or rectangular geometry. [20]

Equation 3.1 is difficult to apply directly to the UA active mirrors because we usually don't know how much pressure each actuator must exert to fix a blister.[9]

[6] If the actuators have the ability to pull downward, there might be little dimples, as well.

[7] The flexural rigidity is discussed in Section 2.1.4.

[8] Nelson provides a thorough analysis of this in his paper. [20] In it, he shows that a triangular configuration results in a surface rms error that is 10% less than a square geometry and nearly 50% less than a hexagonal geometry. He assumes that the plates are semi-infinite with a large number of support points. By doing this, edge effects can be neglected. In his derivation, all of the support points (for all three geometries) support an equal area.

[9] Instead, the person adjusting the mirror just applies enough force until the surface is fixed.

To that end, it would be useful to derive an expression for P that depends on more tangible variables. Because I want to focus on the practical conclusions to be drawn from this relationship, I will only show the results here. A detailed derivation is included in Section 3.2.6. The new expression for P is as follows:

$$P = \frac{2t\,[CE\Delta(\alpha\,T)]}{R},$$

and this can be substituted into Equation 3.1 to get a new expression for $\delta_{\rm rms}$:

$$\delta_{\rm rms} = \frac{0.03\,C(1-\nu^2)\,\Delta(\alpha\,T)}{R\,t^2}\left(\frac{A}{N}\right)^2. \tag{3.2}$$

Here is a description of the variables in Equation 3.2:

$\boldsymbol{\nu}$	Poisson's ratio (See Section 2.1.3.)
$\boldsymbol{\Delta(\alpha\,\mathrm{T})}$	Sources of stress (Figure 3.2): $\Delta(\alpha T) = (\alpha\Delta T + T\Delta\alpha)$
$\boldsymbol{C}$	Shell constant (See Section 3.2.6. C doesn't affect the solution.)
$\boldsymbol{R}$	Shell radius of curvature
$\boldsymbol{t}$	Shell thickness
$\boldsymbol{A}$	Shell area
$\boldsymbol{N}$	Number of actuators

Equation 3.2 represents an important conclusion. This equation is an expression for RMS surface error that depends on the two material properties responsible for causing the error: temperature (T) and CTE (α) differences. Also note that, unlike Equation 3.1, Equation 3.2 is now in terms of three fabrication parameters: t, A, and N, the thickness, shell area, and number of actuators, respectively. These are all parameters that affect the system mass.

A fundamental relationship for thin mirrors is contained within Equation 3.2. The variables for shell thickness and the number of actuators are both in the demonimina-tor: more actuators or a thicker shell result in a smaller residual error. Also, there is a direct tradeoff between shell thickness and the number of actuators. For example, if the shell thickness t decreases by half, then the number of actuators N must double to maintain the same surface quality $\delta_{\rm rms}$. In fact, this is the mathematical expression of the assertion that I made in Section 3.1: it shows the interconnectedness of the number of actuators and the thickness of the substrate.

Finally, it's worth noting that Equation 3.2 does not contain Young's modulus, E.[10] This implies that the designer does not gain anything by choosing a stiffer material: in theory, rubber is just as acceptable as glass or metal, given the initial assumptions. Choosing a stiffer material will require more force from the actuators to remove the blisters, yet the force that is applied through the actuators will cause a surface error that is described by Nelson's equation (Equation 3.1). These two effects cancel each other out, and E is not a factor in the design algorithm.[11]

3.2.2 Optimizing the system for the smallest rms surface error δ_{rms}

Equation 3.2 yields some insightful information, but it doesn't provide a solution for building a mass-optimized mirror. Practically speaking, the system mass is an important factor in designing space mirrors. All three of the fabrication parameters (t, A, and N) affect the mass, so Equation 3.2 can be optimized to find the ideal fabrication parameters for the smallest value of δ_{rms}.

If I express t and N in terms of mass, I can take the derivative—with respect to the substrate mass, of Equation 3.2—set it equal to zero, and find the mass condition that minimizes δ_{rms}. The mathematics are described in Section 3.2.7. When t and N are expressed in terms of mass, Equation 3.2 can be written as follows:

$$\delta_{\mathrm{rms}} = \frac{0.03\, C(1-\nu^2)\Delta(\alpha\, T)\, \rho^2 A^2}{R\left(\frac{m_{sub}}{A}\right)^2 \left(\frac{m-m_{sub}}{m_{act}}\right)^2}, \tag{3.3}$$

were m_{sub} is the mass of the substrate, m_{act} is the mass of each actuator, and m is the total mass (such that $m = m_{sub} + Nm_{act}$). To optimize Equation 3.3, I'll take

[10] It falls out of the derivation. See Section 3.2.6.

[11] It's not a factor, with one caveat: this assumes that the mirror will be used in a zero-gravity environment. Here on Earth, presumably where the mirror will be fabricated and tested, there's an additional force: gravity. 'E now comes into play again, as a glass membrane will be easier to test than a rubber membrane.

the derivative with respect to m and set it equal to zero. The following relationship results:

$$\begin{aligned}(4m_{sub} - 2m)(m_{sub} - m) &= 0 \\ m_{sub} &= \frac{m}{2}.\end{aligned}$$

The answer is stunningly simple! This relationship states that the minimum surface error will occur when the shell mass, m_{sub}, makes up one half of the mass budget.[12] In other words, the optimum correction occurs when

$$\text{substrate mass} = \text{actuator mass}.$$

This relationship occurs because t^2 and N^2 are both in the denominator in Equation 3.2. Neither term can get too small or δ_{rms} will rapidly increase. The ideal solution occurs when the mass is balanced equally among the substrate and actuators. Here are the basic relationships:

$$\begin{aligned} t &= \frac{m_{sub}}{A\rho} = \frac{N m_{act}}{A\rho} \\ m_{sub} &= N m_{act} = \frac{m}{2}. \end{aligned} \tag{3.4}$$

With these relationships in place, I can outline a procedure for designing the optimum a mirror:

1. Determine the mass budget and substrate diameter. This sets the values for the total mass, m, and the area of the substrate, A.

2. Calculate the mass budget for the substrate:

$$m_{sub} = \frac{m}{2}.$$

[12] The solution where $m_{sub} = m$ is trivial.

3. Calculate the substrate thickness:

$$t = \frac{m_{sub}}{A\rho}.$$

4. Use the thickness t to determine the total number of actuators from the mass of each actuator. (I assume that the actuator mass is a predetermined constant.)

$$Nm_{act} = tA\,\rho$$

Notice that this approach assumes a fixed actuator mass. Mirror designers usually have a working actuator design in mind when they design an active mirror, and they can use this value to calculate the required number of support points. As the actuator mass decreases, more actuators can be included in the design.

Finally, it's important to notice that this design scheme does not include the mass of the support structure. The support structure's design depends on the system dynamics so I did not consider it in this analysis. When I discuss the "mass budget", I refer only to the elements that maintain the reflective surface: the thin membrane and the actuators.

3.2.3 Why does it work?

The design algorithm that falls out of the equations is elegantly simple; however, the equations don't provide much insight on why the solution makes physical sense. Figure 3.3 shows an example plot of residual surface error (Equation 3.3) as a function of fractional substrate mass.[13] The plot shows that the minimum amount of surface error occurs when the facesheet uses 50% of the mass budget. This makes physical sense because of what happens at either extreme. For example, the left side of the

[13] I had to make some decisions about the material properties and mirror geomery in order to create this plot. For example, I assumed that the facesheet had the following physical properties: Pyrex glass ($\rho = 2.23$ g/cm^3, $\nu = 0.2$), 200 cm radius of curvature, 50 cm diameter, $C = 0.36$ (see Section 3.2.6), and $\Delta(\alpha T) = 10^{-4}$.

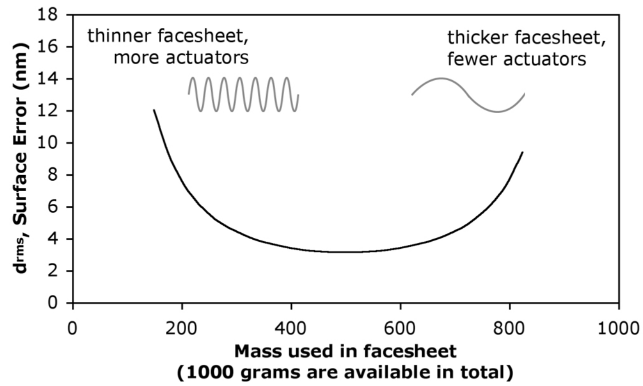

FIGURE 3.3. δ_{rms} as a function of facesheet mass. The minimum surface error occurs when half the mass budget is used for the facesheet. Lighter (thinner) facesheets are subject to high frequency error because more actuators will exist. Heavier (thicker) facesheets are subject to low frequency bending errors. The optimum solution occurs in the middle where neither low nor high frequency errors will dominate.

plot represents using the majority of the mass for the actuators. When this occurs, the facesheet will be very thin, and high frequency errors will dominate because the facesheet will slump about the support points. By contrast, if the majority of mass is used for the facesheet, there will be very few actuators and low-order bending will contribute most of the surface errors. The best solution occurs right in the middle where neither high or low spatial frequency errors will dominate the surface figure.

3.2.4 Practical example: 2 m mirror for use in geosynchronous orbit

As a practical example, let's put the four step procedure to work by calculating the parameters for a hypothetical two meter mirror for use at geosynchronous orbit. Geosync orbit is useful for Earth-imaging situations because the satellite remains fixed over the same position as the Earth rotates.[14] For this exercise, assume that an areal density of 5 $\frac{\text{kg}}{\text{m}^2}$ is the nominal areal density required for this application. [2] Applying the areal density over a two meter mirror, the mass budget for the glass

[14]The basics of geosynchronous orbit are discussed in Section 6.1.

and the actuators is as follows:

$$\begin{aligned}
\text{total mass} &= \text{areal density} \times \text{aperture area} \\
m &= 5\frac{\text{kg}}{\text{m}^2} \times (1\text{m})^2\pi \\
&= 5\pi \text{ kg} \\
m &\sim 16 \text{ kg.}
\end{aligned}$$

After calculating the target mass and mirror diameter, the mass budget for the substrate is as follows:

$$\begin{aligned}
m_{sub} &= \frac{m}{2} \\
&= \frac{16 \text{ kg}}{2} = 8 \text{ kg.}
\end{aligned}$$

Before continuing, it is necessary to choose a substrate material. Corning's ULE[15] is an appropriate choice. ULE has a density *rho* of 2210 $\frac{\text{kg}}{\text{m}^3}$. Using step three, the substrate thickness is calculated using Equation 3.4:

$$\begin{aligned}
t &= \frac{m_{sub}}{A\rho} \\
&= \frac{8 \text{ kg}}{(\pi \text{ m}^2)(2210\frac{\text{kg}}{\text{m}^3})} \\
t &= 1.2 \text{ mm.}
\end{aligned}$$

Finally, I can use step four to calculate the required number of actuators. If I know *a priori* that the actuator fabrication house can build 50 gram actuators ($m_{act} = 50$ g), then I can calculate how many support points I will need:

[15]This glass has a very low coefficient of thermal expansion; standard-grade ULE has a CTE of 15 $\frac{\text{ppb}}{^\circ\text{C}}$. By comparison, BK-7 has a CTE of 7000 $\frac{\text{ppb}}{^\circ\text{C}}$. This glass is usually a good choice for space applications.

$$
\begin{aligned}
t &= \frac{N m_{act}}{A\rho} \\
N &= \frac{tA\rho}{m_{act}} \\
&= \frac{(.0012\ \mathrm{m})(\pi\ \mathrm{m}^2)(2210\ \frac{\mathrm{kg}}{\mathrm{m}^3})}{0.050\ \mathrm{kg}} \\
N &= 167\ \text{actuators.}
\end{aligned}
$$

It's important to note that all of the values obtained via this procedure are reasonable and capable of being fabricated! The University of Arizona has created 50 cm Zerodur substrates less than 1 mm thick. [5] Steward Observatory has designed and built actuators that are less than 40 grams. [7] The numbers generated in this example are certainly possible using existing fabrication methods.

Finally, it's interesting to note that the University of Arizona 2 m mirror, discussed in Chapter 5, roughly meets this specification. The areal density of the 2 m is 13 kg/m^2, which is twice the value used in this example. However, the facesheet is 2 mm thick, and the mirror uses 166 actuators that have a mass of 40 grams each. Again, the 2 m stands as another example that this model produces physical parameters that are both reasonable and easy to build.

3.2.5 Using loadspreaders

Loadspreaders are often used in lightweight, active mirrors, Figure 3.4. Incorporating a loadspreader into the mirror design offers several benefits. First, the loadspreader increases the area of an actuator's influence function. For example, a loadspreader with a three inch footprint will result in a smoother Gaussian influence than an actuator in direct contact with the substrate. Also, using loadspreaders result in a safer mirror design. They allow each actuator to influence a larger portion of the substrate, and this results in less stress/area in the mirror's surface. In addition to

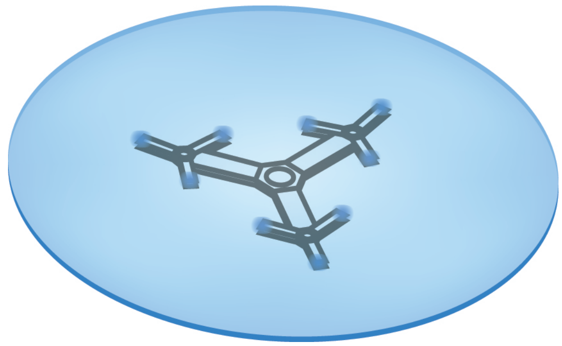

FIGURE 3.4. A nine-point loadspreader. Loadspreaders (or whiffle trees) are used to spread an actuator's influence out over a larger area. For example, this particular loadspreader contacts the actuator on its underside (in the middle of the spreader), and it spreads the force imparted by the actuator to nine contact points on the mirror. Section 3.2.5 describes how to interpret the design rules such that loadspreaders can be included in the mirror design.

this, complex loadspreaders can be designed to disengage when they are subjected to too much, or too little, force.[16]

Loadspeaders are easy to include in the design scheme laid out in this chapter. First, it's necessary to differentiate between the number of actuators, N_{act}, and the total number of contact points, N_{pts}:

$$N_{\text{pts}} = N_{\text{act}} \times N_{\text{pts/act}},$$

where N_{pts} is the total number of support points on the substrate, N_{act} is the total number of actuators, and $N_{\text{pts/act}}$ is the number of support points controlled by each actuator. (For example, here are the values for a mirror with four actuators, where each actuator has a nine point loadspreader: $N_{\text{pts}} = 36$, $N_{\text{act}} = 4$, and $N_{\text{pts/act}} = 9$.)

Finally, Equation 3.4 can be written to include the loadspreader mass:

[16]The UA 2 m NMSD mirror uses a complex loadspreader. See Section 5.1.3.

$$\begin{aligned}
t &= \frac{N_{act} m_a}{A\,\rho} = \frac{m_{sub}}{A\,\rho} = \frac{m_{support}}{A\,\rho} \\
N_{pts} &= \frac{tA\,\rho}{m_{support}} \\
N_{pts} &= \frac{tA\,\rho}{(m_a + m_{ls})},
\end{aligned} \tag{3.5}$$

where $m_{sub} = m_{support}$ is the key design rule (i.e.: the mass of the substrate must equal the total actuator/support mass), m_a is the mass of an individual actuator, m_{ls} is the mass of an individual loadspreader, t is the substrate thickness, A is the surface area of the substrate, and ρ is the mass density of the substrate.

The loadspreaders are part of the support structure, so it is appropriate to include their mass in Equation 3.5. Note that this expression works in the absence of loadspreaders, too: in that case, $m_{ls} = 0$ and $N_{pts} = N_a$.

In Section 3.2.4, I calculated the number of actuators required for a 2 m meter in geosynchronous orbit. The results show that 167 fifty gram actuators minimize the rms surface error while utilizing the least mass. Now, let's suppose that each actuator is 40 grams, and a 10 gram three-point loadspreader will be used. Equation 3.5 is used to calculate the ideal design parameters:

$$\begin{aligned}
N_{pts} &= \frac{tA\,\rho}{(m_a + m_{ls})} \\
N_a \times N_{pts/act} &= \frac{tA\,\rho}{(m_a + m_{ls})} \\
3N_a &= \frac{(.0012\ \mathrm{m})(\pi\ \mathrm{m}^2)(2210\ \frac{\mathrm{kg}}{\mathrm{m}^3})}{(0.040\ \mathrm{kg} + 0.010\ \mathrm{kg})} \\
N_a &= 56\ \text{actuators.}
\end{aligned}$$

Thus, 56 actuators can be used to maintain the same number of contact points (167).[17] The rms surface error is still held to a minimum, yet fewer actuators are necessary.

[17] This solution assumes an infinite actuator pattern. In reality, the actuator density must be increased near the edge to handle the edge effects.

3.2.6 Derivation details: pressure expression for δ_{RMS}

In an ideal situation, once the actuator has been activated, it should be able to remove all of the surface error caused by the strain. In reality, however, a small error remains. In 1982, Nelson presented a relationship that describes the rms surface error of a plate supported by N support points:

$$\delta_{\text{rms}} = 0.0012\,\frac{P}{D}\left(\frac{A}{N}\right)^2. \tag{3.6}$$

The rms surface error δ_{rms} is a function of the force per unit area P applied by the actuators. A is the total plate area, and N is the number of support points. D is the flexural rigidity, which is given by this relationship:

$$D = \frac{Et^3}{12(1-\nu^2)}, \tag{3.7}$$

where t is the shell thickness, ν is Poisson's ratio ($\frac{\epsilon_{\text{trans}}}{\epsilon_{\text{long}}}$), and E is Young's modulus.

The expression for δ_{rms} will be more helpful if P is expressed in terms of something more tangible than the pressure applied by the actuators. The following derivation for P generates an expression that depends on the shell thickness, blister size, and the stress.

Before I derive the expression for pressure P, it is helpful to look at a similar situation: a balloon, illustrated in Figure 3.5. When the balloon is inflated, there are two opposing forces at work. As the balloon is inflated, the rubber stretches out. This causes an internal *membrane stress* that is tangent to the balloon's surface. Once the balloon has some air in it, it is in static equilibrium: it does not change its size. As such, there must be a reaction force to counteract the membrane stress. The reaction force comes from the air pressure inside the balloon.

Like the balloon, a glass shell is subject to similar forces. When either of the temperature/CTE effects described in Figure 3.2 are present, a blister will form. Figure 3.6 shows a shell with radius of curvature R that contains a blister that is

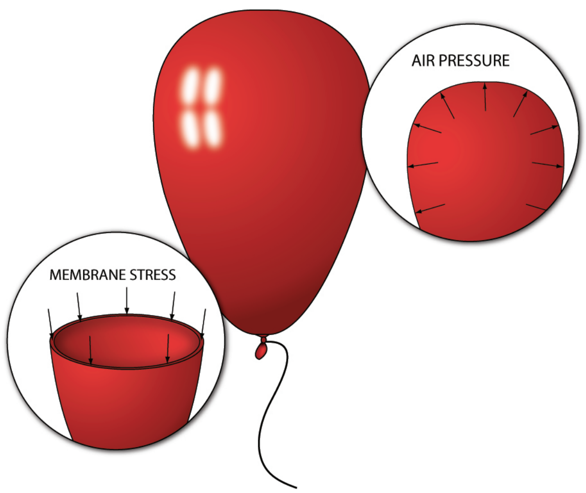

FIGURE 3.5. The science of balloon inflation. After the balloon has some air in it, two opposing forces are at work. The stretched-out rubber has a membrane stress; this is tangent to the balloon's surface. This pressure wants to make the balloon smaller. Opposing this, there is a reaction pressure in the form of air pressure that pushes outward, normal to the balloon's surface. This pressure wants to make the balloon larger. The balloon is in static equilibrium (once inflated, it does not change size) so the two forces must be equal.

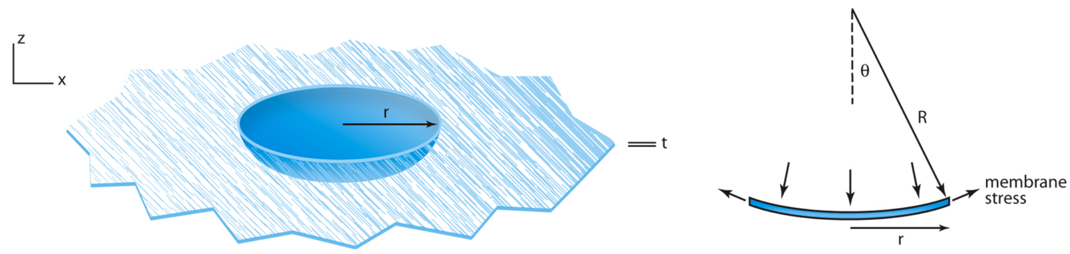

FIGURE 3.6. A stress causes a blister to appear on a glass shell. Right: the geometry of the blister of radius r.

r units wide. The local blister is subject to two forces: a membrane stress σ and a counteracting reactive force P.[18] The membrane stress is, like the balloon example, tangent to the shell. Because the system is in static equilibrium, the z components of the two forces are equal across the blister.

The force due to the membrane stress is expressed as follows:

$$\begin{aligned} F_z &= A_{\text{annulus}} (\sigma \sin\theta) \\ &= 2\pi r t \left(\sigma \frac{r}{R}\right), \end{aligned}$$

where $(\sigma \sin\theta)$ is the z component of the membrane stress and A_{annulus} is the area over which that stress acts. The blister size is assumed to be small compared to the shell's radius of curvature, so I can substitute (r/R) for $\sin\theta$.

The reaction force P opposes the membrane stress. It acts on the projected area of the blister:

$$\begin{aligned} F_z &= P A_{\text{blister\_proj}} \\ &= P\pi r^2. \end{aligned}$$

[18]This derivation assumes that the reactive force P and the blister's curvature are constant.

Because the system is in static equilibrium, the two forces are equal:

$$\begin{aligned} 2\pi r t\left(\sigma\frac{r}{R}\right) &= P\pi r^2 \\ P &= \frac{2\sigma t}{R}. \end{aligned} \tag{3.8}$$

The expression for P in Equation 3.8 contains the membrane stress, σ. Stress is defined in Equation 2.4 as the product of Young's modulus and the strain: $\sigma = E\epsilon$. In Equation 2.8, I noted that strain is equal to $(\alpha\,\Delta T)$. Physically, this represents the scenario shown on the left side of Figure 3.2. Similarly, the quantity $(T\,\Delta\alpha)$ is also a strain. (This represents the scenario shown on the right side of Figure 3.2.)

Thus, for a flat, solid plate, the stress is given by this relationship:

$$\sigma = E\,\Delta(\alpha T). \tag{3.9}$$

where $\Delta(\alpha T)$ denotes the possibility of either strain occurring: $\Delta(\alpha T) = \alpha\,\Delta T + T\,\Delta\alpha$.

Equation 3.9 is for a flat plate, but the stress for a curved shell will be smaller. To determine the correct relationship for a shell, Brian Cuerden developed a finite element model for this situation, and he determined that the following relationship holds true for a thin[19], curved shell:

$$\sigma = 0.36E\,\Delta(\alpha T).$$

For the general case, I will replace Brian's empirical coefficient with a shell constant C such that $\sigma = C\,E\,\Delta(\alpha T)$. I will carry this constant C through the remainder of the derivation, but it will never affect the ultimate solution.

I will substitute this equation for σ into Equation 3.8 to get a new expression for P:

[19] A thin shell has an aspect ratio of at least 100.

$$\begin{aligned} P &= \frac{2\sigma t}{R} \\ &= \frac{2t(CE\Delta(\alpha T))}{R}. \end{aligned} \tag{3.10}$$

Notice that Equation 3.10 now expresses pressure P as a function of the two possible sources of surface error shown in Figure 3.2.

Finally, I will solve Equation 3.7 for Young's modulus E, and I will substitute this into Equation 3.10:

$$\begin{aligned} P &= \frac{2t(CE\Delta(\alpha T))}{R} \\ &= \frac{2t\left[C(\frac{12}{t^3}D(1-\nu^2))\right]\Delta(\alpha T)}{R}. \end{aligned}$$

Now that I have a new expression for P, I will substitute this into Equation 3.6, the starting point in this derivation:

$$\begin{aligned} \delta_{\rm rms} &= 0.0012\,\frac{P}{D}\left(\frac{A}{N}\right)^2 \\ &= 0.0012\,\frac{\left(\frac{2t(C(\frac{12}{t^3}D(1-\nu^2)))\Delta(\alpha T)}{R}\right)}{D}\left(\frac{A}{N}\right)^2 \\ \delta_{\rm rms} &= \frac{0.03\,C(1-\nu^2)\,\Delta(\alpha T)}{R\,t^2}\left(\frac{A}{N}\right)^2. \end{aligned} \tag{3.11}$$

Equation 3.11 now contains a tangible fabrication parameter that depends on mass: the substrate thickness t.

3.2.7 Derivation details: finding the minimum of $\delta_{\rm RMS}$ by taking a derivative

The system mass is an important design factor for lightweight mirrors. All three of the fabrication parameters (t, A, and N) depend on mass, so I can optimize Equation 3.2

to find the optimum fabrication parameters for the smallest mass. To do this, I first need to express t and N in terms of mass.

First I'll express the shell thickness, t in terms of m_{sub}, the mass of the shell. This can be done by starting with two well-known relationships:

$$\begin{aligned} V &= A\,t \\ \rho &= \frac{m_{sub}}{V}, \end{aligned}$$

where V is the volume of the shell and ρ is the density. If I combine these two relationships, I get an expression for the thickness in terms of the mass of the shell:

$$t^2 = \left(\frac{m_{sub}}{A}\right)^2 \frac{1}{\rho^2}. \tag{3.12}$$

This result is squared because the thickness term in Equation 3.2 is squared.

Now, I'll express the number of actuators in terms of the shell mass. The total mass is equal to the following expression:

$$\begin{aligned} \text{total mass} &= \#\text{ actuators (mass at each support point)} + \text{substrate mass} \\ m &= N m_{act} + m_{sub}, \end{aligned}$$

where m_{act} is the actuator mass. Solving this equation for N yields

$$N = \frac{m - m_{sub}}{m_{act}}. \tag{3.13}$$

Finally, I will substitute Equations 3.12 and 3.13 into Equation 3.11:

$$\delta_{\text{rms}} = \frac{0.03\,C(1-\nu^2)\Delta(\alpha\,T)\rho^2 A^2}{R\left(\frac{m_{sub}}{A}\right)^2\left(\frac{m-m_{sub}}{m_{act}}\right)^2}. \tag{3.14}$$

Now that I have the residual surface rms expression in terms of mass, I will take a derivative with respect to m_{sub}, set it equal to zero, and find the condition that minimizes the rms surface error $\delta_{\rm rms}$.

The dependent variable in Equation 3.14 is m_{sub}. It will be easier to take the derivative if we just concentrate on the parts that include m_{sub}. With this in mind, let's rewrite Equation 3.14 without all of the constants and then take the derivative and set it equal to zero:

$$\begin{aligned}
\delta_{\rm rms} &\propto \frac{1}{m_{sub}^2(m-m_{sub})^2} \\
&\propto \frac{1}{m_{sub}^2(m^2-2m\,m_{sub}+m_{sub}^2)} \\
&\propto \frac{1}{m_{sub}^2\,m^2-2m\,m_{sub}^3+m_{sub}^4} \\
\frac{d\delta_{\rm rms}}{dm_{sub}} &\propto \frac{0-(2m_{sub}\,m^2-6m\,m_{sub}^2+4m_{sub}^3)}{\left(m_{sub}^2\,m^2-2m\,m_{sub}^3+m_{sub}^4\right)^2}=0 \\
4m_{sub}^3-6m\,m_{sub}^2-2m^2\,m_{sub} &= 0 \\
m_{sub}\,(4m_{sub}-2m)(m_{sub}-m) &= 0 \\
m_{sub} &= \frac{m}{2}.
\end{aligned}$$

3.3 Gradient temperature/CTE patches

In Section 3.2, I assumed that the errors in the substrate were caused by the inherent material properties (CTE variations) as well as environmental considerations (changes in temperature). In doing this, I also assumed that the patches on the substrate were homogeneous throughout.

In this section, I will assume that the patches are *not* homogeneous. Most important, I allow the patches to contain temperature or CTE gradients in a direction that is normal to the substrate, Figure 3.7.

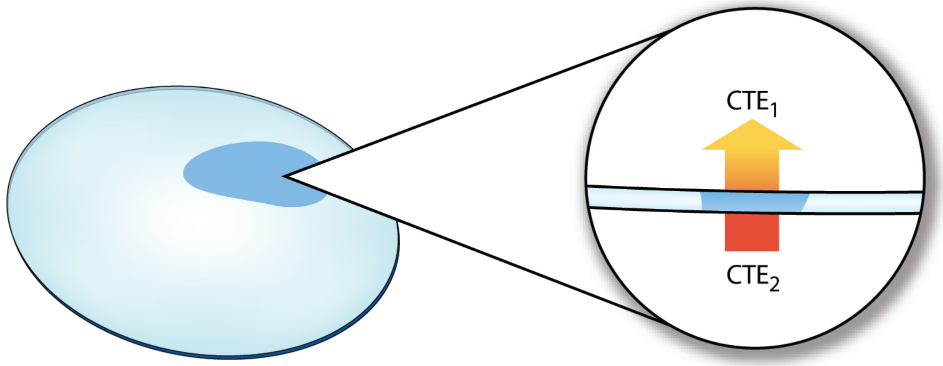

FIGURE 3.7. Gradient patch effects. In Section 3.2, I derived a set of optimum design conditions assuming that the limiting errors are caused by discrete temperature/CTE patches across the substrate. A more realistic consideration is that the patches will really be gradients of temperature or CTE, as seen above. In this section, I re-derive the design conditions assuming there is a temperature/CTE gradient normal to the substrate.

Unlike the derivation shown in Section 3.2, I will include the full derivation here, without the use of appendices. The procedure will remain the same as the previous chapter: I will identify the sources of errors in the substrate, and then I will use these to derive a set of optimum design rules. As before, Nelson's equation (Equation 3.1) will be the starting point for this derivation. Recall that Equation 3.1 contains the pressure/area, P, exerted by each support point. This quantity is rather nebulous, so the purpose of this derivation will be to replace P with a more tangible expression. To do this, I will use the following procedure:

1. First, I will generate a function that describes the surface error due to a temperature gradient.

2. Next, I will describe a transfer function that relates surface error to the required actuator pressure needed to fix that surface error.

3. I will multiply the two functions from steps 1 and 2 to find the pressure function, P.

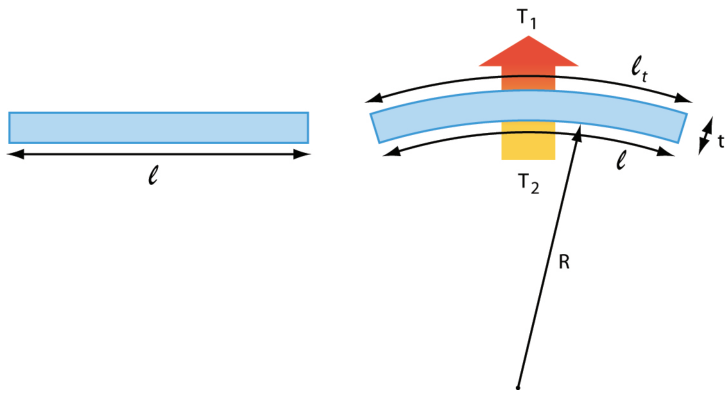

FIGURE 3.8. Thermal bending for a homogeneous plate. When a linear thermal gradient is applied through a bar of material, it bends. The amount that it bends is proportional to the size of the temperature gradient. In Section 3.3.1, I derive an expression that relates the amount of bending (quantified by the radius of curvature, R) to the temperature gradient, ΔT.

4. Finally, I will substitute this new equation for P into Nelson's equation.

3.3.1 Generating a function that relates surface error to temperature gradients

Figure 3.8 illustrates what happens to a homogeneous plate when a linear temperature gradient is applied in a direction normal to the plate: it bends.[20] This bending can be qualified by specifying the radius of curvature, R, of the bent plate. For a homogeneous shell with a normal, linear temperature gradient through the material, the curvature R changes as a function of temperature gradient, $\Delta T = |T_1 - T_2|$.

To begin, note that the curved surfaces in Figure 3.8 are not the same length. The bottom surface of the shell has length l, and the top surface has length $l + \Delta l$. This change in length is due to the thermal expansion effect, expressed as

$$\Delta l = l \, \alpha \, \Delta T,$$

[20] This is not a crazy idea. In fact, most home thermostats uses this phenomenon as the technique for measuring temperature change.

where α is the coefficient of thermal expansion of the material. The length of the top surface can now be rewritten as follows:

$$\begin{aligned} l_t &= l + l\alpha\,\Delta t \\ l_t &= l(1 + \alpha\,\Delta t). \end{aligned}$$

The radii of curvature (ROC) of the two surfaces are proportional to their arc lengths[21]:

$$\begin{aligned} \frac{ROC_{\text{top}}}{ROC_{\text{bottom}}} &= \frac{R+t}{R} \\ \frac{l(1+\alpha\,\Delta T)}{l} &= \frac{R+t}{R} \\ 1+\alpha\Delta T &= 1+\frac{t}{R} \\ R &= \frac{t}{\alpha\,\Delta T} = \frac{1}{\alpha\frac{\mathrm{d}T}{\mathrm{d}z}}, \end{aligned} \tag{3.15}$$

where t is the shell thickness, α is the CTE of the shell, and ΔT is the temperature difference through the plate.

For the case of space mirrors, the substrate is usually a shell: it already has some initial curvature to it. Thus, it is more instructive to describe the shape in terms of curvature instead of radius. Recall that curvature is defined as $\frac{1}{R}$. Doing this means that Equation 3.15 can be rewritten as a differential equation:

$$\frac{\mathrm{d}^2 z}{\mathrm{d}x^2} = \alpha\frac{\mathrm{d}T}{\mathrm{d}z}. \tag{3.16}$$

Equation 3.16 is a differential equation that I will solve by assuming a form for $\frac{\mathrm{d}T}{\mathrm{d}z}$. If $\frac{\mathrm{d}T}{\mathrm{d}z} = K(\xi)\cos(2\pi\xi x)$, this can be substituted into Equation 3.16, and I can solve for $z(x)$ by integrating twice:

[21] For a circle of radius r, the arc length contained by an angle ψ is $r|\psi|$. [12] Arc length is linearly proportional to the radius of curvature.

$$\begin{aligned}\frac{\mathrm{d}^2 z}{\mathrm{d}x^2} &= \alpha\, K(\xi)\cos(2\pi\xi x)\\ z(x) &= -\frac{\alpha}{(2\pi\xi)^2}K(\xi)\cos(2\pi\xi x)\\ z(x) &= -\frac{\alpha}{(2\pi\xi)^2}\frac{\mathrm{d}T}{\mathrm{d}z},\end{aligned}\tag{3.17}$$

where $K(\xi)$ is the amplitude of the cosine function. Equation 3.17 describes the surface error due to a temperature gradient through the shell as a function of spatial frequency ξ.

3.3.2 Defining a transfer function

In the previous section, I derived an expression for surface error as a function of temperature gradient through the shell. This surface error can be corrected by the actuators because they exert a pressure on the shell. The amount of pressure required to do this is proportional to the surface error, and I just need to find the scaling factor between them. The scaling factor Γ is a transfer function that scales the surface error $s(x)$ to the pressure required to fix it $p(x)$:

$$p(x) = s(x)\cdot\Gamma,\tag{3.18}$$

where Γ is the transfer function that relates the two.[22] Equation 3.18 is analogous to Hooke's Law ($F = kx$), which relates a force to a product of linear distance and stiffness. Thus, the transfer function that I seek is a stiffness (a spring constant) that relates pressure to surface error.

The transfer function that I will use was developed by Mehta [18] and further explained by Michael Tuell in his master's thesis [26].[23] Mehta looked at correcting

[22] Γ also depends on the spatial frequency of the surface error $s(x)$.

[23] Mehta is responsible for developing the theory, but Tuell's derivation is more accessible.

high spatial frequency errors in aspheric optics. He developed expressions for the polishing tool stress when it contacts an aspheric optical surface. I will summarize Mehta's derivation in the following paragraphs, and the complete details are available in either work by Mehta or Tuell.

Mehta starts with two simultaneous partial differential equations that describe the tool deflection w as a function of the flexural bending and transverse shear stiffnessnes:

$$\nabla^4 w = \frac{q}{D} - \frac{\nabla^2 q}{D_s} \tag{3.19}$$

$$\nabla^2 \left(\frac{\partial^2 w}{\partial x^2} - \frac{\partial^2 w}{\partial y^2} \right) - \frac{2D_s}{D(1-\nu)} \left(\frac{\partial^2 w}{\partial x^2} - \frac{\partial^2 w}{\partial y^2} \right) = 0. \tag{3.20}$$

Equation 3.20 is a form of the Helmholtz equation, and it represents the deflection due to torsion.

Equation 3.19 characterizes the deflection due to bending and transverse shear; it describes the relationship between tool deflection w, pressure distribution acting on the tool q, flexural rigidity D, and shear stiffness D_s. The flexural rigidity (discussed in Section 2.1.4) characterizes the bending stiffness. The shear stiffness D_s is

$$D_s = G\,t = \frac{E\,t}{2(1+\nu)}, \tag{3.21}$$

where E is Young's modulus, t is the shell thickness, and ν is Poisson's ratio. Physically speaking, the shear stiffness is a measure of resistance to shearing when a transverse shear force is exerted upon a material.

When Equations 3.19 and 3.20 are solved for the pressure q, the following solution results:

$$q = K_c \left(1 - \frac{\beta_1}{\beta_2} \right) s(x), \tag{3.22}$$

where K_c is the pitch stiffness.[24] The variables β_1 and β_2 equal the following:

[24]Equation 3.22 assumes the problem is one-dimensional. That is, Mehta only considers surface

$$\beta_1 = K_c\left[1+\frac{D}{D_s}\left(\frac{\pi^2}{a^2}\right)\right]$$
$$\beta_2 = \beta_1 + D\left(\frac{\pi^2}{a^2}\right)^2,$$

where a is the half period of a spectral feature of the surface error.

In Equation 3.22, the quantity $\left[K_c\left(1-\frac{\beta_1}{\beta_2}\right)\right]$ is just a scaling factor which relates the optical surface error $s(x)$ to the pressure distribution q across the tool, which is the same relationship that I show in Equation 3.18. Tuell rewrites the quantity $\left[K_c\left(1-\frac{\beta_1}{\beta_2}\right)\right]$ in a more intuitive form:

$$\Gamma = K_c\left(1-\frac{\beta_1}{\beta_2}\right) = \frac{1}{\frac{1}{16\pi^4 D\xi^4}+\frac{1}{4\pi^2 D_s\xi^2}+\frac{1}{K_c}}, \tag{3.23}$$

where he substitutes ξ for $\frac{1}{2a}$ such that his expression is in terms of spatial frequency ξ.

Equation 3.23 describes the stiffness of the polishing tool—or any thin plate—considering the effects of bending ($\frac{1}{16\pi^4 D\xi^4}$), transverse shear ($\frac{1}{4\pi^2 D_s\xi^2}$), and pitch compliance ($\frac{1}{K_c}$). Note that the bending and stiffness terms depend on the spatial frequency of the error. For large spatial frequencies (short spatial periods), the shear term dominates. By contrast, bending dominates for small spatial frequencies (long spatial periods). This makes physical sense: long beams (small ξ) will deflect due mostly to bending.[25]

For this analysis, I will make two assumptions before proceeding. First, the $\frac{1}{K_c}$ term (the pitch compliance) is inappropriate in this situation, so I will always assume that $\frac{1}{K_c}=0$. Also, I will assume that the strain caused by the temperature/CTE effects results in bending deflection only. Mathematically, this means that I will assume that the $\left(\frac{1}{4\pi^2 D_s\xi^2}\right)$ shear term is equal to zero. This approximation is appropriate

---

errors in one direction. (The error in the other direction is assumed to have an infinite spatial period.)

[25]This concept is also discussed in Figure 4.16.

because I am assuming that the surface errors occur across several actuators where bending will be the dominant deflection.[26]

The surface error $z(x)$ and the transfer function Γ can now be multiplied together (as in Equation 3.18) to get an expression for pressure:

$$\begin{aligned} p(x) &= z(x) \cdot \Gamma \\ &= \frac{-\alpha\left(\frac{\mathrm{d}T}{\mathrm{d}z}\right)}{\frac{(2\pi\xi)^2}{16\pi^4 D\xi^4}} \\ p(x) &= \frac{-\alpha\left(\frac{\mathrm{d}T}{\mathrm{d}z}\right)}{\frac{1}{4\pi^2 D\xi^2}} \end{aligned} \tag{3.24}$$

D, the flexural rigidity, is discussed in Section 2.1.4.

3.3.3 A revised expression for Nelson's equation

Equation 3.24 now represents a more tangible expression for pressure, and it can be substituted into Nelson's equation as follows:

$$\begin{aligned} \delta_{\mathrm{rms}} &= 0.0012\frac{P}{D}\left(\frac{A}{N}\right)^2 \\ &= \frac{-0.0012\,\alpha\left(\frac{\mathrm{d}T}{\mathrm{d}z}\right)}{\frac{1}{4\pi\xi^2}}\left(\frac{A}{N}\right)^2 \end{aligned} \tag{3.25}$$

3.3.4 Optimizing the system for the smallest mass

Equation 3.25 describes the rms surface error in the mirror substrate due to gradient temperature/CTE patches. This relationship says that using more actuators per unit area will result in a smaller rms surface error. Unlike the scenario described in Section 3.2, there is *not* an ideal solution for this situation.

[26]Shear is most likely to dominate over shorter distances.

Equation 3.25 suggests that the surface error is independent of thickness, and this may seem counter-intuitive. For example, a half meter, 5 mm thick, 25 actuator mirror will have the same surface error as a half meter, 10 mm thick, 25 actuator mirror. The thicker mirror will require a pressure that is proportional to the bending stiffness D (Equation 3.24) to fix the surface error, but the surface error (via Nelson) is inversely proportional to D. In the end, the thickness (buried within D) falls out of the relationship.

Note that these results are derived assuming a *flat plate*. (The solution from Section 3.2 inherently assumes that the shell is curved.) For a thin shell, the additional stiffness obtained by using a curved structure will change these results.

3.4 Which model is the best?

The two models used in this chapter start with different assumptions. Therefore, they are appropriate in different situations. The solution for discrete temperature/CTE patches that resulted in an optimum solution ($m_{actuators} = m_{substate}$) should be used when the dominant cause of surface errors is temperature changes across the mirror. This model also assumed that the substrate was a thin shell.

The solution for gradient temperature/CTE patches is only valid for flat plates. It is most applicable when small surface errors exist due to figure errors or temperature/CTE gradients.

3.5 Chapter summary

In this chapter, I derived a set of design rules for creating the best possible surface figure with the least amount of mass. Along the way, I made a few assumptions about the geometry and fabrication parameters:

- All of the components (glass, actuators, support structure, etc) must be properly fabricated to the designer's specifications. In other words, actuators actuate properly, and the glass is polished correctly.

- The actuators are arranged in a triangular geometry. (Edge effects were ignored.)

- Surface errors in the substrate are due to temperature changes and CTE variations within the material.

- The mass of an individual actuator is known *a priori*.

I analyzed two different situations, and the overall results from either case were exactly the same:

- First, I looked at the case where homogeneous patches of hot/cold spots or different CTEs exist within the substrate. (This concept is illustrated in Figure 3.2.)

- I also looked at the case where the temperature/CTE patches are *not* homogeneous. (This concept is illustrated in Figure 3.7.)

For homogeneous temperature/CTE patches, the minimum surface error occurs when the mass of the substrate equal to the mass of the support system (actuators + loadspreaders, if any).

In addition to this, the following relationships fall out of the derivation and prove helpful in determining substrate thickness and the number of total actuators required:

$$
\begin{aligned}
t &= \frac{m_{sub}}{A\rho} = \frac{Nm_{act}}{A\rho} \\
m_{sub} &= Nm_{act} = \frac{m}{2}.
\end{aligned}
$$

When using loadspreaders with this model, it is *not* necessary to re-derive anything. Instead, I simply changed the notation such that it was more robust:

$$
\begin{aligned}
N_{pts} &= \frac{tA\,\rho}{(m_a + m_{ls})} \\
N_a \times N_{pts/act} &= \frac{tA\,\rho}{(m_a + m_{ls})}.
\end{aligned}
$$

Note that these relationships reduce to the ones shown previously when no load-spreader is present.

For gradient temperature/CTE patches, there is no optimum solution. As more actuators are used per unit area, the rms surface error decreases.

Chapter 4
Optimized, structured substrates

In the previous chapter, I discussed how the mass should be distributed between the glass and the support system in order to achieve the minimum surface error. Throughout that derivation, I assumed that the membrane was a solid, thin shell. In this chapter, I will explore the possibilities of using a *structured* membrane to maximize the effectiveness of the mass allotted for the membrane.

A structured membrane is a thin shell or plate that is not completely solid. For example, throughout this chapter, I will assume that there are two possible ways of making a shell lighter, and these two schemes are both illustrated in Figure 4.1. The left side of Figure 4.1 shows a sandwich-type design. This scheme consists of a cellular core that is flanked by a face and backsheet. The right side of Figure 4.1 shows a openback geometry.[1] The openback scheme also has a cellular core, but it only has a facesheet.

In this chapter, I will discuss the merits of the two geometries shown in Fig-

[1]This is also referred to as an "egg carton" design.

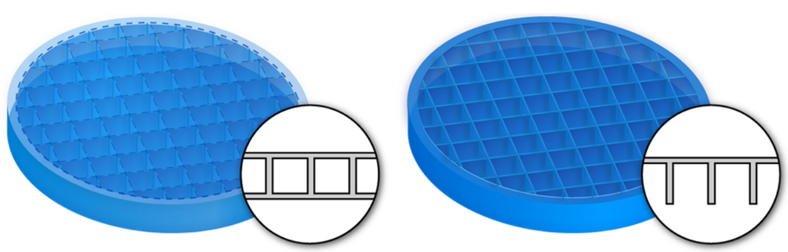

Figure 4.1. Two schemes for lightweighing thin shells. Left: A sandwich scheme uses a facesheet and a backsheet that surround an inner rib structure. Right: The openback scheme uses only a facesheet, and the inner ribbing is exposed from the back.

ure 4.1. I will also show how the structural properties of each geometry change as more material is removed.

4.1 Lightweighting mirrors: a lesson in bending and shear

Before I discuss the individual lightweighting strategies, it's important to understand what happens to a thin plate as material is removed from it. For the purposes of this analysis, the effects on bending and shear are most important.

4.1.1 Bending deflection

Bending is the result of a moment, as discussed in Section 2.1.1. The I-beam in Figure 4.2 bends because gravity causes it to bend under its own weight. Ignoring the effects of shear, the amount of deflection depends on the following equation:

$$\frac{\mathrm{d}^2 z}{\mathrm{d}x^2} = \frac{M}{E\,I},$$

where M is the moment that's causing the bending, E is Young's modulus[2] and I is the moment of inertia[3]. [14] This relationship is important because it shows that the deflection, described as a curvature ($\frac{\mathrm{d}^2 z}{\mathrm{d}x^2}$), depends on the moment of inertia, which depends on the structure's geometry. In order words, the bending properties of an I-beam are very different from those of a solid beam.

This equation can be rewritten to describe the curvature that results from a force $q(x)$ applied along the beam:

[2]Young's modulus is discussed in Section 2.1.2.
[3]The moment of inertia is reviewed in Section 2.3.

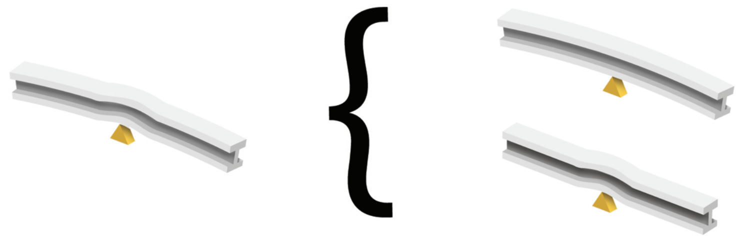

FIGURE 4.2. An I-beam supported at one point. It bends due to its own weight (top right), but it also shears near the support point (bottom right). These two effects combine to create the (exaggerated) shape shown on the left.

$$\begin{aligned} \frac{\mathrm{d}^2 z}{\mathrm{d}x^2} &= \frac{M}{E\,I} \\ \frac{\mathrm{d}^2}{\mathrm{d}x^2}\left(EI\frac{\mathrm{d}^2 z}{\mathrm{d}x^2}\right) &= \frac{\mathrm{d}^2}{\mathrm{d}x^2}M \\ EI\,\frac{\mathrm{d}^4 z}{\mathrm{d}x^4} &= -q(x), \end{aligned}$$

where $-q(x)$ is a force per unit length and is equal to $\frac{\mathrm{d}^2 M}{\mathrm{d}x^2}$. [14]

For the case of thin mirror substrates, it's more appropriate to look at how a *plate* bends. The deflection for a thin, flat, transversely-loaded plate is given by the following relationship:

$$\nabla^4 w = \frac{q}{D}, \tag{4.1}$$

where w is the transverse deflection of the plate, q is the transverse load per unit area, and D is the modulus of flexural rigidity. [3] The most important component of Equation 4.1 is the modulus of flexural rigidity, which was discussed in Section 2.1.4. D is defined by the following relationship:

$$D = \left(\frac{E}{1-\nu^2}\right)\left(\frac{I}{b_o}\right), \tag{4.2}$$

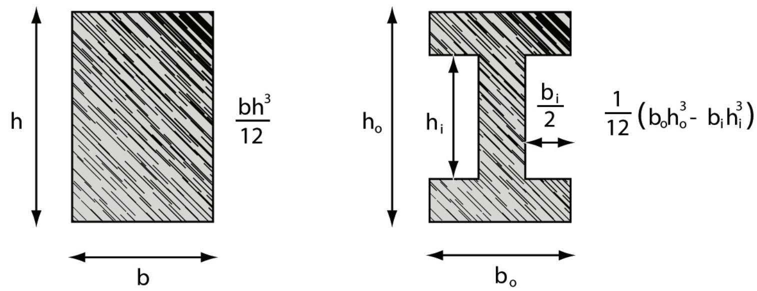

FIGURE 4.3. The moments of inertia for a solid beam and an I-beam. Note that the moment is smaller for the I-beam.

where E is Young's modulus, ν is Poisson's ratio[4], b_o is the width of a cross-sectional unit cell, and I is the moment of inertia. [25]

Again, it's essential to notice that the bending (flexural rigidity D) depends on the moment of inertia I, and I depends strongly on the geometry of the object. For example, the moments of inertia for a solid, rectangular beam and an I-beam are shown in Figure 4.3. Notice that the I-beam has a smaller moment of inertia.

Equation 4.2 implies that there is a way to distribute the mass such that the resulting structure is stiffer than a solid plate of equivalent mass. This is a powerful tool for improving mirror designs, and it will be discussed in Section 4.2.

In conclusion, the following statements about bending deflections are true:

- Bending is caused by a moment.
- The degree to which a structure is likely to bend is closely tied to the moment of inertia (geometry) of the structure. In other words, an I-beam will behave differently than a solid plate.
- Increasing the moment of inertia (I) or the flexural rigidity (D) will result in a stiffer beam or plate.

[4]Poisson's ratio is discussed in Section 2.1.3.

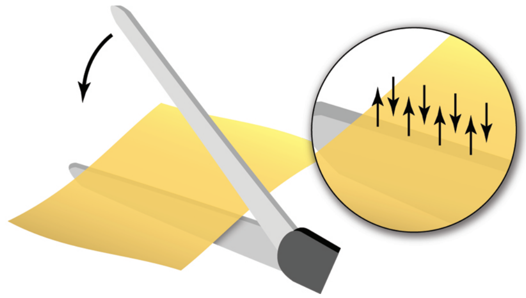

FIGURE 4.4. Scissors use a shearing effect to cut paper. The bottom blade exerts an upward force while the top blade exerts a downward force. This shearing force along a straight line tears the paper into separate pieces.

4.1.2 Shear deflection

Shearing results when molecules slip along a plane that is parallel to the applied force. For example, scissors (or "shears") work by shearing the paper along a line, Figure 4.4. As the top blade of the scissors approaches the cutting point, it exerts a downward force on the paper. Meanwhile, the paper also rests against the bottom blade which provides an upward force. The shear force is so great along the line of contact that the paper tears into separate pieces.

Plates and shells are often subjected to localized shear forces, and it's important to consider what occurs when this happens.[5] Consider a layer of pizza dough, Figure 4.5.[6] If a force is exerted at a discrete point on the dough, the surface figure will change. Why does it assume this particular shape? It does this because the pizza molecules shift past each other along the direction of the force. As a result, a local bump occurs.

The shear modulus, G, is the factor that quantifies this effect.[7] It relates the applied force to the shear deflection:

[5] For example, the Arizona MARS mirrors are subjected to local shear forces from the actuators.

[6] Pizza dough is a better example than glass or metal because it's easier to imagine the effects of shearing.

[7] G is the shear equivalent of Young's modulus for bending deflections. Like Young's modulus, its value is material-dependent, and it is obtained by looking it up in a materials reference book.

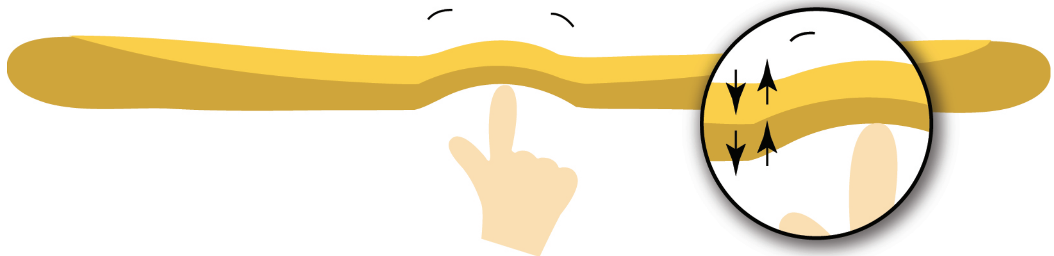

Figure 4.5. This pizza dough is subjected to a localized force (a finger), and it deforms mostly due to shear effects.

$$\begin{aligned} \tau &= G\,\gamma \\ \frac{F}{A} &= G\,\frac{\Delta l}{l}, \end{aligned}$$

where τ is the applied force per unit area, and γ is the strain that results from the force. [14] Materials with a large shear modulus will not experience much shear deflection when a force is exerted upon them.

The shear stiffness, D_s, is analogous to the flexural rigidity for bending: it quantifies how much a particular geometry will deform due to shear forces. The shear stiffness is

$$D_s = G\,h = \frac{E}{2(1+\nu)}h,$$

where E is Young's modulus, G is the shear modulus, ν is Poisson's ratio, and h is the height of the unit cell. [14] The unit cell is chosen such that, when reproduced periodically, the plate's structure is recreated. (The unit cell is discussed in more detail in Section 4.2.) Note that the shear stiffness D_s depends on the plate thickness: thin plates shear more than thick plates.

Thus, the following statements about shear deflection are true:

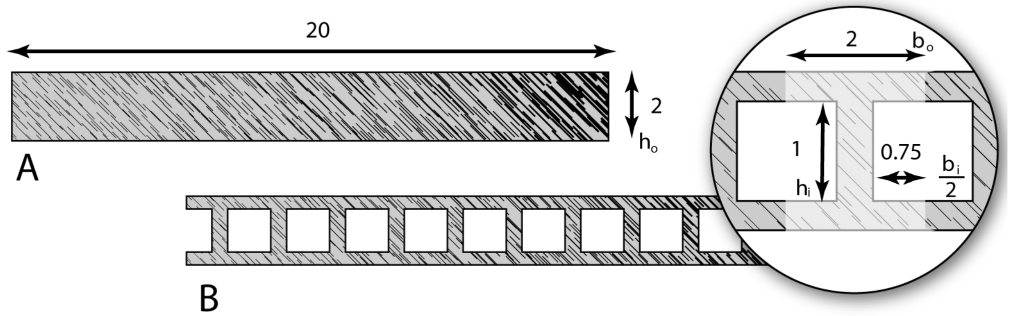

FIGURE 4.6. A comparison between a solid and a lightweighted plate. The callout bubble shows the dimensions of the lightweighted unit cell: $h_o = 2$, $b_o = 2$, $h_i = 1$, and $b_i/2 = 0.75$. The dimensions for the solid unit cell are $h_o = 2$ and $b_o = 2$. (h_i and b_i are equal to zero since the cell isn't structured.)

- The shear stiffness D_s scales linearly with the unit cell height. A thinner plate always has a greater susceptibility to shear.
- Like bending deflection, the amount of shear deflection depends on the structure's geometry.

4.1.3 Practical example: bending for a lightweighted plate

Figure 4.6 shows two plates, each with a different geometry. Plate A is solid and Plate B is lightweighted such that square pockets have been milled out in a periodic fashion. Both plates have the same overall length and width. For the purpose of this example, I will assume that both plates extend out of the page, and the bending occurs in a plane perpendicular to the page.

The results of this comparison are shown in Table 4.1. The moment of inertia was calculated using the equations shown in Figure 4.3. Using the moment of inertia, I was able to calculate the flexural rigidity D using Equation 4.2. Table 4.1 shows that the lightweighted plate has a flexural rigidity that is 9% less than the solid plate. However, note that the areal density for the lightweighted structure is about

Quantity	Solid Plate	Lightweighted Plate	Comments
I (m^4)	$\frac{1}{12}(2 \cdot 2^3)$	$\frac{1}{12}(2 \cdot 2^3 - 1.5 \cdot 1^3)$	LW'd is 9.3% less
D (N·m)	$\frac{E}{B(1-\nu^2)}$ (1.33)	$\frac{E}{B(1-\nu^2)}$ (1.21)	LW'd D is 9.3% less
ϱ ($\frac{\text{kg}}{\text{m}^2}$)	(4) ρ	(2.5) ρ	LW'd areal density is 37.5% less

TABLE 4.1. This table shows the relative values for the following quantities: moment of inertia I, flexural rigidity D, and areal density ϱ. The two structures being compared are the ones shown in Figure 4.6.

62.5% that of the solid plate. This is an important conclusion: it shows that the lightweighted structure is 37.5% lighter yet only 9% more compliant in bending.

4.2 Optimizing the design based on efficient mass distribution

In the previous section, I suggested that a structured mirror could improve the facesheet's stiffness, given a particular mass budget. In this section, I will quantify this effect by performing a detailed analysis that investigates the most efficient way to distribute mass about the plate.

As discussed in the previous section, lightweighted mirror structures can consist of one or two design geometries: sandwich geometries use a cellular core with a face and backsheet, while openback geometries use a cellular core with only a facesheet. These two geometries are illustrated in Figure 4.1.

These geometries have a legacy in several ground-based telescopes. The 200" Palomar mirror, for example, was considered an engineering marvel when it was cast in 1934. Its sheer size was due in part to using a lightweighted, openback Pyrex mirror blank. [9] The blank was cast by using a mold to create the openback geometry. Today, the Steward Mirror Lab casts 8.4 m monolithic mirrors that use a sandwich geometry with a honeycomb structured core. [17]

Both of these lightweighting schemes would lend themselves well to thin mirror substrates. [27, 21] The openback design has already been studied [28, 4, 22, 23] and used in several space mirror prototypes. [8] Openback facesheets are already being used because the technology needed to produce these geometries is already in place. Waterjet-cutting is an established process that uses a high pressure jet of water with a fine particulate to make precise pocket cuts in materials such as glass. On the other hand, it is currently not possible to create high quality, thin substrates with the sandwich design.

To date, no one has studied these geometries in an effort to provide some general scaling laws for their use. For example, for the openback geometry, is there a particular ratio of rib to facesheet thickness that maximizes the structural efficiency? Are there combinations of rib and facesheet thicknesses where lightweighting has little (or no) effect on the structure's stiffness?

To answer these questions, I will examine the structural efficiency of the two geometries shown in Figure 4.1. I will analyze the openback and sandwich geometries to see how the structural efficiency changes as the facesheet, backsheet, and web thicknesses are varied.

4.2.1 Defining the structural efficiency ratio

In order to compare different lightweighting geometries, I will define a metric of quality called the structural efficiency ratio. The structural efficiency will quantify the stiffness for a particular geometry mass. I will begin by using the stiffness expression developed by Mehta and Tuell and discussed in detail in Section 3.3.2:

$$\Gamma = \frac{1}{\frac{1}{16\pi^4 D\xi^4} + \frac{1}{4\pi^2 D_s\xi^2}}, \tag{4.3}$$

were D is the flexural rigidity, D_s is the shear stiffness, and ξ is the spatial frequency (1/in) of the surface errors. [26] Recall that this expression is the stiffness for a thin plate that considers the effects of both bending ($\frac{1}{16\pi^4 D\xi^4}$) and transverse shear ($\frac{1}{4\pi^2 D_s\xi^2}$).

For this analysis, it will be most helpful to compare a particular lightweighted geometry with a solid plate of *equal mass*. This way, I will be able to determine which design uses the mass in the most structurally-efficient manner. To do this, I will define the structural efficiency ratio (sE) as follows:

$$sE = \frac{\Gamma_{LW}}{\Gamma_{solid}}, \tag{4.4}$$

where Γ_{LW} is Equation 4.3 for a lightweighted plate and Γ_{solid} is Equation 4.3 for a solid plate of equivalent mass.

4.2.2 Optimized design: sandwich geometry

Now that the concept of structural efficiency has some mathematics attached to it, Equation 4.4 can be used to analyze a particular situation. In this section, I will discuss the performance of the sandwich geometry, shown in Figure 4.1. First, though, a unit cell must be defined that can be periodically replicated to represent the entire surface.[8] For a sandwich geometry, the unit cell looks like a cross with a face and backsheet, Figure 4.7. The cross section looks just like an I-beam, and this makes it easy to calculate the moment of inertia for this cell:

$$I = \frac{1}{12}(b_o h_o^3 - b_i h_i^3),$$

[8]The use of unit cells to describe the overall structure is supported by two different researchers. Barnes used this approach in his analysis of triangular, hexagonal, and square sandwich structures. [3] For a square sandwich structure, he uses the moment of inertia of a two-dimensional I-beam. His resulting expression for the flexural rigidity D is equivalent to mine, except that his notation is different. Throughout his analysis, he assumes that the unit cell is small in comparison to the overall mirror width. In addition to this, Ralph M. Richard performed two finite element analyses on structured mirrors. The first one used constant-stress, linear-edge displacement membrane triangles. These are elements that were not allowed to bend, but they were allowed to move in piston with respect to one another. The other model used rectangular elements, where each element *was* allowed to bend. The resulting overall mirror stiffnesses were within 2% of each another. [22] Richard's results show that the unit cells do not have to bend in order to model the system correctly. (This assumes, of course, that the unit cells are small in comparison to the overall mirror diameter.)

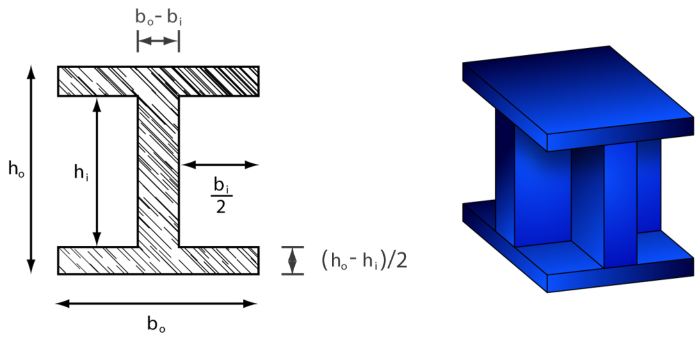

FIGURE 4.7. 2D and 3D unit cells for the sandwich scheme.

where the variables are shown in Figure 4.7.

I can substitute the expression for the moment of inertia into Equation 4.4 such that it represents the specifics of the sandwich geometry:

$$
\begin{aligned}
sE &= \frac{\Gamma_{LW}}{\Gamma_{solid}} \\
&= \frac{\frac{1}{\frac{1}{16\pi^4 D\xi^4}+\frac{1}{4\pi^2 D_s \xi^2}}}{\Gamma_{solid}} \\
&= \frac{\frac{1}{\frac{1}{16\pi^4\left(\frac{E}{1-\nu^2}\frac{I}{b_o}\right)\xi^4}+\frac{1}{4\pi^2 D_s\xi^2}}}{\Gamma_{solid}} \\
&= \frac{\frac{1}{\frac{1}{16\pi^4\left(\frac{E}{1-\nu^2}\frac{\frac{1}{12}(b_o h_o^3 - b_i h_i^3)}{b_o}\right)\xi^4}+\frac{1}{4\pi^2\left(\frac{E}{2(1+\nu)}\right)h'_o\,\xi^2}}}{\Gamma_{solid}} \\
&= \frac{\frac{1}{\frac{1}{16\pi^4\left(\frac{E}{1-\nu^2}\frac{\frac{1}{12}(b_o h_o^3 - b_i h_i^3)}{b_o}\right)\xi^4}+\frac{1}{4\pi^2\left(\frac{E}{2(1+\nu)}\right)h'_o\,\xi^2}}}{\frac{1}{\frac{1}{16\pi^4\left(\frac{E}{1-\nu^2}\frac{\frac{1}{12}b_o h_o'^3}{b_o}\right)\xi^4}+\frac{1}{4\pi^2\left(\frac{E}{2(1+\nu)}\right)h'_o\,\xi^2}}} \\
&= \frac{\frac{1}{\frac{1}{16\pi^4\left(\frac{E}{1-\nu^2}\frac{\frac{1}{12}(b_o h_o^3 - b_i h_i^3)}{b_o}\right)\xi^4}+\frac{1}{4\pi^2\left(\frac{E}{2(1+\nu)}\right)\left(\frac{b_o^2 h_o - b_i^2 h_i}{b_o^2}\right)\xi^2}}}{\frac{1}{\frac{1}{16\pi^4\left[\frac{E}{1-\nu^2}\frac{1}{12}\left(\frac{b_o^2 h_o - b_i^2 h_i}{b_o^2}\right)^3\right]\xi^4}+\frac{1}{4\pi^2\left(\frac{E}{2(1+\nu)}\right)\left(\frac{b_o^2 h_o - b_i^2 h_i}{b_o^2}\right)\xi^2}}}.
\end{aligned}
\tag{4.5}
$$

Equation 4.5 looks like an intimidating expression, but it *is* very useful! All of the steps leading up to it are simply algebraic substitution, and I included them to clarify how I arrived at the answer. There are two items which may warrant additional explanation:

- Line three numerator: $\frac{I}{b_o}$. b_o is the width of the unit cell, as shown in Figure 4.7.
- The shear stiffness D_s is the *same* for both the lightweighted and solid cases. This is because I am normalizing the lightweighted mirror to a solid mirror of equal mass. The shear stiffness depends only on the amount of material present—not the geometry—so the value of D_s is equivalent in both cases.[9] As such, I define the effective thickness h_o' as follows:

$$\begin{aligned} m_{LW} &= m_{solid} \\ \rho\, V_{LW} &= \rho\, V_{solid} \\ V_{solid} - V_{empty} &= V_{solid} \\ b_o^2\, h_o - 4\, h_i \left(\frac{b_i}{2}\right)^2 &= V_{solid} \\ (b_o^2\, h_o - b_i^2\, h_i) &= b_o^2\, h_o' \\ h_o' &= \frac{b_o^2\, h_o - b_i^2\, h_i}{b_o^2}. \end{aligned}$$

  The effective thickness is the height of the solid plate. It represents all of the mass that is within each structure.

I can now use Equation 4.5 to investigate how the structural efficiency changes as a solid plate is lightweighted using the sandwich geometry. First, however, it will be helpful to define what I mean when I say that a structure "is lightweighted". The basic idea is simple: I'd like to show what happens to the structural efficiency ratio as I start removing material from a solid plate. For the sandwich geometry, I will always remove material using the same procedure.

[9] If I normalized the lightweighted plate to an equivalent plate of *equal thickness*—which I am not—then the respective values for D_s would be different because each plate would contain a different amount of material.

FIGURE 4.8. Lightweighting the sandwich geometry. In this example, the ratio of the facesheet to rib thickness is equal to one ($TR = 1$). Thus, the facesheet and rib thickness remain equal as the cell is lightweighted.

Figure 4.8 illustrates the most efficient way to gradually remove material from a solid cell to create a sandwich cell. The mass is initially removed along the neutral axis because this contributes the least to the sandwich structure's stiffness. (The material near the very top and bottom—the I sections of the I-beam—contribute the most to the stiffness.) While removing material, I maintain a constant proportion between the facesheet and rib thickness. I define this thickness ratio (TR) as follows:

$$\begin{aligned} TR &= \frac{t_{\text{facesheet}}}{t_{\text{rib}}} \\ &= \frac{\frac{h_o - h_i}{2}}{b_o - b_i}, \end{aligned} \tag{4.6}$$

where h_o, b_o, h_i, and b_i are shown in Figure 4.7. For example, if I set $TR = 3$, then the facesheet will always remain three times thicker than the rib.[10]

By using the thickness ratio, I can easily generate a plot of the structural efficiency ratio as a function of lightweightedness. There are four variables that define the geometry: b_o, h_o, b_i, and h_i. I'm going to choose the values for TR, b_o, and h_o. In order to lightweight the structure, the independent variable will be h_i, which will vary from zero to h_o. For every h_i, I will calculate b_i using Equation 4.6.

Figure 4.9 shows how the structural efficiency changes as a solid plate is lightweighted. The percent lightweightedness (% LW) is plotted along the x-axis, and

[10]For another example of thickness ratio, Figure 4.9 shows a unit cell where $TR = 1$.

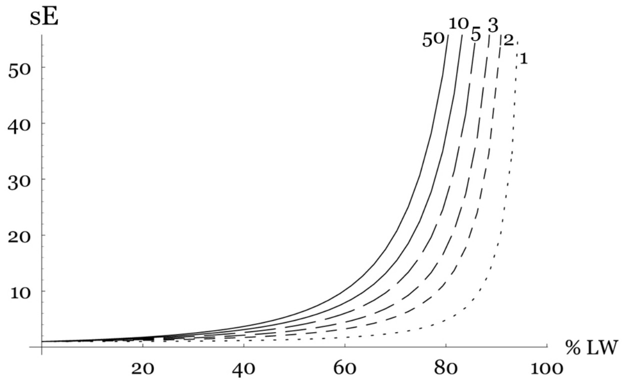

FIGURE 4.9. Structural efficiency (sE) for a sandwich structure as a function of lightweightedness (% LW). For this example, I used BK7 ($\nu = 0.206$) and a unit cell with outer dimensions $b_o = 1$ in and $h_o = 2$ in. $\xi = 1/10\,\frac{1}{\text{in}}$. The different curves represent different facesheet to rib thicknesses. For example, the line labeled "5" is for a sandwich geometry where the facesheet thickness is held at five times the rib thickness as the unit cell is lightweighted.

the structural efficiency (sE) is plotted along the y-axis. The different curves each represent a different thickness ratio. For example, the curve labeled "5" is for a geometry where the facesheet thickness is held at five times the rib thickness as the unit cell is lightweighted. This plot illustrates three important conclusions about lightweighting schemes using the sandwich geometry:

- First, there are geometries where *little or no structural efficiency is gained* by using a lightweighted shell over a solid shell of equal mass. For example, the curve labeled "1" (TR = 1, or the facesheet thickness is the same as the rib thickness) shows very little increase in sE until the unit cell is over 70% lightweighted.

- Second, using *a thinner rib always results in a better structural efficiency ratio* for the same % LW. For example, in this plot, a shell that maintains a facesheet that is ten times thicker than the ribs (TR=10) will have a structrual efficiency ratio of 10 when the unit cell is 65 % lightweighted. A shell that has equal rib and facesheet thickness (TR=1) needs to be 85% lightweighted to achieve the same structural efficiency.

- Most important, the *structural efficiency increases* as the material is lightweighted.

Figure 4.9 represents a particular geometry of unit cell parameters: $b_o = 1$ in, $h_o = 2$ in, and $\xi = 1/10$ 1/in. I also assumed that I was using BK7, a standard-grade optical glass. (This sets the Poisson ratio, $\nu = 0.206$.)[11] The following rules apply if any of these constants are changed as follows:

- b_o is increased. Doing this effectively spaces the ribs farther apart. Increasing b_o increases the sE for a given % LW. For example, for $\mathbf{b_o = 1}$ **in**, $h_o = 2$ in, $TR = 1$, $\nu = 0.206$, and $\xi = 1/10$ 1/in, $sE \approx 6$ at 60% LW. For $\mathbf{b_o = 10}$ **in**, $h_o = 2$ in, $TR = 1$, $\nu = 0.206$, and $\xi = 1/10$ 1/in, $sE \approx 7.5$ at 60% LW.

- h_o and b_o are scaled up by the same factor. Increasing h_o and b_o by the same scaling factor decreases the sE for a given % LW. For example, for $\mathbf{b_o = 1}$ **in**, $\mathbf{h_o = 2}$ **in**, $TR = 1$, $\nu = 0.206$, and $\xi = 1/10$ 1/in, $sE \approx 6$ at 60% LW. For $\mathbf{b_o = 4}$ **in**, $\mathbf{h_o = 8}$ **in**, $TR = 1$, $\nu = 0.206$, and $\xi = 1/10$ 1/in, $sE \approx 2$ at 60% LW. This result may seem counterintuitive, but the ratio of the moments of inertia does not double if the unit cell's dimensions are doubled.

- ξ is increases. Increasing ξ decreases the sE for a given % LW. For example, for $b_o = 1$ in, $h_o = 2$ in, $TR = 1$, $\nu = 0.206$, and $\boldsymbol{\xi = 1/10}$ **1/in**, $sE \approx 5.5$ at 60% LW. For $b_o = 1$ in, $h_o = 2$ in, $TR = 1$, $\nu = 0.206$, and $\boldsymbol{\xi = 1/4}$ **1/in**, sE ≈ 3 at 60% LW.

- ν increases. (Increasing the Poisson ratio results in using a material that is essentially more rubbery. See Section 2.1.3.) Increasing ν decreases the sE for

[11] It's interesting to note that Young's modulus E drops out of Equation 4.5, and it isn't necessary to specify E in order to solve the problem.

Parameter (change)	Effect on sE for a given % LW
b_o (+)	Increase
h_o, b_o (scaled up)	Decrease
ξ (+)	Decrease
ν (+)	Decrease
TR (+)	Increase
% LW (+)	Increases

TABLE 4.2. Summary of effects on sE for the sandwich geometry. By far, the easiest way to increase the structural efficiency is to increase the % LW. By comparison, the other factors have little effect.

a given % LW. For example, for $b_o = 1$ in, $h_o = 2$ in, $TR = 1$, $\boldsymbol{\nu} = \mathbf{0.206}$, and $\xi = 1/10$ 1/in, $sE \approx 5.7$ at 60% LW. For $b_o = 1$ in, $h_o = 2$ in, $TR = 1$, $\boldsymbol{\nu} = \mathbf{0.5}$, and $\xi = 1/10$ 1/in, $sE \approx 5.0$ at 60% LW.

These rules are summarized in Table 4.2.

4.2.3 Optimized design: openback geometry

I can perform a similar analysis on the openback geometry, shown in Figure 4.1. However, the openback scheme is more involved than the sandwich geometry because it is not symmetric about any horizontal axis. As a result, the algebra will be more involved for this situation. The conclusions, however, are far more dramatic than for the sandwich geometry.

As in the previous section, I will use Equation 4.4 as the starting point. The unit cell for the openback geometry looks like the letter "T", as shown in Figure 4.10. As with the case of the sandwich geometry, I need the moment of inertia for this cell. The cross section shown in Figure 4.10 is not symmetric about a horizontal axis, and this requires some extra steps when calculating the moment of inertia, I. Unlike an I-beam, the location of the center of mass changes as the facesheet or rib thickness is changed. This results in an expression for the moment of inertia that is more

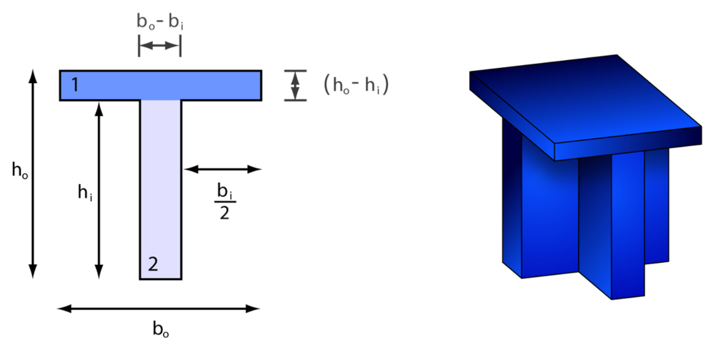

FIGURE 4.10. 2D and 3D drawings for the openback unit cell. Left: the 2D drawing has been divided up into two smaller pieces for solving the moment of inertia for this geometry. This is the scheme that I will use for calculating the center of mass.

complicated than that of the I-beam.[12] The following paragraphs derive the moment of inertia for an openback unit cell.

The moment of inertia depends on the location of the center of mass, and this is the first quantity that must be calculated. Figure 4.10 shows the geometry of a T cell. The following equation is used to find the center of mass: [19]

$$\begin{aligned} \langle\vec{r}\rangle = \frac{\int \vec{r}\,dm}{m} &= \frac{(\frac{h_i}{2})(b_o - b_i)h_i + \left[h_i + \frac{(h_o-h_i)}{2}\right](h_o - h_i)(b_o)}{(b_o - b_i)h_i + (h_o - h_i)b_o} \\ \langle\vec{r}\rangle &= \frac{b_o h_o^2 - b_i h_i^2}{2\,b_o h_o - 2\,b_i h_i}. \end{aligned} \tag{4.7}$$

The location of the center of mass for a T cell is $\frac{b_o h_o^2 - b_i h_i^2}{2\,b_o h_o - 2\,b_i h_i}$ units above the base of the cell.

To simplify matters, I will calculate the moments of inertia for the top and bottom pieces separately. The line drawing in Figure 4.10 shows that the unit cell is easily divisible into two rectangles. By doing this, the individual centers of mass can be calculated and then combined for the net center of mass. Because both pieces are

[12]Because of this, the expression for I is rarely found in textbooks. However, it is simple enough to calculate.

rectangles, this relationship can be used as a starting point: $I_{\text{rect}} = \frac{bh^3}{12}$. The moments for rectangles 1 and 2 are

$$\begin{aligned} I_1 &= \frac{1}{12}\, b_o\,(h_o - h_i)^3 \quad \text{and} \\ I_2 &= \frac{1}{12}\,(b_o - b_i) h_i^3. \end{aligned}$$

Now I will transfer[13] each moment to the neutral axis, which contains the center of mass[14] (Equation 4.7: $\frac{b_o h_o^2 - b_i h_i^2}{2\, b_o h_o - 2\, b_i h_i}$):

$$\begin{aligned} I_1 &= \overline{I_1} + A\, d^2 \\ I_1 &= \frac{1}{12}\, b_o\,(h_o - h_i)^3 + (h_o - h_i)\, b_o \left[h_o - \frac{(h_o - h_i)}{2} - \frac{b_o h_o^2 - b_i h_i^2}{2\, b_o h_o - 2\, b_i h_i} \right]^2 \\ I_2 &= \frac{1}{12}\,(b_o - b_i)\, h_i^3 + (b_o - b_i)\, h_i \left[\frac{h_i}{2} - \frac{b_o h_o^2 - b_i h_i^2}{2\, b_o h_o - 2\, b_i h_i} \right]^2. \end{aligned}$$

The total moment of inertia is the sum of I_1 and I_2:

$$\begin{aligned} I &= \frac{1}{12}\, b_o\,(h_o - h_i)^3 + \frac{1}{12}\,(b_o - b_i) h_i^3 + h_i (b_o - b_i) \left(\frac{h_i}{2} - \frac{b_o h_o^2 - b_i h_i^2}{2\, b_o h_o - 2\, b_i h_i} \right)^2 \\ &+ b_o\,(h_o - h_i) \left(h_o + \frac{1}{12}(h_i - h_o) - \frac{b_o h_o^2 - b_i h_i^2}{2\, b_o h_o - 2\, b_i h_i} \right)^2. \end{aligned} \tag{4.8}$$

I can now substitute Equation 4.8 into Equation 4.4. In order to prevent the algebra from consuming the page, I will represent Equation 4.8 as $I(b_o, h_o, b_i, h_i)$:

[13]The procedure for transfer of axes is reviewed in Section 2.3.2.

[14]For pure bending, the centroidal axis coincides with the neutral axis. Timoshenko provides a proof of this on page 95 in *Strength of Materials, Part I.* [24]

FIGURE 4.11. Lightweighting the openback geometry. As material is removed, the ratio of the rib to unit cell width remains constant. (In this example, $R_r = 0.25$. The rib width is 25% the unit cell's width.)

$$
\begin{aligned}
sE &= \frac{\Gamma_{LW}}{\Gamma_{solid}} \\
&= \frac{\frac{1}{\frac{1}{16\pi^4 D\xi^4}+\frac{1}{4\pi^2 D_s\xi^2}}}{\Gamma_{solid}} \\
&= \frac{\frac{1}{\frac{1}{16\pi^4\left(\frac{E}{1-\nu^2}\frac{I(b_o,h_o,b_i,h_i)}{b_o}\right)\xi^4}+\frac{1}{4\pi^2\left(\frac{E}{2(1+\nu)}h_o'\right)\xi^2}}}{\Gamma_{solid}} \\
&= \frac{\frac{1}{\frac{1}{16\pi^4\left(\frac{E}{1-\nu^2}\frac{I(b_o,h_o,b_i,h_i)}{b_o}\right)\xi^4}+\frac{1}{4\pi^2\left(\frac{E}{2(1+\nu)}h_o'\right)\xi^2}}}{\frac{1}{\frac{1}{16\pi^4\left(\frac{E}{1-\nu^2}\frac{\frac{1}{12}b_o h_o'^3}{b_o}\right)\xi^4}+\frac{1}{4\pi^2\left(\frac{E}{2(1+\nu)}h_o'\right)\xi^2}}} \\
&= \frac{\frac{1}{\frac{1}{16\pi^4\left(\frac{E}{1-\nu^2}\frac{I(b_o,h_o,b_i,h_i)}{b_o}\right)\xi^4}+\frac{1}{4\pi^2\left(\frac{E}{2(1+\nu)}\left(\frac{b_o^2h_o-b_i^2h_i}{b_o^2}\right)\right)\xi^2}}}{\frac{1}{\frac{1}{16\pi^4\left[\frac{E}{1-\nu^2}\frac{1}{12}\left(\frac{b_o^2h_o-b_i^2h_i}{b_o^2}\right)^3\right]\xi^4}+\frac{1}{4\pi^2\left(\frac{E}{2(1+\nu)}\left(\frac{b_o^2h_o-b_i^2h_i}{b_o^2}\right)\right)\xi^2}}}.
\end{aligned}
\tag{4.9}
$$

Equation 4.9 contains a considerable number of terms, but it will produce some powerful conclusions. It is similar to Equation 4.5; as such, refer to that derivation for explanations of the $\frac{I(b_o,h_o,b_i,h_i)}{b_o}$ and D_s terms.

In Section 4.2.2, I used the thickness ratio (TR) to help define how I lightweighted the sandwich unit cell. I will define an analogous convention for the openback case, but it is *very different* from the thickness ratio.[15]

[15]It's very different because the geometries are very different, and it doesn't make any sense to use the TR in this case. Instead, I will define a different ratio.

Figure 4.11 shows the convention that I will use for removing material from the openback geometry. The mass is initially removed from the lower right and lower left corners because this is how it would be done using traditional lightweighting techniques like water-jet milling.[16] While removing material, I will maintain a constant rib thickness. To make matters simpler, I will define the rib width as a function of the total cell width:

$$R_r = (1 - b_i/b_o)\,, \tag{4.10}$$

where R_r is defined as the *rib ratio*. For example, if $R_r = 0.2$, then the rib is 20% as wide as the unit cell. As I remove material from the openback's unit cell, R_r (and therefore the rib thickness) will remain constant. For example, as material is removed from the unit cell in Figure 4.11, the rib width remains constant.

I can use Equation 4.9 to look at how the structural efficiency varies as a plate is lightweighted using the openback geometry. Figure 4.12 shows how the sE varies as the unit cell is lightweighted. The parameters of the unit cell are $b_o = 10$ in, $h_o = 1$ in, $R_r = 0.5$ in, and $\xi = 1/10$ 1/in.

The results are very different when compared to the sandwich geometry. First, when this unit cell is between 0 and 11% lightweighted, the structural efficiency of the openback structure is *worse* than a solid plate of equivalent mass. Why does this happen? As I mentioned above, the material that is farthest away from the neutral axis provides the greatest contribution to the stiffness. This means that the material at the top and bottom of the unit cell provide the most stiffness per unit mass. When this material is removed (using the scheme shown in Figure 4.11), the structural efficiency will decrease because this material provides a big contribution to the stiffness. Eventually, the material that is removed comes from the middle of the unit cell, and this material doesn't contribute very much to the cell's structural

[16] Note! Unlike in Section 4.2.2, this is *not* the most structurally efficient way to remove the material. It is, however, the most *practical* way to do it using today's pocketmilling techniques.

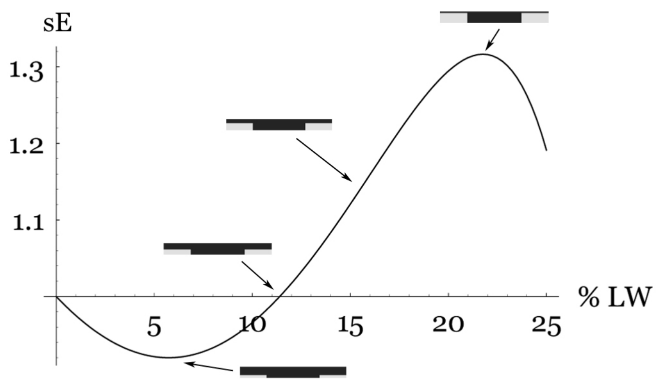

FIGURE 4.12. Structural efficiency (sE) for an openback structure as a function of lightweightedness (% LW). I also include the approximate illustration of the unit cell for a few points. Note that the rib width remains constant as material is removed. (In this case, $R_r = 0.5$ so the rib width remains 50% that of the cell width.) For this geometry, the optimum structural efficiency is obtained when the unit cell is lightweighted by 22%.

stiffness. As such, the structural efficiency ratio will increase. Finally, there is a particular % LW at which the structural efficiency reaches a maximum. For the openback structure, this means there is one value for h_i that yields the best sE ratio. After the maximum, the structural efficiency starts to decrease again because material is removed from the very top part of the cell.

Figure 4.12 is for a single set of b_o, h_o, and R_r. For this particular combination of values, there is a value for h_i that maximizes the structural efficiency. How does this ideal value of h_i change for other sets of b_o, h_o, and R_r? This information is shown in Figure 4.13.

The left side of Figure 4.13 shows the percent lightweighedness (% LW) required to maximize the structural efficiency ratio for a given rib thickness (R_r). For example, when $(1 - R_r) = 0.8$ (the rib is 20 % of the cell width), the maximum sE ratio will occur when the unit cell is 60% lightweighted.

The right side of Figure 4.13 shows the maximum structural efficiency ratio that is possible for a given rib thickness (R_r). For example, when $(1 - R_r) = 0.8$, the max-

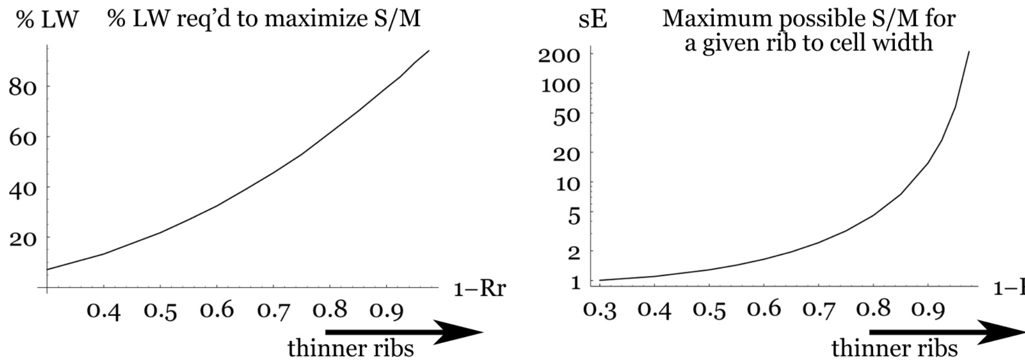

FIGURE 4.13. Left: The % lightweightedness required to maximize the structural efficiency as a function of R_r. This plot shows how much the unit cell must be lightweighed to achieve the maximum sE for a particular rib width. Right: The maximum possible structural efficiency as a function of R_r. This plot shows the maximum possible sE for a particular rib width.

imum possible sE is five times that of a solid plate of equivalent mass. (And, looking at the previous paragraph, this occurs when the unit cell is 60% lightweighted.)

In summary, Figures 4.12 and 4.13 illustrate three important conclusions about lightweighting schemes that use the openback geometry:

- There are geometries where the *structural effciency for a lightweighted plate is worse* than that of a solid plate of equal mass. This occurs when the unit cell is only lightweighted by 5 or 10%. Using a large value (> 0.50, thicker ribs) of R_r can intensify this effect. For geometries with a value of R_r near unity, a structural efficiency advantage is *never* gained.

- Unlike the sandwich geometry, there is a *particular % LW that maximizes the structural efficiency ratio* for a given set of h_o, b_o, ξ, and R_r. For a particular set of these parameters, the designer should choose the % LW that maximizes the structural efficiency. Every other choice for % LW results in an un-optimized design.

- Using *a thinner rib always results in a higher possible structural efficiency.* Most geometries will experience a significant increase in sE when R_r is less than 0.2. The maximum possible sE increases with a linear decrease in rib thickness.

Finally, note that Figures 4.12 and 4.13 are for a particular combination of b_o and h_o: $b_o = 10$ in, $h_o = 1$ in, $\xi = 1/10$ 1/in, and $\nu = 0.206$ (BK7). Because Figure 4.12 contains an inflection point, I cannot create a list of scaling laws for each of the physical parameters as I did in Table 4.2 for the sandwich geometry. As such, if a design engineer is interested in a particular geometry, it would be best to do the calculation for his specific case. Section 4.2.4 contains an example for an openback aluminum structure.

4.2.4 Two practical examples

Example using a sandwich geometry: An engineer is asked to analyze a sandwich mirror made from OHara's E6 glass ($\nu = 0.195$), with the following unit cell parameters: $b_o = 4$ in, $h_o = 0.5$ in, and $TR = 1$. I will assume that $\xi = 1/10$ 1/in.

Section 4.2.2 shows that there isn't an ideal unit cell geometry that will maximize the structural efficiency. (The sE will approach infinity as % LW approaches 100.) However, I can create a plot that shows how the structural efficiency changes as the material is lightweighted.[17] To do this, I will generate a list of h_i values that range from 0 to h_o. For each h_i point, I will calculate the % LW using this relationship:

$$\%\ LW_{\text{sand}} = (1 - \frac{b_o^2 h_o - b_i^2 h_i}{b_o^2 h_o}) \times 100. \tag{4.11}$$

Next, I will use Equation 4.5 to calculate the sE for each h_i. (Equation 4.6 is used to calculate a b_i from each h_i.) Finally, I will plot the sE values against the % LW values. This plot is shown in Figure 4.14. As expected, the sE advantage increases with increased lightweightedness.

[17] This plot will be similar to Figure 4.9.

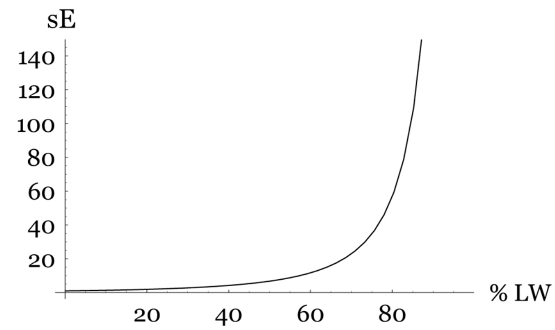

FIGURE 4.14. Structural efficiency (sE) for a sandwich structure as a function of lightweightedness (% LW). This plot is for an example using E6 glass ($\nu = 0.195$), and a unit cell with dimensions $b_o = 4$ in, $h_o = 0.5$ in, and $TR = 1$. $\xi = 1/10$ 1/in.

Let's suppose that the structure should be 20 times stiffer than a solid plate of equivalent mass. Figure 4.14 shows that this occurs when the unit cell is about 67% lightweighted. What are the values of b_i and h_i when the unit cell is 67% lightweighted? I will use Equations 4.6 and 4.11 to find these values:

$$
\begin{aligned}
TR = \frac{\frac{h_o - h_i}{2}}{b_o - b_i} &= 1 \\
\frac{\frac{0.5 - h_i}{2}}{4 - b_i} &= 1 \\
h_i &= 0.5 - 2(4 - b_i) \\
\%\ LW_{\text{sand}} = (1 - \frac{b_o^2 h_o - b_i^2 h_i}{b_o^2 h_o}) \times 100 &= 67 \\
(1 - \frac{4^2 \cdot 0.5 - b_i^2 \cdot [0.5 - 2(4 - b_i)]}{4^2 \cdot 0.5}) \times 100 &= 67 \\
b_i &= 3.92 \text{ in} \\
h_i &= 0.348 \text{ in.}
\end{aligned}
$$

In conclusion, the structure will be 20 times stiffer than a solid plate of equivalent mass when $b_o = 4$ in, $h_o = 0.5$ in, $b_i = 3.92$ in, and $h_i = 0.348$ in.

Example using an openback geometry: An engineer is asked to analyze an openback mirror made from 6061-T6 aluminum ($\nu = 0.33$) with the following unit cell parameters: $b_o = 6$ in, $h_o = 1$ in, and $R_r = 0.1$. I will assume that $\xi = 1/10$ 1/in.

What are the inside dimensions b_i and h_i that result in the optimum structural efficiency ratio? To answer this question, I will generate a plot similar to that of Figure 4.12. First I will create a list of h_i values ranging from 0 to h_o. Then, I will substitute each of these h_i values into Equation 4.9 to calculate the structural efficiency at each point. (Note that I will use Equation 4.10 to calculate a b_i at each h_i.) Next, I will calculate the % LW at each h_i using the following relationship:

$$\%\ LW_{\text{open}} = (1 - \frac{b_o^2 h_o - b_i^2 h_i}{b_o^2 h_o}) \times 100. \tag{4.12}$$

Finally, I will plot the sE values against the % LW values. This plot is shown in Figure 4.15. The optimum structural efficiency occurs when the unit cell is 79% lightweighted. I can calculate the inside dimensions b_i and h_i by using Equations 4.10 and 4.12 and substituting the values of b_o, h_o and R_r:

$$\begin{aligned}
R_r = \left(1 - \frac{b_i}{b_o}\right) &= 0.1 \\
1 - \frac{b_i}{6} &= 0.1 \\
b_i &= 5.4 \text{ in} \\
\%\ LW_{\text{open}} = (1 - \frac{b_o^2 h_o - b_i^2 h_i}{b_o^2 h_o}) \times 100 &= 79 \\
(1 - \frac{6^2 \cdot 1 - 5.4^2 \cdot h_i}{6^2 \cdot 1}) \times 100 &= 79 \\
h_i &= 0.975 \text{ in}
\end{aligned}$$

When the unit cell is lightweighted by 79% (this is equivalent to unit cell dimensions $b_o = 6$ in, $h_o = 1$ in, $b_i = 5.4$ in, and $h_i = 0.975$ in), the openback structure will be 16.5 times stiffer than a solid structure of equivalent mass. As suggested by

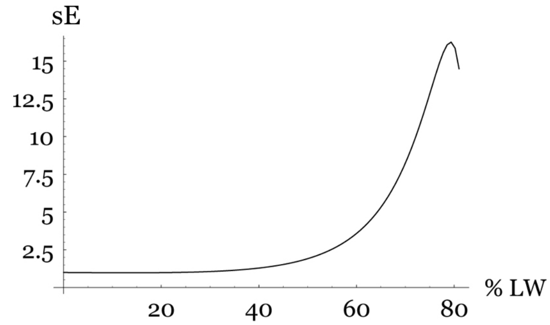

FIGURE 4.15. Structural efficiency (sE) for an openback structure as a function of lightweightedness (% LW). This plot is for an example using aluminum 6061-T6 ($\nu = 0.33$), and a unit cell with dimensions $b_o = 6$ in, $h_o = 1$ in, and $R_r = 0.1$. $\xi = 1/10$ 1/in.

Figure 4.13, the stiffness can be improved by using a smaller value for R_r (a thinner rib).

4.2.5 Design note: bending versus shear at different spatial frequencies

Throughout this chapter, I calculated the plate stiffness as a function of structural geometry. Equation 4.3 includes the effects of both bending and shear, but I haven't mentioned the situations where the deflection is dominated by either bending or shear. For example, Figure 4.16 shows two beams of different lengths. When a downward force is exerted at the end of the longer beam, the deflection is caused mostly by bending. By contrast, when a force is exerted at the end of the short beam, the deflection caused mostly by shear. Clearly, there are geometries where either bending or shear is the dominate cause of the deflection.

The mathematics describing the two scenarios shown in Figure 4.16 is shown below. The shear deflection scales linearly with the beam length, while the bending deflection is proportional to the cube of the beam length:

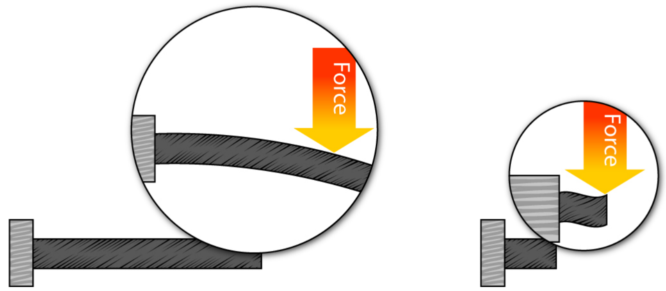

FIGURE 4.16. Bending versus shear deflection for different geometries. Left: the long beam deflects due to mostly bending effects. Right: the short, stubby beam deflects due to mostly shear. This is because shorter beams are more difficult to bend with the same amount of force, so the shear effect is more apparent in the stubby beam.

$$\begin{aligned}\Delta y_{\text{shear}} &= \frac{F}{AG} \cdot l \\ \Delta y_{\text{bending}} &= \frac{F}{3EI} \cdot l^3,\end{aligned}$$

where A is the cross-sectional area, G is the shear modulus, E is Young's modulus, I is the moment of inertia, and F is the downward force at the end of the beam of length l. These equations emphasize that bending is the dominant deflection at longer beam lengths.

Over which geometries does bending or shear dominate for the sandwich and openback geometries? The left side of Figure 4.17 shows the spatial frequencies for which bending and shear compliance are *equal* as the unit cell is lightweighted.[18] Shear dominates in the upper left region and bending dominates in the lower right region. As the value of $\%LW$ approaches 100, the material that is removed comes from the flanges of the I-beam, and this material contributes the most to the bending stiffness. The bending stiffness drops off significantly, and the structure is dominated

[18]Note that the overall cell dimensions b_o and h_o remain the same as the cell is lightweighted. Figure 4.17 was generated from the following unit cell parameters: $b_o = 1$ in, $h_o = 2$ in, and $TR = 1$. Recall that $TR = 1$ means that the rib has the same thickness as the facesheet as the unit cell is lightweighted. Larger values of TR mean the rib is proportionally thinner. For example, when $TR = 5$, the rib is 5 times thinner than the facesheets as the unit cell is lightweighted.

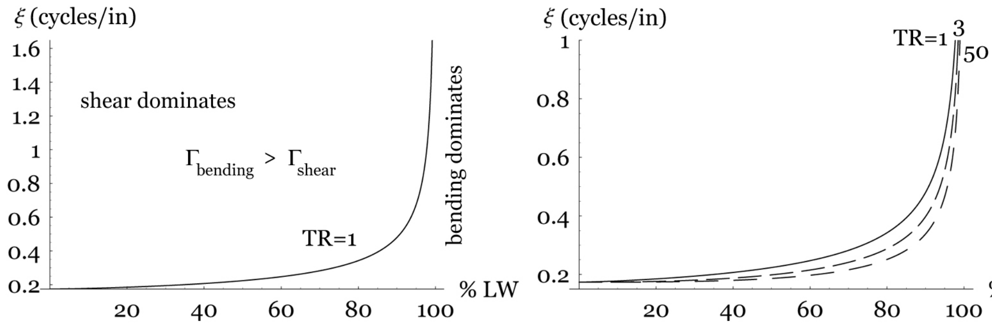

FIGURE 4.17. Spatial frequencies where bending and shear stiffnesses are equal for a sandwich cell of constant height. Left: This plot is for $b_o = 1$ in, $h_o = 2$ in, and $TR = 1$. Right: This plot is for different values of TR. (Recall TR determines the rib thickness. For example, when $TR = 3$, the rib is 3 times thinner than the facesheets as the unit cell is lightweighted.)

by bending deflection. The right side of Figure 4.17 shows the same information, except each plot represents a different value for TR.

Figure 4.18 is an analogous plot for the openback structure. It shows the spatial frequencies where bending and shear compliance are equal as the unit cell is lightweighted. (Again, the unit cell height remains constant as the cell is lighweighted.) The left side of Figure 4.18 was generated from the following unit cell parameters: $b_o = 5$ in, $h_o = 1$ in, and $R_r = 0.1$. (Recall that $R_r = 0.1$ means that the rib width is held at 10% of the unit cell width.)

This plot looks different than Figure 4.17 because the mass removal affects the stiffness in a different manner. At first, the material is removed from the bottom of the cell (as illustrated in Figure 4.11), and this results in a drastic reduction in stiffness. As the material near the middle of the unit cell is removed, the stiffness isn't affected as much; this is shown in Figure 4.18 as the region with zero slope. Finally, the material removal comes from the top section of the "T", and the stiffness is drastically affected once again.

The right side of Figure 4.18 shows the same information for different rib thick-

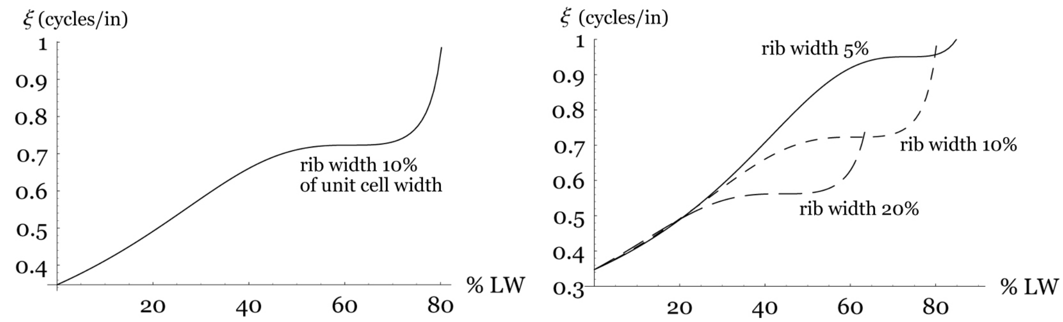

FIGURE 4.18. Spatial frequencies where bending and shear stiffnesses are equal for an openback cell of constant height. Left: This plot is for $b_o = 5$ in, $h_o = 1$ in, and $R_r = 0.9$. Right: This plot is for different values of R_r.

nesses. Note that, as the rib thickness is increased, the cell cannot be lightweighted as much.

4.2.6 Design note: sandwich versus openback

The two geometries discussed in this chapter are very different from each other. The sandwich structure's backsheet allows it to be significantly stiffer than an openback structure of equivalent mass. As a result, it isn't fair to compare the stiffnesses of the two geometries: for the same amount of mass, the sandwich structure is always better. However, it is instructive to look at just how *much* better the sandwich structure is over the openback geometry.

I considered an example unit cell, with outer dimensions $b_o = 5$ and $h_o = 1$. For the sandwich structure, I allowed the thickness ratio TR to be 1. (The rib and the facesheet will remain at equal thickness as the unit cell is lightweighted.) The rib ratio R_r for the openback structure was set at 0.1. (The rib is 10% of the unit cell width.) I assumed that $\xi = 1/10$. The results are shown in Figure 4.19.

For small lightweighting percentages ($< 20\%$), there is a relatively small difference between the openback and sandwich structures. However, as the structures are lightweighted, the sandwich's structural efficiency increases. When lightweighted by

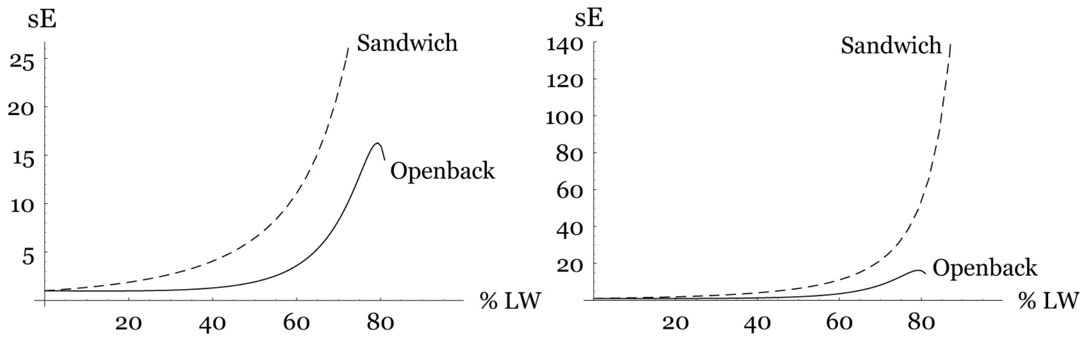

FIGURE 4.19. Comparison between the sandwich and openback geometries. This comparison is for unit cells with the same overall thickness, $h_o = 1$. The two plots both show the same data; the plot on the right shows a larger range for the sE. These figures emphasize the structural efficiency advantage that the sandwich geometry has over the openback when the unit cell is lightweighted more than 80%.

80%, the sandwich structure is about 3.5 times stiffer than an openback structure of equal mass.

Ultimately, the decision to use an openback or sandwich structure will depend on several factors: what the structure will be used for; the availability of the fabrication equipment; the previous experiences of the design and fabrication team; and the allowances for schedule and budget.

4.2.7 Design note: alternative geometries

Throughout this chapter, I only discuss lightweighting schemes that use square cells. There are, however, lightweighting geometries that use hexagon or triangular cells. Why did I only analyze the square schemes? First, the square cells possess a symmetry that result in simple expressions for the moment of inertia I. For example, for the sandwich geometry, I was able to use the moment of inertia of an I-beam. This resulted in an intuitive approach that didn't require the use of finite-element analysis.

There is evidence in the literature that suggests that it *doesn't matter* which rib geometry is used! Ralph M. Richard has shown that—for mirrors using square, triangular, and hexagonal sandwich cells—the stiffnesses are nearly equivalent if the same amount of mass is used in each mirror. He notes that the "structural deformations for all ... mirror models [are] isotropic and essentially identical". [22] Richard performed two finite-element analyses using constant-stress, linear-edge displacement membrane triangles and rectangular bending elements. (The two analyses were within 2% of one another.) He concludes that the deformation is isotropic provided that the cell size is small compared to the mirror diameter.

4.3 Chapter summary

In this chapter I discussed the two lightweighting schemes shown in Figure 4.1. I analyzed the structural efficiency behavior for each geometry, and I came to the following conclusions:
Sandwich Geometry:

- When compared to a solid plate of equal mass, the structural efficiency ratio of a sandwich structure increases as the plate is lightweighted.
- Most sandwich geometries do not experience a significant advantage (10X) over a solid plate until the sandwich is over 50% lightweighted.
- Thinner ribs always result in better structural efficiency.

Openback Geometry:

- For most openback geometries, there is a combination of unit cell dimensions that will provide an optimum solution for maximizing the structural efficiency ratio.
- There are geometries where the stiffness can be *worse* than that of a solid plate of equal mass.

- Thinner ribs always result in better structural efficiency.

I also discussed the following helpful design notes:

- Table 4.2 shows how changing individual sandwich unit cell parameters affects the structural efficiency.
- Section 4.2.4 provides two real-world examples. I look at an E6 sandwich geometry and an aluminum openback structure.
- Section 4.2.6 provides an example that illustrates how much stiffer a sandwich structure is over an openback structure.

Chapter 5

NMSD: the UA two meter NGST demonstration mirror

The University of Arizona's NMSD mirror was an ambitious project: at two meters in diameter, it was going to be the largest high-authority glass mirror that anyone had ever built. The mirror was built as a technology demonstration for the James Webb Space Telescope, the successor to the Hubble Space Telescope that is scheduled to launch in 2011. In this chapter, I begin by briefly describing the fabrication process. My specific role in the project was as the metrology engineer, and the bulk of this chapter describes the schemes that I used to measure and control the mirror.

5.1 Design and fabrication

A cartoon of the NMSD mirror is shown in Figure 5.1. The F/5 glass membrane is 2 meters in diameter (point-to-point), and it is 2 mm thick. The glass is supported by 166 actuators: 39 edge actuators are coupled directly to the glass, and the central 127 actuators are coupled to the glass via a nine-point loadspreader. (The actuators are remotely-controlled via a separate electronics system.) The support is maintained by a lightweight, carbon-fiber/epoxy reaction structure. All of these components combine to form a mirror system that weighs only 86 pounds. In addition to these specifications, the mirror was designed and built to work at cryogenic temperatures.

The NMSD mirror was an important project because it allowed the university to bring several of its research areas—thin glass fabrication, actuator development, and structural design—to maturity. This section highlights some of the important technical aspects of the fabrication process.

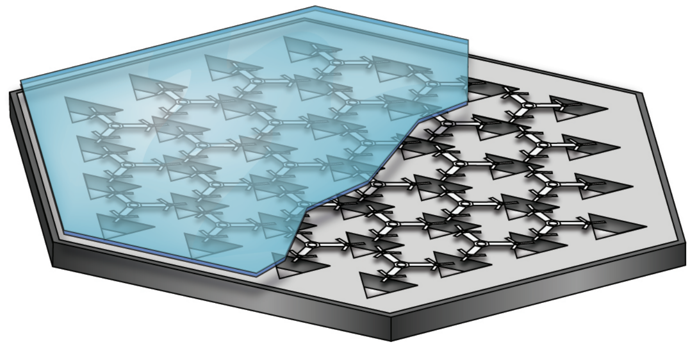

FIGURE 5.1. The University of Arizona NMSD 2 m prototype. The F/5 glass membrane is two meters point-to-point and 2 mm thick. The membrane is supported by 166 actuators. The entire structure, including the glass, actuators, support structure, loadspreaders, and all of the onboard wiring, weighs only 86 pounds.

5.1.1 Glass fabrication

Two 50 mm thick glass blanks were created for this mirror. The first shell suffered from flaws present since the initial casting, and this caused it to fail during the polishing process. [6] The second shell was successfully cast using the large rotating oven at the Steward Observatory Mirror Lab, Figure 5.2. The mirror was cast from a single chunk of Ohara's E6 borosilicate glass.[1] This particular casting achieved excellent homogeneity because a single block of E6 was used to cast the entire mirror blank. (This block was hand-selected in Japan specifically for this project.) The final mirror blank was 50 mm thick and 2.2 m in diameter.

The glass fabrication process is shown in Figure 5.3. The generating and polishing operations were designed such that no novel tooling was needed for these steps: the opticians used the existing generating and polishing machines to fabricate the thin membrane. The process started with generating, grinding, and polishing the convex

[1]Why E6? There were several reasons. First, borosilicate possesses a relatively low thermal coefficient of expansion (Section 2.2), which means that it doesn't change dimension much with changes in temperature. For example, the CTE of E6 is 2.9 parts/°C, while standard optical glass (BK7) is about 7 parts/°C. The Mirror Lab also has a legacy with this glass: the opticians have been using it long enough such that they are comfortable working with it, and they understand its behavior through years of use.

1. The mold is assembled.

2. A single chunk of E6 is lifted out of its shipping container.

3. The glass is lowered on the form inside the 8-m rotating furnace.

FIGURE 5.2. The two meter casting process. These three images show how the Steward Mirror Lab's 8.5 m furnace was prepared for the casting of the 2 m glass blank. 1. A 2.2 m mold was assembled in the oven's center. 2. The glass was lifted out of its shipping container and inspected for impurities. 3. The block was lowered on to the mold. The Steward furnace was then fired to a temperature of 1100 °C (2000 °F). At this temperature, glass has the consistency of thick honey, and it flowed into the mold. The furnace was slowly cooled, and the finished glass blank was removed from the mold. Throughout the casting process, the furnace rotates such that the top of the glass blank forms a parabola.

(non-optical) side of the mirror blank. After this step, the blank was about 35 mm thick, and it was flipped over and blocked down to a thick, rigid blocking body using pitch.[2] At this point, most of the excess glass was removed from the concave (optical) side until the shell was 3 mm thick. Finally, the glass was ground and polished using conventional techniques. The completed membrane was 2 mm thick. After polishing, the 2.2 m round shell was cut into a 2 m hexagon (point-to-point).

The glass shell was complete after the polishing operations, but it still remained attached to the blocking body. In the past, the standard procedure for smaller mirrors involved placing the mirror in a 200 °C oven, waiting for the pitch to soften, and slowly sliding the glass off the blocking body. Because of its large size, this procedure would have posed too much of a risk to the glass. Instead, a new procedure for deblocking a glass membrane was developed.

[2]The blocking body is needed to support the membrane throughout the fabrication process such that it does not bend or flex during the polishing operations. In this case, the blocking body was made of E6 glass.

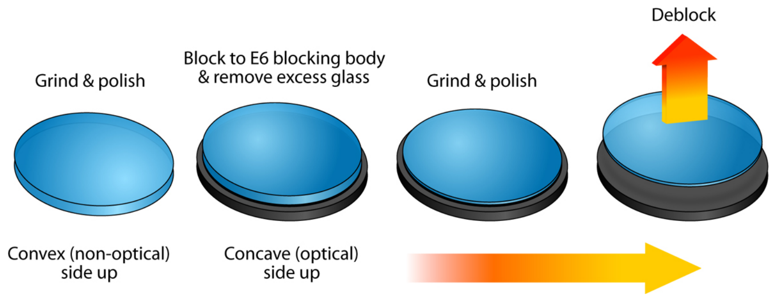

FIGURE 5.3. The glass fabrication process. The process started with a meniscus-shaped glass blank, Figure 5.2. The convex, non-optical surface was polished while the blank was 50 mm thick. This allowed the opticians to use standard polishing techniques and their existing tooling. After the convex (non-optical) surface was finished, it was flipped over and bonded to an E6 blocking body using pitch. After attachment, the excess glass was removed from the concave (optical) side using a diamond cutting tool. Finally, the concave side was ground and polished to remove any micro-fractures. When the optical finishing was complete, the facesheet was removed from the E6 body. The unique deblocking process developed for this mirror is described in Section 5.1.2.

5.1.2 A novel scheme for deblocking a 2 m mirror

Brian Cuerden's[3] scheme for deblocking the glass is illustrated in Figure 5.4. The membrane was placed in a hot bath of motor oil, and the bouyant forces were used to separate the glass from the blocking body once the pitch softened. To assist in this operation, eighteen cylindrical floats were attached to the glass using an RTV adhesive. The entire assembly was placed in a 10-foot wide insulated steel tank containing standard motor oil, and the oil was heated to 120 °C (250 °F). Distance gauges were used to monitor the glass as it started to separate from the blocking body. The entire operation took 30 hours total: the motor oil required 12 hours to preheat; the glass lifted off in 6 hours; and the oil needed another 12 hours to return to room temperature.

Once the glass was cool, it was removed from the oil bath using an 18-point whiffle

[3]Brian is a mechanical engineer at Steward Observatory with years of experience working with large telescope optics.

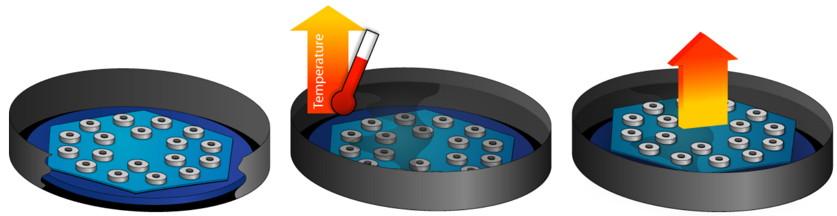

FIGURE 5.4. Cuerden's deblocking scheme. Left: Floats were attached to the mirror's surface, and the entire assembly was placed in a large insulated tank. Middle: The tank was filled with motor oil and heated to 120 °C (250 °F). Right: After several hours, the pitch released the glass from the blocking body, and it floated to the surface. Pictures of the deblocking process are shown in Figure 5.5.

tree. The glass was cleaned using a spray degreaser, and the floats were carefully removed. A convex vacuum tool was used to transport the membrane about the optics shop. Figure 5.5 shows photos taken at each step in the deblocking process.

5.1.3 Loadspreader design and attachment

After the glass was deblocked, the engineering team attached 127 nine-point loadspreaders to the rear of the facesheet. A schematic of a loadspreader is shown in Figure 5.6. Each loadspreader interfaced with a set of nine glass buttons that were permanently attached to the back of the facesheet using a cryo-ready adhesive. Two preloads maintained a stiff connection between the actuator and the glass buttons.[4] The preloads broke away when the forces became too great. For example, the spring next to the glass button breaks away when the actuator pulls down with too much force. The preload in-between the main and sub-loadspreader arms breaks away when the actuator pushes with too much force. Thus, there is a small range of force over which the actuator is coupled to the glass via a stiff connection. If the force exerted upon the glass is outside of this range, the loadspreader is completely ineffective.

[4] A preload is a spring that holds two things together. In this case, the preloads were dome-shaped washers made out of Teflon or steel.

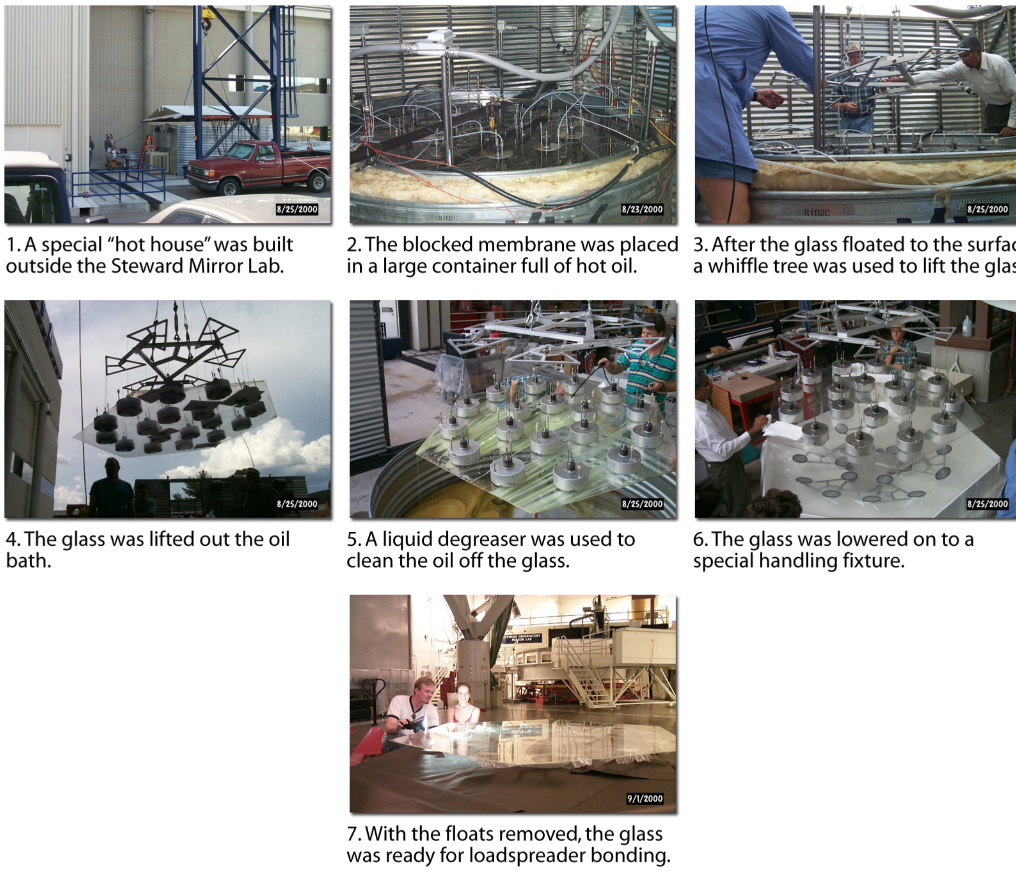

FIGURE 5.5. Photos of the deblocking process. 1. A special enclosure was built outside the Steward Mirror Lab. The resulting structure had a removable lid such that the glass could be taken in and out. 2. The blocked membrane was placed in a large tub of hot motor oil. Floats were attached to the glass to provide the buoyancy necessary to separate the glass from the blocking body. 3. Once the pitch melted, the glass floated to the surface, and a whiffle tree was used to lift the glass out of the oil. 4. The glass was lifted out of the oil using an overhead crane. 5. A liquid degreaser was used as an initial measure for cleaning the glass. 6. The glass was lowered on to a special handling fixture. Once secure on the fixture, the floats were removed and the glass was thoroughly cleaned. 7. The resulting 2 m glass membrane.

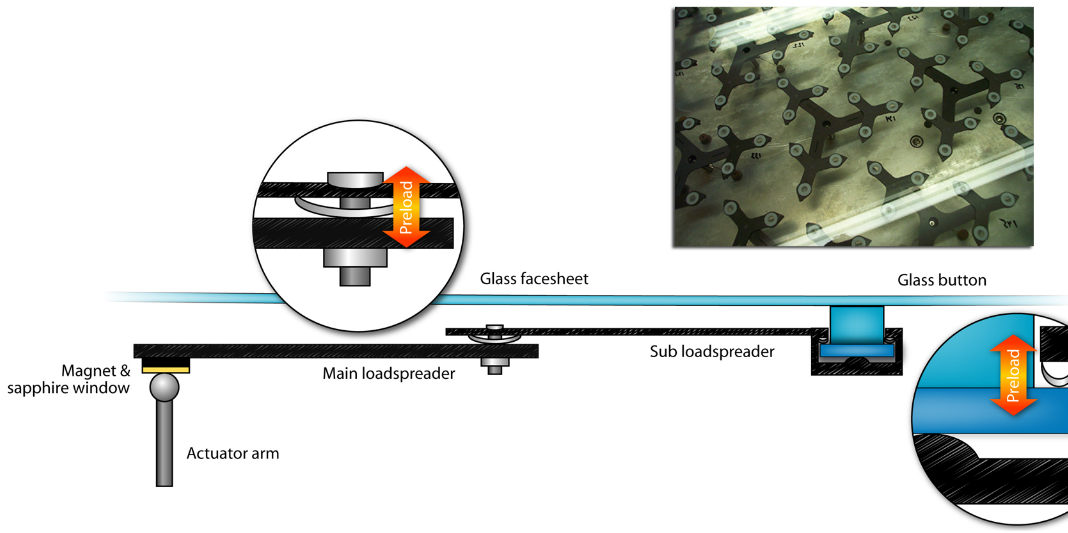

FIGURE 5.6. Schematic and photo of the NMSD loadspreaders. The drawing shows a side view of the loadspreader components. There are two preload systems which maintain a stiff connection between the glass and the actuator. The picture of the installed loadspreaders was taken before the glass was coated.

The loadspreaders served several purposes. First, they increased the spatial influence of each actuator. As a result, the actuator influence functions were roughly Gaussian instead of being a sharp peak immediately above the actuator. This reduces the number of required actuators necessary to maintain the same surface accuracy. The loadspreaders also served to protect the glass: if the force on each loadspreader was too large or too small, the loadspreader disengaged, as mentioned above.

5.1.4 Support structure and actuators

The support structure is a lightweight carbon-fiber structure, and it was designed at the Univ. of Arizona and fabricated at Composite Optics, Inc. Because it was constructed from a graphite composite, mechanical properties (such as thermal strain) were selected to maximize the on-orbit performance. The support structure is curved such that it has the same radius of curvature as the glass membrane. This allows the actuators to contact the loadspreaders in a direction that is normal to the membrane. The support structure includes a set of launch restraints that are used to firmly attach the glass to the membrane.

A schematic of an actuator used to adjust the mirror's surface is shown in Figure 5.7. The actuator's operation is similar to whipping a tablecloth out from beneath a set of dishes, Figure 5.8. Both depend on overcoming the static friction within the system. The schematic shown in Figure 5.7 illustrates the important components necessary for operation. There are two solenoids; one is used to turn the actuator clockwise and the other turns the actuator counterclockwise. When a current pulse is sent to a solenoid, a steel rod is accelerated through the solenoid and into a nut. At the moment of this impact, the nut slips about the screw by one arcminute. The flexures then return the nut to the original position, and the screw advances by one arcminute. Figure 5.9 is a picture of one of the NMSD actuators.

The actuators are "set and forget": no power is required to maintain their position. This is an important requirement because satellite platforms have limited power resources. In addition to this, no heat is emitted when they are not in use.

Once the mirror was assembled, the actuators were controlled remotely via a personal computer. The actuators were tethered to a large electronics chassis that gathered all of the actuator wires together. The chassis interfaced with two digital in/out boards installed in a PC. The user ran the actuators using a Windows program written specifically for this project.[5]

5.1.5 System integration

The completed mirror is shown in Figure 5.10. After the loadspreaders were attached, the glass was coated with bare aluminum. As is the case with all of Arizona's active mirrors, the glass membrane does not assume the correct shape when placed on

[5]The software was similar to that described in Section 6.3.2, but it didn't contain as many features.

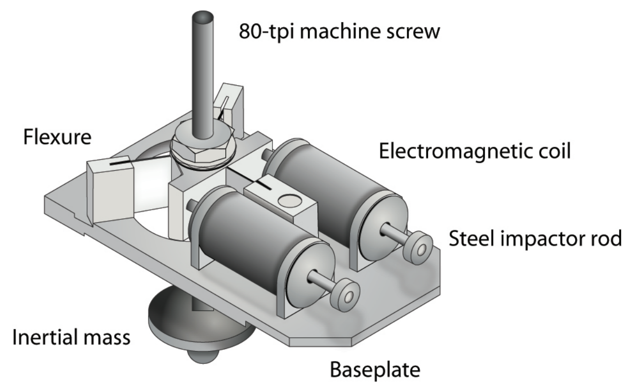

FIGURE 5.7. The University of Arizona set-and-forget actuator. The action is impact-driven, and it requires no power to maintain its position. It works using the tablecloth principle illustrated in Figure 5.8. There are two electromagnetic coils on either side of a nut. To move the actuator, a current pulse is sent to one of the coils. This accelerates a steel impactor rod through the coil until it taps on a nut. At the moment of impact, the nut slips about the screw by one arcminute. (This is equivalent to whipping the tablecloth out from beneath the dishes: the tablecloth moves, but the dishes don't.) Three flexures (arranged symmetrically about the nut) then slowly return the nut to its original orientation, and the screw advances by one arcminute. (This is equivalent to slowly pulling on the tablecloth: the tablecloth and dishes move together.)

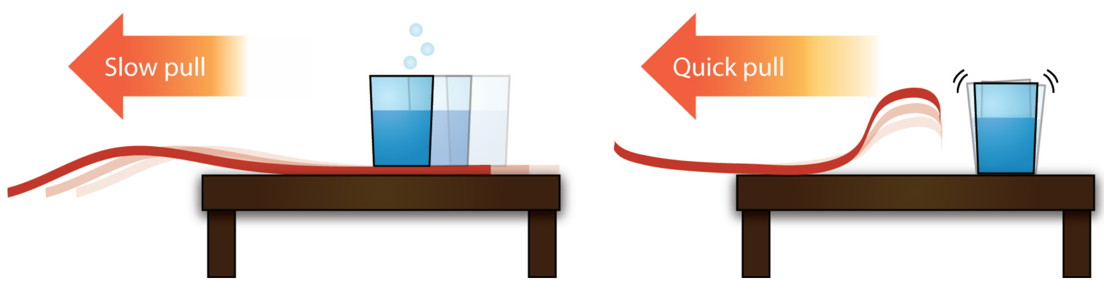

FIGURE 5.8. The old tablecloth trick. If the tablecloth is pulled to the left with a gentle pull, the glass will move in a one-to-one ratio along with it. (The force that accelerates the glass is less than the static friction between the glass and the tablecloth.) If the tablecloth is whipped to the left with a quick snap, the static friction is overcome and the tablecloth moves while the glass stays put. (The force that accelerates the glass is greater than the static friction.)

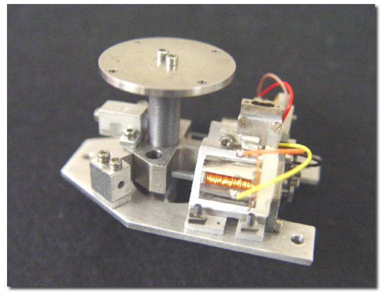

FIGURE 5.9. An NMSD actuator. All of the key components described in Figure 5.7 are visible in this picture: the electromagnetic coils (copper wire), the impactor rods, the inertial mass, the flexures, and the fine-pitch screw. Paul Gohman used a miniature computer-controlled milling machine to fabricate all of the parts.

the actuators.[6] As such, it was necessary to measure and adjust the mirror using the actuators. This was my role in this project, and the next section describes the techniques that I used to do this.

5.2 Metrology

Because the surface figure of the Arizona active mirror concept is determined by the array of actuators, the glass membrane does not assume the proper figure when it is initially assembled. The procedure for actuating smaller mirrors is simple: the membrane is supported on three actuators, and the mirror is illuminated with a point source at the center of curvature. The three initial actuators are adjusted until the image at the center of curvature displays three-fold symmetry. Additional actuators are applied and adjusted to achieve corresponding symmetry in the return image. Once all of the actuators are engaged, the figure is usually good enough for a visible

[6]The actuators can be positioned to the nearest 0.001” using standard measurement tools.

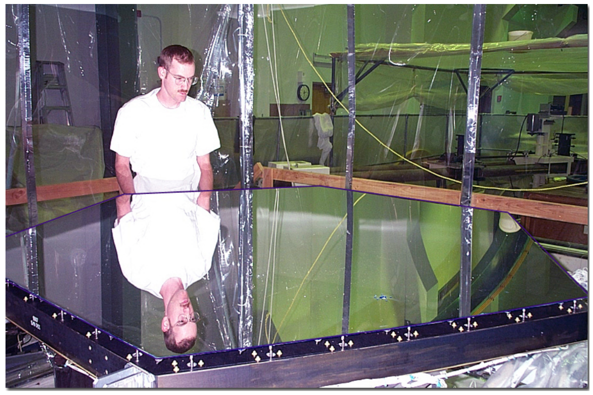

FIGURE 5.10. The completed 2 m NMSD mirror. Brian Stamper provides a sense of scale by standing next to the assembled mirror. The hole in the lower right portion of the glass was drilled out to prevent a fracture from propagating all the way to the edge.

interferometer, and interferometry[7] is used to remove the remaining figure errors.[8] However, because this mirror was larger than the previous Arizona mirrors, it was not possible to support the membrane by three points because the stress would risk fracturing the glass. In addition to this, the loadspreaders contained a mechanical system that decoupled the actuator from the glass if too much self-weight was loaded onto each support point. As a result, even if the glass had been able to withstand the stress of being supported by three points, the loadspreaders would not have worked correctly.

As a response to these concerns, I developed a metrology scheme that utilized three different tests. The first of these tests had a high dynamic range and low accuracy for doing rough mirror figuring. The two remaining tests were based on interferometry and had increasingly smaller dynamic ranges with better accuracy.

[7]The concept of interferometry is not discussed in this work. Basically, it is a technique which uses the wave-like properties of light to measure the shape of a surface. The basics of interferometry are discussed in Hecht's *Optics* [13], and the use of interferometry to measure surfaces can be found in Malacara's *Optical Shop Testing* [16].

[8]In fact, this is the technique that I used to correct the figure of the half-meter mirror that is discussed in Chapter 6.

5.2.1 Hartmann test

The concept of the Hartmann test is simple: a screen is used to project rays of light on to the test surface. The rays are imaged on to a CCD where they appear as spots. (An example Hartmann-gram is shown in Figure 5.13.) By noting the change in spot location as the actuators are adjusted, the user can determine the mirror's slope.

The Hartmann test that I designed and used differed from a conventional Hartmann test in several ways:

- The Hartmann mask (shown in Figure 5.11) was a paper mask with 216 holes that were 0.25" in diameter. Each actuator was surrounded by six spots arranged in a hexagonal layout. This geometry was useful because the size of the hexagon's image would scale up or down as the actuator moved up or down. An example of this is shown in Figure 5.14.

- The mask was placed directly on the mirror's surface. (The weight of the mask caused a small amount of deflection, but this deflection was insignificant compared to errors caused by incorrect actuator heights.) A cartoon of this concept is shown in Figure 5.11.

- The imaging system was designed such that the mirror surface and CCD were conjugate to one another. This layout (shown in Figure 5.12) allowed for a large dynamic range, which was the biggest advantage for using this test. The operation details are described below.

The geometry of the Hartmann testing scheme is shown in Figure 5.12. The mirror had a radius of curvature of 20 meters (65.6'), and the setup was assembled in the Optical Science Center's tower. A Princeton Instruments VersArray CT:1300B imaging array was positioned behind the center of curvature, and the CCD was on a stage such that they could be moved along the optical axis. The CCD had 1340

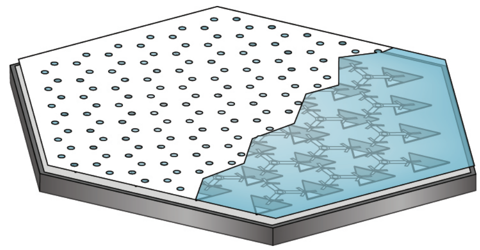

FIGURE 5.11. The Hartmann mask. I constructed the mask out of a large sheet of butcher paper. Each actuator location is surrounded by six holes arranged in a hexagon. There were 216 holes (I did not use this scheme to measure the single actuators at the very edge of the mirror), and each hole was 0.25" in diameter.

by 1300 imaging pixels, and each pixel was 20 microns square. There was a 100% fill factor, and the imaging area was 26.8 by 26 mm.[9] The HeNe laser source is not shown in Figure 5.12, but it was positioned next to the CCD. I designed the illumination system such that the aberrations due to the projection optics were small compared to the mirror's aberrations. The fold mirror was supported by a mount that was controlled via two Picomotors. This allowed for fine adjustment of the mirror's tip and tilt. The Hartmann mask was placed directly on top of the mirror, as shown in Figure 5.11.

After mirror assembly, this test proved to be an efficient, qualitative measurement tool for quickly identifying and correcting actuators that were severely out of place.[10] For example, Figure 5.13 shows two pictures that represent the before and after Hartmanngrams for the portion of the mirror that contains the central 19 actuators. The left side of Figure 5.13 shows that the Hartmann spots are visible, but they are not in the correct locations. The right side shows the results after the actuators in

[9]While the Hartmann mask was simple and inexpensive, a CCD of this size is not. Luckily, we were able to borrow it from another organization.

[10]I should mention that I tried a few other schemes before I settled on a Hartmann test, and none of them were very successful. First, I tried analyzing the return images to determine which parts of the mirror had the most error. I also tried using a formal curvature sensing technique with an instrument that was available in-house. Unfortunately, neither of these ideas was successful. The return image contained too many folds for either technique to be successful.

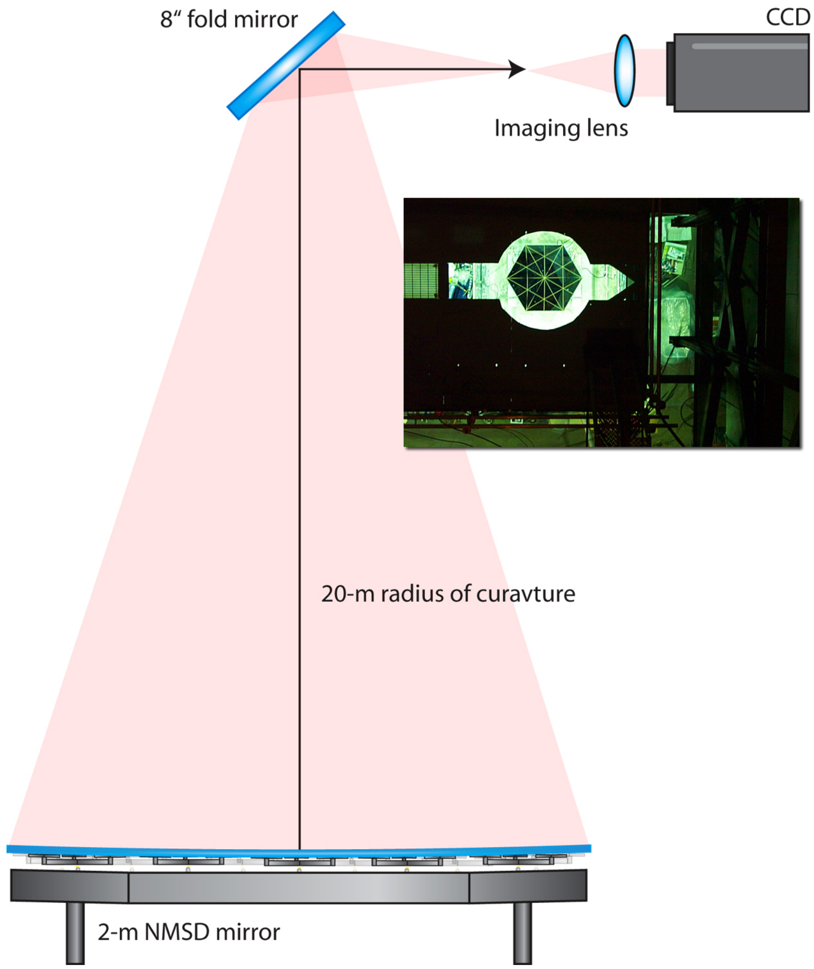

FIGURE 5.12. Hartmann test layout. The mirror had a large radius of curvature, so I tested it in the Optical Science Center's test tower. (The mirror was mounted at the tower's base, and the fold mirror, CCD, and illumination system rested on a platform 65 feet above the mirror.) The illumination system is not shown here, but the HeNe laser source would be behind the CCD. The illumination system used two singlets to shape the beam and control spherical aberration. (The resulting aberration from the illumination system was significantly smaller than the errors in the mirror.) The fold mirror was mounted on a tip-tilt stage, and the Hartmann mask rested directly on the mirror's surface. Inset: the view looking down from the platform where the laser and CCD were located. (There is an image of the camera and my hands inside the mirror.) The lines across the mirror are pieces of thin butcher paper that I was using as fiduciary markers.

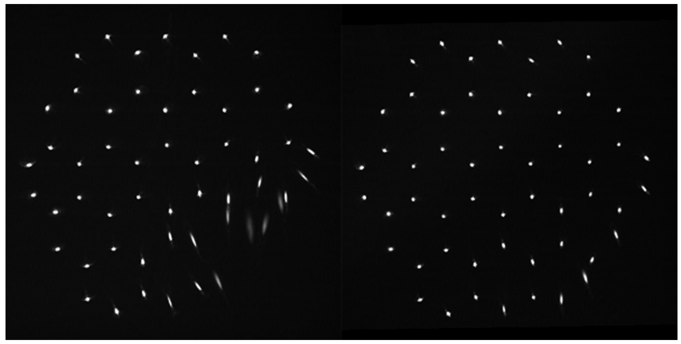

FIGURE 5.13. The Hartmann test as an efficient quantitative tool. These images show the Hartmann spots for the 19 inner-most actuators. There is an actuator inside each of the hexagons. Left: the actuators in the southeast corner are not adjusted properly. The Hartmann spots are in the image, but they are not in the correct locations. Right: the surface showed improvement after I adjusted the actuators. (The spots are still a little displaced; this is caused by the actuators surrounding the inner 19 actuators.)

the southeast corner were all moved up by hand. Using this information, I was able to manually turn each actuator while watching the resulting spot motions in real time. This proved to be a very effective procedure for quickly moving all of the actuators to their nominal positions.

I was also able to use this scheme to determine the relative actuator heights. Because the Hartmann spots form a hexagon around each actuator, the relative size of the hexagons provide the relative height information. For example, if a particular actuator is too low, the local surface above that actuator will be slightly more concave than the surrounding region. This region will have a shorter focal length, and the hexagon will be smaller.[11] If an actuator is too high, the surface above the actuator will be less concave than the surrounding region. This results in a larger hexagonal image. An example of this concept is illustrated in Figure 5.14.

[11]The connection between concavity and hexagon size depends on the location of the CCD. If the CCD is in front of nominal focus, a smaller hexagon indicates the region is more concave than the surrounding area, and the actuator is too low. If the CCD is behind nominal focus, a smaller hexagon indicates the region is less concave, and the actuator is too high.

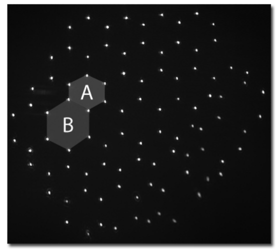

FIGURE 5.14. The Hartmann test was used to determine relative actuator heights. The hexagon that surrounds actuator A is smaller than hexagon B. Given this particular optical configuration, the actuator under the letter A is lower than the actuator under the letter B. (This image was taken in front of nominal focus.)

The Hartmann test also provided quantitative surface measurements. By moving the CCD back away from nominal focus, I was able to measure every ray bundle at two points. This technique is described in Figure 5.15. Using this information, I calculated the slope of the ray bundle and the slope of the mirror at each Hartmann aperture. To adjust the mirror, I used a least squares solution to calculate all of the actuator commands at once. (The least squares solution for mirror control is described in Section 5.3.)

This test was particularly effective for this mirror because the dynamic range is variable. For example, the mirror contained a lot of surface error during the initial measurements. As a result, I could only defocus the CCD by a short distance. (If the CCD was moved back too far, the Hartmann spots would start to overlap and my centroiding algorithm wouldn't be able to locate all of the spots.) As the mirror improved, I was able to defocus the CCD by a larger amount and detect smaller errors in the mirror.

This quantitative test scheme proved very successful. Figure 5.16 shows the initial and final quantitative measurements that I made using the Hartmann test. The mirror's initial figure was approximately 25 microns RMS, and the final figure was less than 4 microns RMS. This simple Hartmann test was able to improve the mirror's

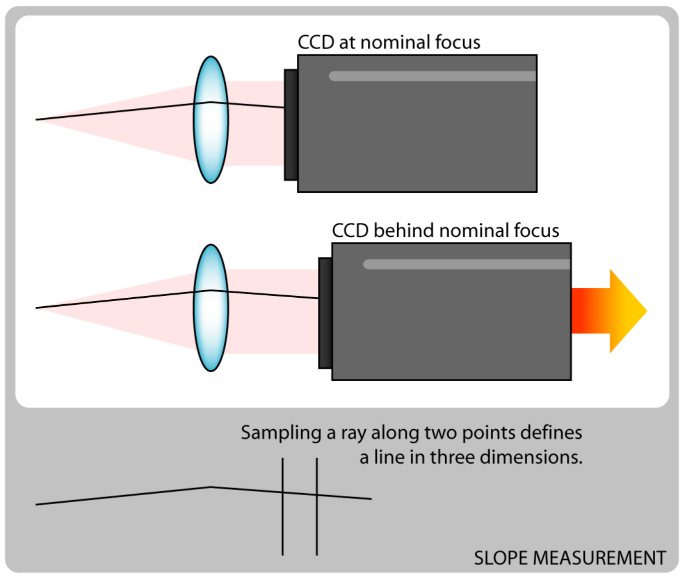

FIGURE 5.15. The hardware setup that allowed for quantitative Hartmann measurements. (This figure shows the illumination/imaging system shown in Figure 5.12.) Each Hartmann aperture produced a small bundle of rays. As an example, this figure shows one bundle of rays from one Hartmann aperture. I needed two images to calculate a quantitative surface figure. First, I took an image of the Hartmann spots when the CCD was at nominal focus. Next, I moved the CCD back away from focus and took another image. Using these two images, I was able to calculate the slopes of every ray bundle and the slope of the mirror at each Hartmann aperture.

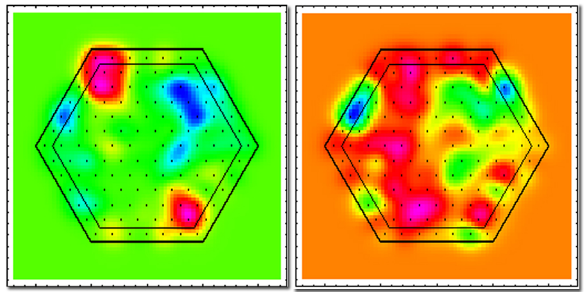

Figure 5.16. Initial and final Hartmann qualitative measurements. The surface on the left represents a surface figure of 25 microns RMS and 125 microns PV. The surface on the right represents a figure of 3.7 microns RMS and 23.1 microns PV. The final surface map is six times better than the initial measurement.

surface figure by a factor of six!

The Hartmann scheme was useful in two ways. I was able to efficiently position each actuator to within 3 to 5 microns of its ideal location. Once all of the actuators were positioned using this scheme, I was able to make quantitative measurements of the surface figure.

5.2.2 IR interferometry

The Hartmann test worked well enough to prepare the surface for infrared (IR) interferometry. The IR interferometer was based on a model initially developed in the late 1970's. The illumination source is a 10 W CO_2 laser operating at 10.6 microns. This interferometer was phase-shifted and connected to a computer running IntelliWave.[12]

Using the IR interferometer was more straightforward than the Hartmann test because the instrument was provided as a turnkey system. The initial interferogram is shown in Figure 5.17. Because the instrument was phase-shifted, I was able to generate surface maps and calculate an appropriate set of actuator commands to fix

[12]IntelliWave is a third-party software package that is designed to gather interferograms and calculate phase maps from a phase-shifting interferometer. Basically, IntelliWave collects four frames of interferograms, and it calculates a surface map from this information.

FIGURE 5.17. The initial infrared interferogram.

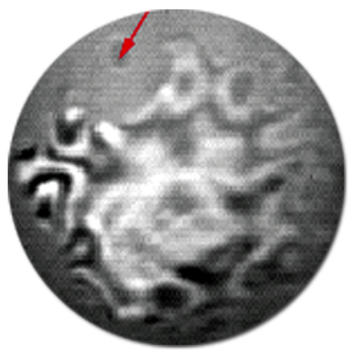

FIGURE 5.18. The final infrared interferogram. The surface statistics are 1.88 microns RMS and 15.9 microns PV. The arrow represents a region of high slope, and it was not collected by the interferometer's aperture.

the figure. The final interferogram taken using the IR interferometer is shown in Figure 5.18. The final surface statistics for this data are 1.88 microns RMS and 15.9 microns PV. This surface represents a clear aperture that is 90% of the total mirror width.

I wasn't able to measure the entire clear aperture using this instrument because the slopes near the edge of the mirror were too large. An example of this is shown under the arrow in Figure 5.18. In Section 5.2.5, I discuss some improvements to the metrology setup that would have allowed for the correction of these regions with high slopes.

I didn't spend much time using this instrument because working with it was difficult. The 10 W invisible laser necessitated a lot of precautions.[13] The laser, itself, was water cooled, and there was a very narrow window of operating conditions over which the device would actually lase. The detector system was an old, infrared Vidicon camera. I spent more time fixing the instrument than I did actually using it. As a result, I used it to quickly improve the mirror, and then I started using visible interferometry.

5.2.3 Visible interferometry

The visible interferometer was a PhaseCam on loan from 4D Technology. The PhaseCam is a modified Twyman-Green interferometer. It uses a diffraction grating to image four frames of data on to a single CCD. These four frames are phased 90 degrees apart from each other. As a result, a surface map is calculated from a single CCD frame. This system virtually eliminates the effects of vibration from the metrology setup. This interferometer was connected to a computer, and IntelliWave was used to generate the surface maps.

The PhaseCam proved to be very effective at measuring the mirror because its instantaneous measurement scheme was particularly good at gathering data over regions with high slope errors.[14] The initial and final surface maps are shown in Figure 5.19. The initial measurement on the left represents 2.0 waves RMS and 14 waves PV (HeNe). The final measurement on the right represents 0.7 waves waves RMS and 4.8 waves PV (HeNe).

[13] A 10 Watt CO_2 laser will easily burn holes in paper.

[14] The fringe visibility in high-slope regions declines more rapidly (than low-slope regions) when vibration is present. By collecting all four interferograms at once, the PhaseCam isn't vibration-sensitive. This allows for better fringe visibility in the high-slope regions.

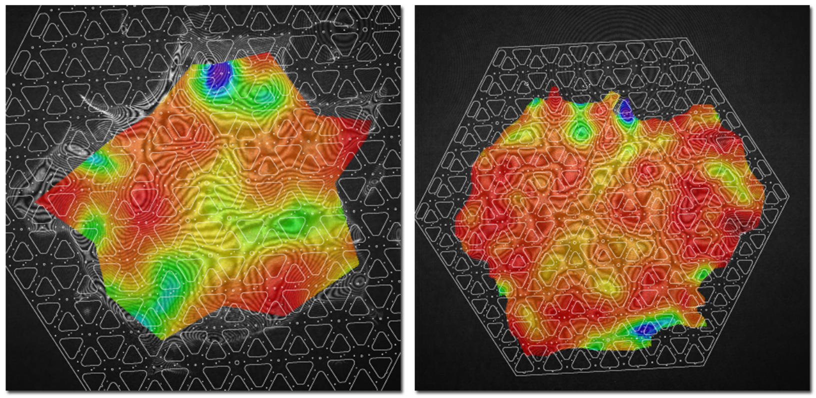

FIGURE 5.19. The initial and final measurements taken with the PhaseCam. The initial measurement on the left represents 2.0 waves RMS and 14 waves PV (HeNe). The final measurement on the right represents 0.7 waves waves RMS and 4.8 waves PV (HeNe). The regions near the edge contains slopes that are too high to be measured by the interferometer.

5.2.4 Summary of technical achievements

While this mirror didn't achieve its goal of diffraction limited performance (in the visible) across the entire aperture, this project is still considered a major success by the University. The NMSD mirror contributed the following technical achievements to Arizona's lightweight mirror program:

- The Steward Mirror Lab proved that a 2 m thin glass membrane can be made using conventional fabrication tools.
- The engineering team pioneered a novel technique for deblocking a thin glass membrane from a blocking body.
- I developed a test plan designed to measure the mirror both in its initial, inaccurate state and as the mirror approaches the diffraction limit. This scheme could be used to measure future high authority mirrors in an efficient manner.
- Both the actuators and the loadspreaders were created specifically for this

project, and they represent an excellent first-generation design.

5.2.5 Suggested improvements and lessons learned

While this mirror did not accomplish the ultimate goal of diffraction-limited performance across the entire two meter aperture at visible wavelengths, it has provided a wealth of information about designing, fabricating, and operating lightweight active mirrors. This section outlines some of the most important lessons learned during the metrology phase of the project. Future mirror designers should take these points into consideration before beginning to work on the next generation of active mirrors.

Suggested hardware improvements:

- *Mount the mirror on its own, isolated platform when testing/actuating.* During the optical testing, the mirror and the cleanroom floor shared the same foundation. When someone stepped into the cleanroom, they distorted the mirror because it was directly coupled to the floor.

  During initial actuation, it's essential that the metrology engineer have real-time feedback from the mirror. (Even though the mirror was remotely-controlled, it's important that the engineer be able to watch or touch the actuators or the glass while the mirror is under test.) There are two instances where real-time feedback is helpful:

  1. Because the NMSD used prototype actuators, there was never a guarantee that any actuator was moving in the direction that it was asked to move. It's always helpful to watch the actuators as they move to confirm that they are moving in the proper direction. Given the hardware configuration, the actuators could not be monitored while the mirror was being measured.

2. It's always helpful to walk up to the mirror, gently push down on the facesheet, and observe the results. This test is especially useful if the slopes in one region are so high that the return rays miss the metrology aperture. For example, if a particular region contains so much error that the interferometer cannot measure it, the metrology engineer can gently push or pull on the mirror until she sees interference fringes in that region. (This test will indicate whether the region is too high or too low.) This scheme allows for very efficient actuation of the worst portions of the mirror. Had I been able to perform this test, I would have been able to adjust the actuators such that the entire mirror was visible in Figure 5.19.

The mirror's mounting situation did not allow for either of these real-time tests: progress was severely hindered because I could not touch or watch the actuators and measure the mirror at the same time. If the mirror was mounted on a separate foundation, someone could stand next to the mirror while it was being measured and actuated.

- *Design the actuator control software with both 'large step' and 'normal step' modes.* When the mirror was actuated for the first time, the actuators had to move large distances. Under normal conditions, the actuators were designed to move with a 15 nm step size. Some of the initial errors were as large as 200 microns; this is equal to 13300 steps! It took roughly 50 minutes to move an actuator this far using its normal settings (15 nm step size). If the software could automatically double or triple the current and pulse width settings that are sent to each actuator, this initial process could have taken place much more quickly. Alternatively, the *actuators* could be designed to have large step and small step modes.

- *Include a linear distance encoder on each actuator.* The success of the MARS design depends on repeatable, accurate actuator behavior. The NMSD actuators were neither repeatable or accurate. It would have been incredibly valuable to know how far each actuator actually moved. Although this would represent a large increase in the initial cost of each actuator, the time saved during the testing and actuation process would more than make up for it. Instead, I spent a good deal of time trying to figure out how far the actuators had moved. This is particularly important with the Hartmann and IR interferometric tests because these tests do not have the sensitivity to measure the smallest actuator motions.

Successful techniques:

- *The Hartmann test proved to be an efficient method for quick, initial actuation of the mirror.* The Hartmann test is an effective tool for high authority mirrors. By watching the set of six spots surrounding each actuator, each actuator can be manually turned until the spots form a uniform hexagon around the actuator. This procedure proved to be a quick and efficient method for moving all of the actuators to their nominal positions. The mask was constructed out of paper and all of the imaging lenses were simple, plano-convex lenses. The only disadvantage to using this system is that a CCD with a large collecting area (i.e.: 1 in^2) is preferred. This method would have been particularly effective if the mirror was not mechanically coupled to the cleanroom floor.

- *A system that compensates for inconsistent actuator behavior must be included in the algorithm that corrects the mirror's surface.* No two actuators are the same. At some resolution, inconsistent actuator behavior is going to be the limiting factor in improving the mirror's surface.[15] This problem can be circumvented by using actuator encoders. Alternatively, the actuator behavior

[15] Our inability to measure the high-slope regions was always the limiting factor.

can be analyzed in software. While the NMSD actuators definitely behaved inconsistently, they were never the limiting factor in the mirror's progress. Thus, I never implemented a permanent scheme for monitoring actuator behavior.

- *The PhaseCam proved to be a useful tool for testing the mirror under visible interferometry.* The PhaseCam easily measured the mirror's high slopes under very difficult mechanical conditions. This instrument should be considered for future applications where vibrations and large surface errors would confuse conventional interferometers.

The most important lesson of all: the effects of scaling:

- ***Scaling a half-meter mirror up to a two-meter model is not as easy as it sounds on paper.*** This becomes an issue even before the mirror blank is created. Most glass manufacturers have half-meter blanks on hand, but finding a high quality piece of homogenous, low CTE optical glass is a serious challenge. As described in Section 5.1.4, Steward elected to cast the blank themselves.[16] After the blank is created, the glass faces challenges in polishing, handling, and deblocking.

- *Mirror handling becomes a major engineering challenge with apertures greater than one-meter.* The simple act of moving a two meter thin glass shell around the optics shop requires a separate team of mechanical engineers devoted to the task. Unlike a smaller (0.5-m) mirror, the mirror blank cannot be lifted by hand and carried around the shop. For this project, Steward Observatory had to design special tooling and procedures for moving the blank around the shop as it progressed through the figuring process. In addition, Brian Cuerden developed an entirely new method for deblocking a 2 m membrane.

[16] I should note that Steward is one of the few shops in the world that is capable of casting their own 2 m glass blank.

5.3 The least squares algorithm for high authority mirrors

5.3.1 When and why is LS useful?

In Chapters 5 and 6, I mention that I use a least-squares (LS) algorithm to generate entire lists of actuator commands at once. While there is plenty of literature that discusses the fundamentals of least-squares theory, there is not an article dedicated to its use for active mirrors. The concepts are not difficult, and I certainly didn't invent *any* of this. However, I used this scheme *six* times across four projects and over six years during my graduate residency. Clearly, it's a useful tool.

When I first encountered this scheme, I spent several weeks working out the exact details.[17] If I had been presented with a cookbook-type approach, I could have solved the problem in a manner of minutes. Therefore, I hope that future mirror control engineers will find this section useful: I provide a recipe-like approach for using a least-squares algorithm to generate actuator commands from an existing surface map.

5.3.2 The mirror control problem

The mirror control problem is easily understood: provided that the user can measure the mirror surface, what combinations of actuator commands should be used to fix the mirror surface? How far (and in what direction) should each actuator move to remove all of the bumps and valleys?

Before a solution can be obtained, the least-squares algorithm requires a few pieces of information from the user. First, it must know the current state of the system. This is usually input as the current surface map. The algorithm also has to know how the actuators are capable of changing the mirror's surface. Each actuator is characterized by an "influence function", or a function that states how the actuator

[17] As with any problem, it's easy to say "Oh, I used algorithm X to solve the problem." The time-consuming part is figuring out how to actually *use* the algorithm on a computer or even a pad of paper.

will affect the surface when it's moved. Finally, the algorithm needs to know the desired final state. In the case of a mirror, it is assumed to be a perfect surface (no bumps and no valleys).

The least-squares approach may be used to solve this problem provided that the mirror is thought of as linear system. A system is linear if it obeys the linear principle of superposition: the "overall response to a linear combination of stimuli is simply the same linear combination of the individual responses."[10] In the case of an active mirror, this means that the surface map can be produced by a linear combination of the individual influence functions.

The least-squares approach is appealing for several reasons. First, the influence functions (the actuator models) don't have to be perfect because the algorithm can be used iteratively to solve the control problem. For example, if the actuator behavior isn't modeled perfectly, then the first set of actuator commands will not result in a perfect mirror. However, the mirror surface will improve as long as the actuator model is at least a good estimate. The algorithm can then be used a second time to improve the mirror a little more. In addition, as the mirror is improved, the actuator model can be updated, and this will result in more accurate results from the algorithm.

5.3.3 LS solution by way of an example

Consider a square mirror that is supported by four actuators; one actuator is in the center of each of the four quadrants. The mirror control engineer measures the mirror and generates the surface map shown in Figure 5.20. By inspection, it appears that the upper left actuator is correctly placed, the upper right and lower left actuators

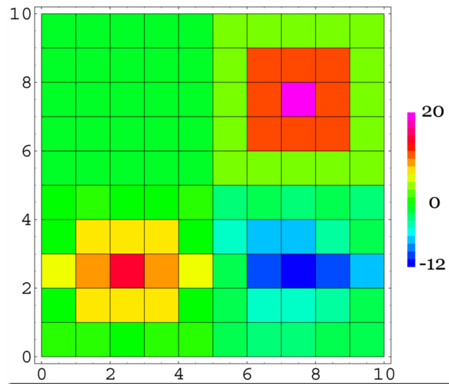

FIGURE 5.20. The initial surface map. This example considers a square mirror that is supported by four actuators. One actuator is in the middle of each quadrant. The actuator in the upper left is probably at the correct height. (There is no disturbance in this quadrant.) The actuators in the upper right and lower left are too high, and the actuator in the lower right is too low.

are too high, and the lower right actuator is too low.[18] The control engineer could certainly move the resulting actuators in the correct direction, but this operation may take a lot of time if several hundred actuators are involved. Instead, the engineer opts to use a LS approach to generate a list of actuator commands.

First, the engineer must generate an influence function for each of the four actuators. An influence function describes how the mirror surface changes as the actuator is moved. There are two ways to do this:

1. The engineer could use real data. For example, an actuator could be advanced

[18]In Figure 5.20, the surface map is represented graphically, but it is really just a 10 x 10 matrix:

$$\begin{bmatrix} 0 & 0 & 0 & 0 & 0 & 4 & 4 & 4 & 4 & 4 \\ 0 & 0 & 0 & 0 & 0 & 4 & 12 & 12 & 12 & 4 \\ 0 & 0 & 0 & 0 & 0 & 4 & 12 & 20 & 12 & 4 \\ 0 & 0 & 0 & 0 & 0 & 4 & 12 & 12 & 12 & 4 \\ 0 & 0 & 0 & 0 & 0 & 4 & 4 & 4 & 4 & 4 \\ 2 & 2 & 1 & 2 & 2 & -1 & -2 & -2 & -1 & -1 \\ 1 & 8 & 8 & 8 & 1 & -1 & -4 & -4 & -3 & -1 \\ 7 & 10 & 15 & 10 & 7 & -1 & -10 & -12 & -10 & -7 \\ 1 & 8 & 8 & 8 & 1 & -4 & -7 & -7 & -3 & -1 \\ 1 & 2 & 1 & 1 & 2 & -2 & -1 & -2 & -1 & -2 \end{bmatrix}.$$

by 10 steps (or 10 nm, 10 microns, etc). If the engineer took a surface measurement before and after the actuator was moved, she could generate a surface map that showed the net effect of having moved the actuator. This is the influence function for that actuator, and this could be repeated for all of the actuators. Note that this approach assumes that the surface deflects linearly with actuator displacement.

2. The engineer could use a model. For example, she could model the net effect as a Gaussian with a particular height and width. If available, a mechanical engineer can generate a very accurate model using finite element analysis.

I have used both of the schemes described above, and I have found success with both methods. In general, actual data yields the best results. However, it can be time-consuming to collect an influence function for every actuator. Alternatively, one set of actual data can be collected and then linearly shifted to represent the remaining actuators.

For this example, the control engineer decides to model the actuators as three-dimensional ziggurat functions.[19] She decides to use a model because her actuators are well-behaved.[20] Figure 5.21 shows the resulting four influence functions that she generates.

While the influence functions shown in Figure 5.21 are displayed in a graphical form, they are really just matrices of numbers. For example, the matrix representing the influence function of the upper left actuator looks like this:

[19]A ziggurat (`zi-ger-RAT`) predates the (comparably) modern pyramids of Egypt. Constructed by the Mesopotamians, a ziggurat is a multi-layered temple where each ascending layer is smaller than the one below. Imagine a pyramid built from standard Legos; a ziggurat is the best one could hope for.

[20]A well-behaved set of actuators means that actuator A behaves identically to actuator B, as to C, etc. This would certainly be the case if a set of commerically-produced motors, like the New Focus Picomotors, are used. If the actuators are built in-house (to less exacting production standards) it would be best to take actual data for use as the influence functions.

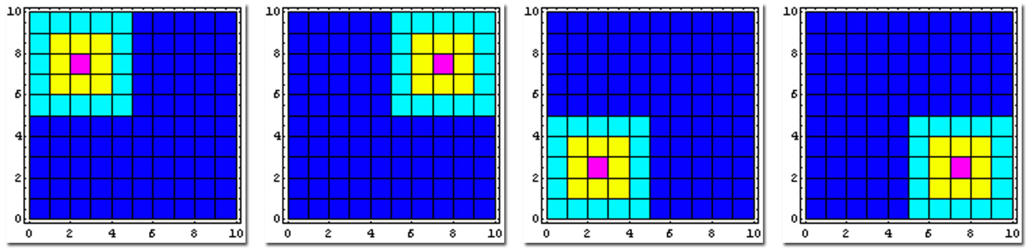

FIGURE 5.21. Four influence functions. The influence functions, from left to right, are labeled 1, 2, 3, and 4.

$$\begin{bmatrix} 1 & 1 & 1 & 1 & 1 & 0 & 0 & 0 & 0 & 0 \\ 1 & 3 & 3 & 3 & 1 & 0 & 0 & 0 & 0 & 0 \\ 1 & 3 & 5 & 3 & 1 & 0 & 0 & 0 & 0 & 0 \\ 1 & 3 & 3 & 3 & 1 & 0 & 0 & 0 & 0 & 0 \\ 1 & 1 & 1 & 1 & 1 & 0 & 0 & 0 & 0 & 0 \\ 0 & 0 & 0 & 0 & 0 & 0 & 0 & 0 & 0 & 0 \\ 0 & 0 & 0 & 0 & 0 & 0 & 0 & 0 & 0 & 0 \\ 0 & 0 & 0 & 0 & 0 & 0 & 0 & 0 & 0 & 0 \\ 0 & 0 & 0 & 0 & 0 & 0 & 0 & 0 & 0 & 0 \\ 0 & 0 & 0 & 0 & 0 & 0 & 0 & 0 & 0 & 0 \end{bmatrix}.$$

The remaining influence functions look similar, except their maxima are located in the appropriate quadrant.

Now that she has a surface map and influence functions, she has everything she needs to solve the problem. As discussed above, the least-squares solution is generally used to solve systems of simultaneous equations. This system is essentially no different: there are four unknowns (the actuator commands), and there are four knowns (influence functions). The equation that will yield the solution is as follows:

$$A \cdot b = \psi. \tag{5.1}$$

A represents a matrix containing the influence functions, b contains the actuator commands (the unknown in this equation), and ψ is a vector that represents the current surface figure. Here's another way to interpret Equation 5.1: "How many

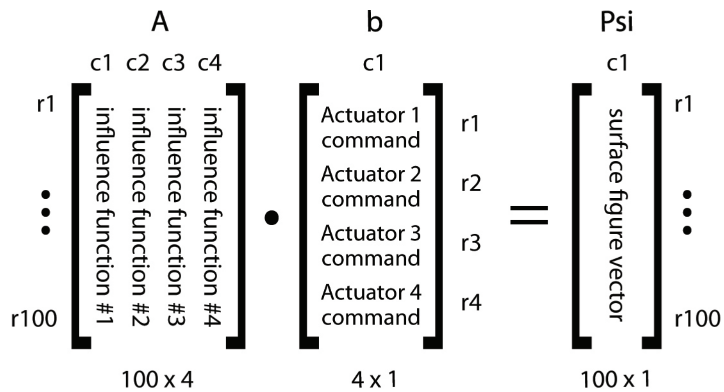

FIGURE 5.22. The least squares equation. Matrix A contains the influence functions, shown in Figure 5.21, and redimensioned such that each influence function is a vector containing 100 numbers. The influence functions are labeled according to the scheme described in Figure 5.21's caption. Vector b contains the actuator commands (the unknown), and vector ψ contains the surface map shown in Figure 5.20.

units of each influence function are needed to fit to the current surface map?"

Figure 5.22 provides a visual depiction of how the variables work in Equation 5.1. These variables are described in the following list:

- **A** is the influence function matrix. In this example, it has dimensions of 100 rows by 4 columns. There is one column for each influence function, and there are 100 rows because the influence functions and the surface figure all contain 100 pixels.[21] To prepare the influence functions for this matrix, they are converted from 10 x 10 matrices to 100 x 1 vectors. It doesn't matter how this redimensioning is done as long as the scheme remains consistent throughout the entire process.[22]

- **b** is the coefficients, or actuator commands. They are the unknown variables in

[21]The 100 pixels used in this example was chosen arbitrarily. In a real situation, this will usually be determined by the number of the pixels in the CCD that is used to gather the surface map.

[22]For example, the most common method takes the 10 rows of the matrix and strings them together as a long vector containing 100 numbers: $[a_{1,1}, a_{1,2}, a_{1,3}, a_{1,4}, a_{1,5}, a_{1,6}, a_{1,7}, a_{1,8}, a_{1,9}, a_{1,10}, a_{2,1}, a_{2,2}, ..., a_{10,10}]$. Practically speaking, Mathematica's `Flatten[]` command does this. In MatLab, if M is a 10 x 10 matrix, `N = reshape(M,100,1)` redimensions M and saves the result to N.

this equation. For this example, b has dimensions of 4 rows by 1 column.

- $\boldsymbol{\psi}$ is the surface map vector. For this example, it has dimensions of 100 rows by 1 column. Like the influence function matrix, it is redimensioned from a 10 x 10 matrix to a 100 x 1 vector. For this example, ψ is the redimensioned matrix shown in Figure 5.20.

Once everything is redimensioned into vectors and packed into the appropriate matrices, the solution can be obtained. Solving Equation 5.1 for b isn't as simple as it looks because A generally isn't invertible.[23] The following is the least squares solution for b:

$$\begin{aligned} A \cdot b &= \psi \\ A^{\mathrm{T}} \cdot A \cdot b &= A^{\mathrm{T}} \cdot \psi \\ \left[A^{\mathrm{T}} \cdot A\right]^{-1} \cdot A^{\mathrm{T}} \cdot A \cdot b &= \left[A^{\mathrm{T}} \cdot A\right]^{-1} \cdot A^{\mathrm{T}} \cdot \psi \\ b &= [A^{\mathrm{T}} \cdot A]^{-1} \cdot A^{\mathrm{T}} \cdot \psi. \end{aligned} \tag{5.2}$$

First, both sides of the equation are multiplied by the transpose of A. When matrix A is multiplied by its transpose A^{T}, the resulting matrix $[A^{\mathrm{T}} \cdot A]$ is square and invertible. Thus, in the final step, both sides are multiplied by the inverse of $[A^{\mathrm{T}} \cdot A]$. The result gives a 4 x 1 vector b: the solution that contains the actuator commands.[24]

When the control engineer uses Equation 5.2 to solve for b, the result is as follows:

$$b = \begin{bmatrix} 0 \\ 4 \\ 2.76991 \\ -2.0708 \end{bmatrix}. \tag{5.3}$$

[23] Invertible matrices must be square (n rows and n columns). In order for A to be square, the number of actuators must be equal to the number of pixels, and this generally doesn't happen.

[24] I should mention that MatLab provides an even easier way to solve this equation. The command $\boldsymbol{\psi} \setminus$ `A` will yield the solution b. Note the direction of the slash.

These are the actuator commands used *to obtain* the surface figure shown in Figure 5.20. In other words, 0 units of influence function number one + 4 units of influence function number two + 2.74991 units of influence function number three + −2.0708 units of influence function number four produces the best fit to the surface map shown in Figure 5.20. In order to use this result as actuator commands, they must be multiplied by negative one:

$$\begin{bmatrix} 0 \\ -4 \\ -2.76991 \\ 2.0708 \end{bmatrix}.$$

These commands will *remove* the errors from the surface.

Finally, even though all of the influence functions were positive bumps, the algorithm was able to accurately describe the negative dip in the mirror. This occurs because the entire system is assumed to be linear. As long as this holds true, the user doesn't have to worry about including positive and negative influence functions for each actuator.

5.3.4 A note about units

Throughout this description, I don't attach any physical units to any part of the problem. For example, what do the numbers in Equation 5.3 represent in the physical world? The solution contains the same units as the actuator functions and surface map. Therefore, if the units of these matrices were in microns, then the actuator in the upper right must be moved down four microns to fix the surface error.

When actuating the mirror for the first time, it's a good idea to move the actuators less than the prescribed amount. For example, the solution from the previous section suggests that the upper right actuator should be moved down four units in order to fix the surface error. Instead of moving that actuator four units, it would be best to move it by *half* this amount in two separate events. This suggestion may seem trivial for this example, but it will be important on a mirror with 200 actuators. If the actuators don't exhibit consistent behavior (and the engineer hasn't yet realized this fact), moving the actuators by a fraction of the prescribed amount will allow the engineer to monitor the actuator behavior without significant risk to the surface figure.

5.4 Chapter summary

This chapter summarizes the design and control of the Arizona NMSD mirror. The F/5 NMSD is 2 meters in diameter (point-to-point), and it uses a 2 mm thick borosilicate glass shell as the optical surface. The mirror has an areal density of 13 kg/m^2, including the glass, 166 actuators, 127 nine-point loadspreaders, the support structure, and all of the onboard wiring. The entire 2 m NMSD mirror weighs 86 pounds.

In this chapter, I reviewed the fabrication details, and then I described the metrology scheme that I developed for measuring this mirror. Here are the most important conclusions:

- The mirror was commissioned by NASA as part of a technology demonstration for the James Webb Space Telescope, the successor to the Hubble Space Telescope. The resulting mirror had an areal density of 13 kg/m^2. (The areal density of the Hubble's primary mirror is 180 kg/m^2.)

- The Steward Mirror Lab developed a novel technique for deblocking a 2 m thin glass shell from the blocking body. Brian Cuerden's scheme is discussed in Section 5.1.2.

- The mirror was adjusted to 0.7 waves RMS and 4.8 waves PV (HeNe) across 90% of the clear aperture. The final surface map is shown in Figure 5.19.

- I presented a list of lessons-learned throughout the fabrication and testing process. I will summarize them each with one sentence here, and they are discussed in detail in Section 5.2.5:

1. The mirror should be mounted on its own, isolated platform when testing and actuating.
2. The actuator control software (or the actuators) should be designed with both a ‘run’ and ‘walk’ mode.
3. Each actuator should have a linear distance encoder.
4. The Hartmann test proved to be an efficient method for quick, initial actuation of the mirror. It was also robust enough to provide qualitative measurements once the initial actuator positions were set.
5. A system that compensates for inconsistent actuator behavior must be included in the algorithm that corrects the mirror’s surface.
6. The PhaseCam proved to be a useful tool for testing the mirror under visible interferometry.
7. Mirror handling becomes a major engineering challenge at the two-meter scale.
8. **Scaling a half-meter mirror up to a two-meter model is not as easy as it sounds on paper.**

- Finally, I presented a useful guide to using a least-squares approach for solving the actuator control problem. None of this material is novel, but the fact that I’ve written it down as it pertains to active mirrors *is* new. The procedure, complete with an example, is described in Section 5.3.

Chapter 6

The half-meter ultralightweight demonstration mirror

In 1999, the University of Arizona was asked to build a prototype mirror that would achieve an areal density of 5 kg/m^2. The result, based on the 2 m mirror described in Chapter 5, was an ultralightweight half-meter mirror that is currently the lightest glass mirror in the world. This chapter begins by outlining the motivation for this project, and then I provide the details about component fabrication, metrology system, and mirror control.

6.1 Earth-imaging from geosynchronous orbit

Most contemporary Earth-imaging sensors are placed in a low-Earth orbit (LEO). LEO satellites are located anywhere from 320 - 800 kilometers (200 - 500 miles) above the Earth's surface. Because of their close proximity to the surface, they must maintain a high velocity in order to remain in orbit. This results in a very short period of revolution: the average LEO satellite takes about 90 minutes to complete one revolution around the Earth.

While the close proximity of these satellites can provide spectacular imaging capabilities, there are a few disadvantages. First, the satellites do not remain over a fixed ground location. This means that the organization that operates the sensor does not enjoy a continuous stream of data for a particular location. Also, it's relatively simple to calculate the orbits of all currently-operating sensors: most organizations are aware of when a particular satellite passes overhead, and they will govern their activities accordingly.

One advantage to using geosynchronous (geo) orbit is that it provides a continuous stream of data for a particular ground location. As a satellite is placed in orbit father away from the Earth, it experiences less of the Earth's gravity, and it doesn't have to travel as quickly to remain in that orbit. At one particular distance from the Earth, the satellite will orbit at the same angular speed as the Earth's rotation. This location is referred to as geosynchronous orbit, and a satellite in this orbit will always remain fixed over the same ground location.

Geo orbit is 35,793 km (22,241 miles) above the Earth, and this presents some interesting challenges for the person designing the optical sensors. First, this is 100 times farther away than a LEO satellite, so fewer satellites are necessary in order to image the entire planet. The disadvantage to this location is that a geosynchronous imaging system must have an aperture 100 times larger to achieve the same resolution as a low-Earth orbiting satellite. Even the lightweight NMSD mirror described in Chapter 5 isn't light enough to meet the mass requirements needed for geo orbit. The half-meter prototype described in this chapter is over two times less massive than the NMSD mirror, and it meets the mass requirements for imaging from geo orbit.

6.2 Design and fabrication

The immediate predecessor to this project was the 2 m UA NMSD mirror that I discussed in Chapter 5. The NMSD mirror uses a 2 mm thick glass facesheet as the reflective surface. The composite structure holds 166 actuators, and each of the 127 interior actuators is coupled to the glass via a nine-point whiffle tree. The facesheet was designed and fabricated at the University of Arizona, and the completed mirror weighs 86 pounds and has an areal density of 12 kg/m^2.

The customer for the 0.5 m prototype determined that a successful geo telescope should possess an areal density of approximately 5 kg/m^2 for the primary mirror. The NMSD mirror technology was not light enough for this project; however, the NMSD

	2 m NMSD	0.5 m Demo
Mirror diameter	2 m	0.5 m
Glass thickness	2 mm	1 mm
Actuator mass (each)	40 g	5 g
Reaction structure areal density	3.2 kg/m^2	1.1 kg/m^2
Total areal density	**12.4 kg/m$^{\mathbf{2}}$**	**5.2 kg/m$^{\mathbf{2}}$**

TABLE 6.1. Comparison of the 2 m NMSD and the 0.5 m demonstration mirror's fabrication parameters. The half meter's glass facesheet is half as thick, and the actuators are a scant 5 grams (0.01 lbs). Note that the total areal density includes the glass facesheet, the actuators, loadspreaders, support structure, and all of the on-board wiring.

mirror served as an important starting point for the 0.5 m prototype.

This 0.5 m prototype started out with the same design philosophy as the NMSD mirror, but all of its parts were miniaturized and aggressively lightweighted. Table 6.1 shows a comparison between the NMSD mirror discussed in Chapter 5 and the 0.5 m prototype. The 0.5 m mirror represents the lightest Arizona MARS mirror to date, and it is currently the lightest glass mirror of its size in the world.

6.2.1 Component fabrication

The support structure is shown in Figure 6.1. It was designed at the Univ. of Arizona and fabricated at Composite Optics, Inc. (COI). The structure was made by sandwiching several layers of carbon fiber and epoxy together. Carbon fiber is an ideal material for this project because the resulting structure is extremely stiff and very lightweight. The facesheet and backsheet are both 0.015" thick, and the webs are 0.010" thick. The entire structure has been aggressively lightweighted by cutting holes into the face/backsheets and ribs. The actuators are mounted in the 31 reinforced holes. The structure is concave such that the actuators are mounted normal to the glass. The completed shell is shown in Figure 6.1.

The actuators are a miniaturized version of the NMSD actuators discussed in

FIGURE 6.1. Left: Paul Gohman holds the completed support structure. The structure is 0.5 m (20") tip-to-tip and is less than 1" thick. Right: Line drawing of the support structure. This structure is a meniscus-shaped sandwich: note that all of the components have been aggressively lightweighted. The actuators are mounted in the reinforced holes in the facesheet. (Line drawing by Randall Hodge.)

Section 5.1.4. The actuators used for this project are similar to the one shown in Figure 5.7. The actuators are an impact-driven model designed and built at the Univ. of Arizona. There are two advantages to using an impact-driven actuator. First, the design works at cryogenic temperatures. Second, the actuators are "set and forget": they do not require a power source to maintain their position. This is an important requirement because space imaging systems have limited power resources.

A picture of the 5 gram actuator is shown in Figure 6.2. The average step size is 20 nm without any loading. Each step requires an average pulse amplitude of 700 mA for 1.5 ms.

The thin glass membrane was created using conventional techniques and existing tooling within the optics shop. The fabrication process is illustrated in Figure 6.3. The process started with a large Zerodur glass blank.[1] The optical surface (concave) was then generated and polished using conventional tooling. The remaining steps shown in Figure 6.3 are necessary for thinning the glass down to its final thickness. Before all of the excess glass can be removed, the thick blank must be attached to a rigid body such that it does not bend during the glass removal. This rigid body is

[1] Zerodur is a special glass with a low coefficient of thermal expansion. These types of special material considerations are important for space applications.

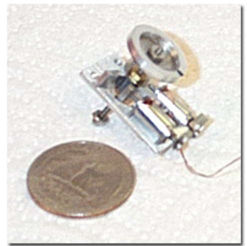

Figure 6.2. A tiny actuator. One of the half meter's actuators, placed next to a US quarter for scale. The actuators are 5 grams (0.01 lbs) and have a nominal step size of 20 nanometers. This picture shows the key components of the actuator's mechanism: the two electromagnetic coils on either side of a nut, an 80 tpi machine screw, and a rectangular aluminum mounting plate.

referred to as a *blocking body*, and a plano-convex piece of granite was used in this instance. The blank was attached to the blocking body with pitch, and several inches of the rear surface were generated off using a diamond cutting tool. Finally, the rear (convex) surface was ground and polished to remove any microfractures.

After the polishing was complete, the facesheet remained attached to the blocking body. At this point, the design team decided to attach the loadspreaders to the rear (non-optical, convex) surface of the meniscus. This decision was made because the loadspreaders served a useful purpose during the deblocking process. Once all of the loadspreaders were attached, they served as a convenient grip during the de-blocking process.

Unlike the complicated deblocking process described in Chapter 5.1.2 for the 2 m mirror, the procedure for this mirror was considerably simpler. Because the substrate was only 0.5 m in diamater, the optician was able to remove the substrate by hand. Figure 6.4 shows Steve Miller removing the facesheet from the granite blocking body. Steve placed the facesheet and blocking body in the Steward Mirror Lab's cube meter oven for 10 hours at 200 degrees Celsius. During this soak, the pitch softened enough such that the facesheet could be easily slid off the blocking body.

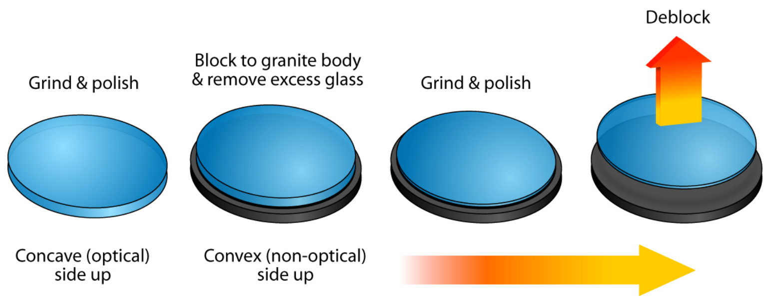

FIGURE 6.3. The glass fabrication process. The process starts with a meniscus-shaped glass blank. The concave optical surface is polished while the blank is thick. This allows the opticians to use standard polishing techniques and their existing tooling. After the optical surface is finished, it is bonded to a granite blocking body using pitch. After attachment, the excess glass is removed from the convex side using a diamond cutting tool. Finally, the convex side is ground and polished to remove any micro-fractures. When the optical finishing is complete, the facesheet is removed from the granite body.

FIGURE 6.4. Steve Miller deblocks the facesheet. The glass and blocking body sat in a 200 degree C oven for 10 hours before Steve gently pulled the glass off the granite blocking body. At 200 degrees Celsius, pitch has the consistency of thick honey, and Steve was able to safely remove the glass.

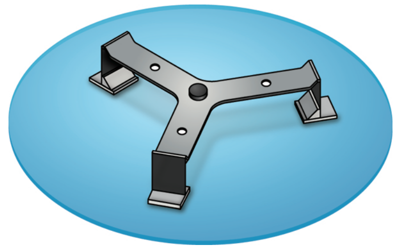

Figure 6.5. Loadspreader used on the UA half-meter prototype. The three feet are attached to the glass using Q3-6093 RTV adhesive, Figure 6.6. The feet are attached to the main loadspreader arm using thin steel flexures. The actuator picks up the loadspreader at a small magnet located in the center of the loadspreader arm. (There is an additional component that is not shown: a sapphire window sits on top of the magnet. This allows for a quasi-point contact between the actuator and the loadspreader.)

6.2.2 A scheme for attaching the loadspreaders

The loadspreaders for this project were a simple three foot whiffle tree made from aluminum and spring steel. A schematic of a single loadspreader is shown in Figure 6.5. The feet are attached to the main aluminum loadspreader body via thin steel flexures.[2] The mechanical design of this loadspreader allows for thermal expansion and contraction of the loadspreader tree without influencing the surface quality of the glass facesheet.

The three feet were attached to the glass using Dow Corning's Q3-6093 RTV adhesive. This adhesive was chosen because it possesses several attractive mechanical properties that were useful for this application. Figure 6.6 shows a cartoon of one of the RTV interfaces between the aluminum foot and the glass facesheet. When RTV adhesive cures, it has a rubbery consistency. This allows for a certain amount of motion in a direction parallel to the facesheet because the RTV pad is compliant

[2]Because this was a demonstration project, the design team did not construct the loadspreaders out of space-appropriate materials. A space-hardened version of this mirror would replace the aluminum loadspreaders with a more appropriate material, like Invar or a graphite composite.

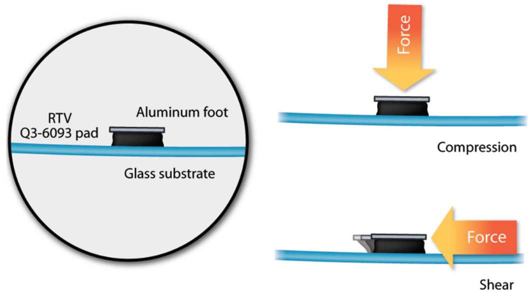

FIGURE 6.6. The effects of using an RTV adhesive. The RTV pad that results from bonding resists compressive forces, but it yields in shear.

in shear.[3] By contrast, the bond does not allow for much movement in compression. In addition to these mechanical features, the tensile strength of the bond is 325 psi. Finally, the Mirror Lab's engineers are partial to this particular RTV because they have a lot of experience working with it.

As I mentioned above, the design team elected to attach the loadspreaders after the rear convex surface was polished, but before the glass was deblocked from the granite blocking body.[4] The loadspreader attachment caused some concern because the thin facesheet would be sensitive to moments introduced by the loadspreaders (via the actuators) at the attachment points. For example, if the loadspreaders were not attached in a stress-free state, they would impart moment on the glass, and this would result in a surface error above each foot. As a result, Brian Cuerden and I developed a procedure for attaching the feet such that they would impart little or no moment into the facesheet. Our finalized procedure is described in the following list, and Figure 6.7 illustrates each of the steps.

1. First, I cleaned the glass surface using four solvents in the following order: 1,1,1 trichoroethane, acetone, isopropyl alcohol, and ethanol. I also cleaned all of the loadspreader parts in successive baths using these solvents.

[3]Shear is discussed in Section 4.1.2.

[4]The loadspreaders were attached between the third and fourth steps shown in Figure 6.3.

2. I applied a fiberglass bonding template to the glass surface. The template was designed at the University of Arizona and fabricated at Composite Optics. The template has openings for each of the loadspreaders, and each opening is flanked by two tooling/fiduciary holes.

3. For each loadspreader, I began by placing three teflon spacers in the approximate locations for bonding. These horseshoe-shaped spacers were used to achieve a particular bond thickness between the loadspreader foot and the glass. At this time, I also placed a pin in each of the two tooling holes.

4. Next, I placed some RTV adhesive inside each of the teflon spacers. (The RTV was outgassed for 5 minutes in a vacuum chamber before it was applied.)

5. For the next step, I placed the aluminum feet on top of the teflon spacers. When they were in their nominal location, I placed a tooling bar across the hole in the template. The bar had two holes which slid over the two pins placed in step 3.

6. To locate the feet in the precise locations, I used a jig that we built specifically for this purpose. This jig looked similar to the main loadspreader arm except that it was much thicker. I screwed the jig down to the tooling bar described in step 5. The jig had an aluminum fixture attached to each end that allowed for adjusting the feet to their precise locations.[5]

7. After the feet were positioned, I carefully unscrewed the jig used to position the feet. I then screwed the real loadspreader arm into the tooling bar. Because of the geometry, a spacer was needed between the arm and the bar.

8. At this point, the feet and loadspreader arm were located in their correct locations. I then attached the flexures that connect each arm segment to a foot. I used the RTV for this attachment.

[5] The work time of the RTV was approximately 45 minutes. During this time, it had the consistency of toothpaste, and I was able to make minor adjustments in the foot locations.

9. To complete the procedure, I allowed the RTV to cure overnight. Finally, I unscrewed the loadspreader arm from the tooling bar, and I slipped the bar out from beneath the arm.

This procedure was developed as a result of several iterations using the loadspreaders on a 1 mm thick piece of dummy Borofloat glass. These trials allowed us to improve upon the loadspreader design such that the final design contained fewer pieces than the original model. The final loadspreader design was more accurate because fewer pieces had to be screwed together, and the assembly procedure was simpler.

We were also able to measure the effects that our attachment scheme had on the glass. Figure 6.8 shows a sample loadspreader bonded onto a test piece of 1 mm thick float glass. After using our procedure to attach the loadspreader, I placed the test piece on an optical flat under a [partially coherent] sodium lamp. The resulting interference fringes are shown in Figure 6.8. The overall figure of the test piece is terrible; however, the important result is that there is no noticeable distortion around each foot.[6] This shows that the attachment procedure imparts little or no stress on the local region around each foot.

6.3 Metrology

The assembled mirror is shown in Figure 6.9. The mirror's mass is 1.17 kg: this includes the actuators, loadspreaders, glass, reaction structure, and all of the onboard wiring. The mirror was attached to a tip/tilt stand via the three hardpoints shown in Figure 6.9.

The mirror was tested at its center of curvature using a phase-shifting Twyman-Green interferometer.[7] This particular interferometer operated at 633 nm, and it

[6] If there was a disturbance due to the foot, one would see a break in the contour lines around each attachment point.

[7] A phase-shifting interferometer gathers three or more frames of interferograms that are each 90

FIGURE 6.7. Procedure for attaching loadspreaders in a stress-free manner. 1. I started with the bare glass after it was polished but before it was deblocked. The loadspreaders were attached to the rear, convex (non-optical) surface. 2. A bonding template was applied to ensure the loadspreaders were placed in the correct location. 3. Teflon spacers were used to regulate the bond thickness. Also, two tooling pins were placed in corresponding holes on the bonding template. 4. Epoxy was applied to the glass inside the teflon spacers. 5. The feet were placed on the spacers and near their nominal positions. 6. A tooling bar and dummy loadspreader were used to position the feet to their exact locations. 7. The dummy loadspreader was removed and replaced with the actual loadspreader arm. The loadspreader arm was screwed into the tooling bar to ensure it was located in the correct position. 8. The tooling bar was removed. 9. The final five loadspreaders were attached. 10. The bonding template was removed. The glass was now ready for deblocking.

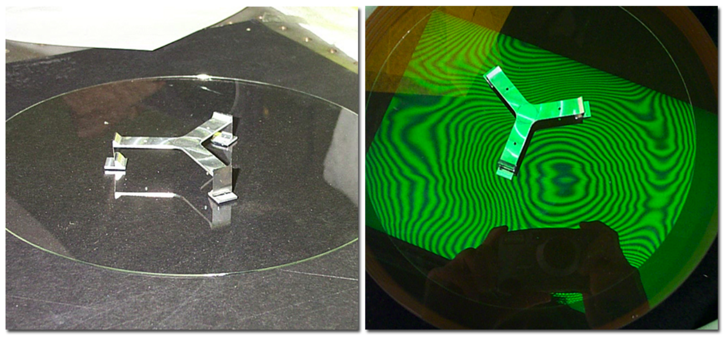

FIGURE 6.8. Test coupon and resulting interference fringes. The test loadspreader on the left is attached to a 6” piece of float glass that is 1 mm thick. The interferogram on the right shows that the contour lines are not distorted around each foot.

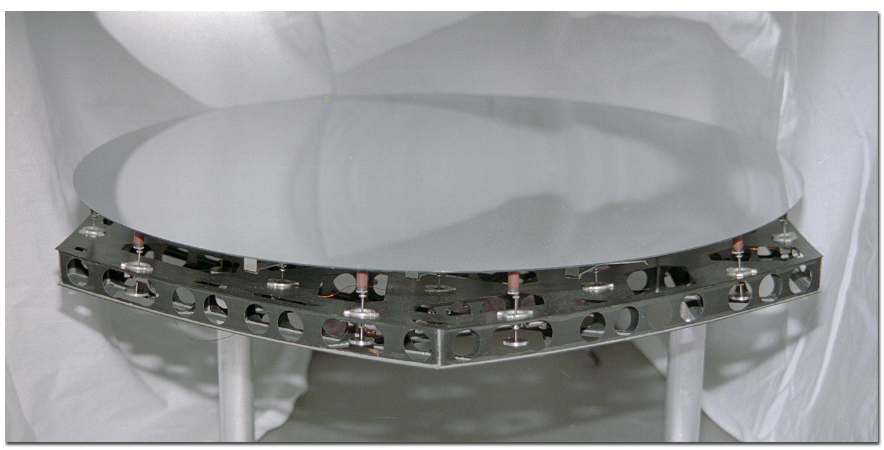

FIGURE 6.9. The finished half-meter prototype. The 1 mm thick glass facesheet has an aluminum coating. In this image, the edge actuators are clearly visible. (The edge actuators do not use loadspreaders.) The actuator screws and inertial masses (aluminum discs attached to the screws) are also clearly visible. Note how aggressively the support structure has been lightweighted. (Photo: Lori Stiles, UA News Services)

was unique in that it actively compensated for piston caused by vibration. [29] I used Durango to run the interferometer and collect the data.[8]

The actuators were controlled via a set of control electronics, and the user adjusted the actuators using a Windows program running on a PC. The program allows for individual adjustment of the actuators, or an entire "move map" can be imported to move all of the actuators at once. The features of this program are discussed in more detail in Section 6.3.2.

6.3.1 Measurement scheme and results

As with the mirror described in Chapter 5, the surface figure does not assume the correct figure when the mirror is initially assembled. However, unlike the 2 m, this mirror was considerably easier to actuate. This mirror was small enough that I was able to implement an intuitive, efficient method for quickly advancing all of the actuators to their nominal positions.

I started by advancing three actuators such that they were a few millimeters higher than the remaining 28 actuators. I chose the initial actuators for their symmetry: each actuator was at the vertex of an equilateral triangle. With the mirror resting on these three points, I adjusted each of the three actuators until the return spot at the mirror's center of curvature possessed three-fold symmetry. Then I added three more actuators such that the mirror was resting on the vertices of a hexagon. Again, I adjusted the actuators until the return spot possessed six-fold symmetry. I continued in this manner until all of the actuators were attached. At this point, the mirror was good enough to begin using the visible Twyman-Green interferometer to take surface measurements.

---

degrees out of phase with each other. The extra phase information allows the user to calculate a surface map of the mirror's figure. For more information about phase-shifting interferometry, John Greivenkamp's chapter in *Optical Shop Testing* is an excellent introduction to the subject. [11]

[8]Durango is a piece of third-party software used to drive phase-shifting interferometers. It commands the interferometer to take several frames of phased interferograms; it collects the resulting images; and it generates a surface map from the data.

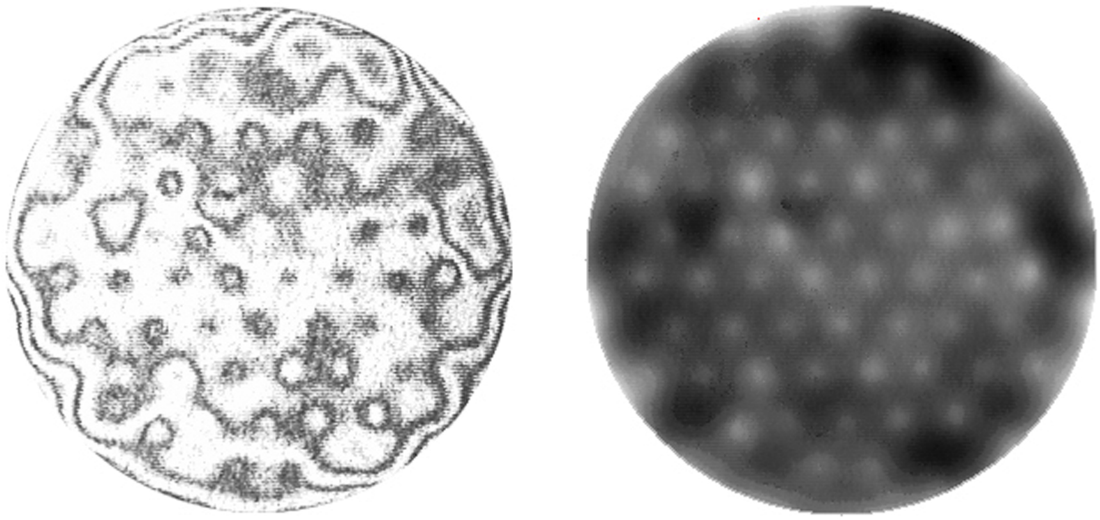

FIGURE 6.10. Final interferogram and surface map for the half-meter prototype mirror. The surface map represents a figure of 0.248 waves RMS (HeNe). (This is equivalent to 157 nm RMS.) The white areas are high and the dark areas are low. The bumps are due to self-weight deflection, discussed in Section 6.3.3. Incidentally, these bumps were an effective qualitative tool useful for improving the surface figure. Bumps that are too bright mean the actuator underneath is pushing harder than its neighbors. Non-existent (or subdued) bumps represent actuators that are not providing enough support.

Once all of the actuators were attached, it took about 8 hours to achieve the final surface shown in Figure 6.10. For the most part, I used a least-squares algorithm (described in Section 5.3) to improve the figure. However, once the figure was nearly complete, I spent several hours fine-tuning the positions of individual actuators.[9]

6.3.2 Mirror control software

During a subsequent experiment on the 0.5 m mirror, I wrote my own actuator control software. The previous software was written by a programmer at Steward Observatory, and, while this resulted in a technically-sound program, it lacked several

[9] Adjusting a high-authority mirror is similar in feeling to being in Las Vegas. Every time an actuator is moved, you risk losing everything in return for very little gain.

helpful features for successful mirror actuation.

Figure 6.11 shows a screenshot of the control program that I wrote. While this specific program might not be helpful to future researchers, the list of features should be considered essential elements for any future mirror control software:

- The program works like this: the user enters actuator commands and then clicks on the "Send to Mirror" button to send the commands to the actuators.[10]

- There are several ways to enter the commands. There is a spreadsheet at the left which is used to enter full arrays of actuator commands. Alternatively, the user can click the top number next to each actuator location and enter the command manually. As described in Section 6.2.1, the actuators move in discrete steps. As a result, each actuator command is an integer (positive for advance and negative for retreat) which represents an integer number of steps up or down. The actuators can also be incremented by clicking on the up/down arrows next to each actuator. Finally, the program can read in an ASCII file containing a full list of actuator commands. This is helpful when an external program (such as MatLAB or IDL) is used to calculate which way the actuators must move next. (The algorithm that I used is described in Section 5.3.)

- The program keeps track of the previous actuator activity. The cumulative total of each actuator's steps is represented next to each actuator as the lower number. By clicking on the curly arrow next to each actuator, the actuator's *negative* cumulative history is loaded in as the next command. (This is effectively an "undo" button.)

- The entire set of actuator commands can be scaled or summed by a separate factor. This is accomplished by using the two entry boxes labeled "X" and "+"

[10] For this particular program, the graphical user interface (shown in Figure 6.11) sends the commands to a small C program, which then communicates with the actuator hardware via the serial port.

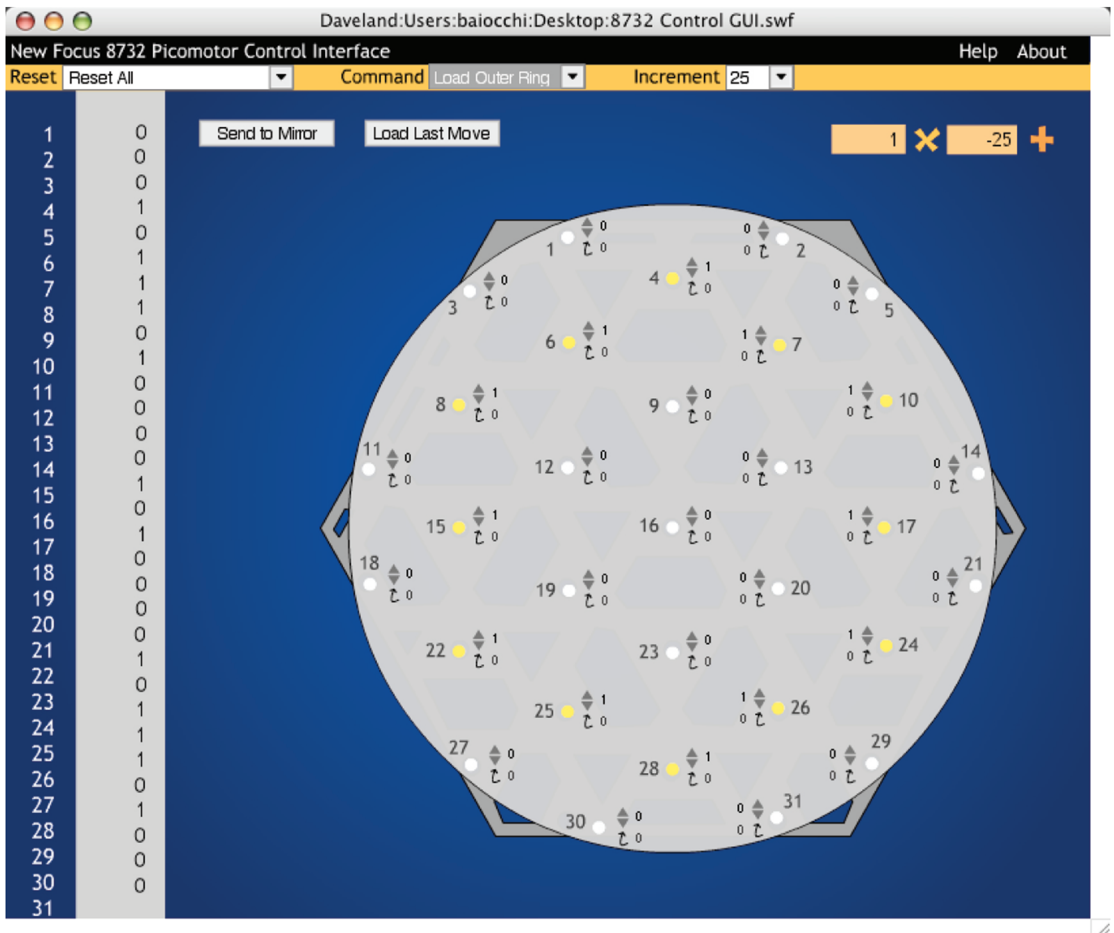

FIGURE 6.11. Control program for the 8732 New Focus Picomotor driver. I designed this program after having worked on four different active mirrors. As such, I was able to include several features that will certainly prove useful for any future application involving actively-controlled mirrors.

in the upper right hand corner. For example, pushing the "+" sign in its current state will subtract 25 from all of the current actuator commands.

- When an actuator contains an active command (meaning that it will move when "Send to Mirror" is clicked) the white dot symbolizing the actuator's position turns yellow. This allows the user to quickly visualize which portions of the mirror will move next.

- Clicking on the "Load Last Move" button loads the last move in as the next command to be executed. This allows the user to repeat the last move. Alternatively, the user can click on "Load Last Move" and then multiply the entire set by -1 to undo the last move.

- The "Reset" drop-down contains several useful features for resetting global parameters. "Reset All" resets the entire program: actuator commands, histories, and scaling factors. "Reset Commands to Zero" resets all of the current commands to zero, but it leaves the actuator histories intact. "Reset Commands to One" resets all of the current commands to one, and it also leaves the actuator histories intact. "Reset History" resets the histories to zero.

- The "Command" drop-down box contains several useful features for working with different parts of the mirror. "Load History" moves all of the actuator histories to the active command. "Load -(History)" loads the opposite of the history to the active command such that all the cumulative commands may be undone. Finally, the last four commands load a "1" as the active command for the appropriate group: "Load Edge", "Load Center 19", "Load Inner Ring", or "Load Outer Ring". This is helpful for correcting circularly symmetric aberrations, like spherical aberration or defocus. It's also useful for adjusting the mirror's radius of curvature.

- The "Increment" drop-down box is helpful when the actuators must move in large increments. It contains the following options: 1, 5, 25, 50, 250, 500, and 1000. When one of these integers is selected, it does two things. First, it enters that number into the sum box (next to the "+" sign). Also, it changes what happens when the user clicks on the up/down arrows. For example, if an increment of 250 is selected, clicking on the arrows advances the commands in increments of 250. Again, this is a helpful feature if the actuators must be moved long distances. (Which is typical during initial actuation.)

6.3.3 Limiting circumstances: self-weight deflection

The final surface figure shown in Figure 6.10 contains several localized bumps. These features are a side effect of using such a thin facesheet on Earth: gravity causes the glass to sag about each of the support points. In space, of course, this problem doesn't exist because the mirror won't be subjected to the Earth's gravitational effects. In the meantime, we say that the surface quality is limited by its *self-weight deflection*.

6.3.4 A space-hardened design

The next major step for this mirror—indeed, the entire family of Arizona MARS mirrors—is to launch a space-hardened version of the 0.5 m prototype. This involves packaging a mirror along with a system that can monitor and correct the surface figure as the mission progresses. The package would then be flown on a future flight mission. The purpose of this test will be to investigate the following issues:

- Transition from stowed to active mode. The MARS mirrors are rather fragile, especially when compared to the thick glass mirror used in the Hubble Space Telescope. As such, it would be wise to protect the mirrors during launch by placing the mirror in a "stowed mode". This scheme uses a set of launch restraints to pull the glass back against the actuators. Once on orbit, these mechanical restraints are released, and the actuators are free to push and pull according to the MARS design. A flight mission would show that the launch restraints are effective in preserving the mirror's integrity during the launch sequence.

- Survivability. During the early part of the Arizona MARS research, the design team conducted a survivability study to determine the design's ability to survive launch. A dummy mirror was tested in an acoustic chamber and it survived. However, this dummy mirror was constructed using float glass, machine-screw actuators and an aluminum support structure. A mission test would prove that the MARS design is robust enough to survive the space environment.

- System performance in a zero gravity environment. As discussed in Section 6.3.3, the surface figure of the mirror is limited by its self-weight deflection. There are calculations that can predict what the figure will look like in a zero gravity environment, but these predictions are only as good as the finite-element model used to create them. Placing a mirror on orbit will be an important experiment to demonstrate the surface figure characteristics of the MARS mirrors.

6.4 Chapter summary

In this chapter, I described the fabrication and control of the Arizona ultralightweight half-meter prototype mirror. This mirror, weighing in at only 2 pounds, represents the lightest glass mirror in the world for its size. Throughout the chapter, I covered the following important topics on the practical aspects of building and controlling such a mirror:

- Geosynchronous orbit is a desirable location for an Earth-imaging satellite because it remains over a fixed ground location as the Earth rotates. This allows for constant monitoring of the subject of interest. The disadvantage to geo orbit is that it is 22,200 miles above Earth: ultralightweight optics are needed for imaging systems at this distance.

- The design of the half-meter was based on the NMSD mirror (Chapter 5). Using the NMSD as a starting point for the design, *everything* was lightweighted in an effort to minimize the mass. Table 6.1 shows the differences between the NMSD and the half-meter's components.

- I developed a procedure for attaching the loadspreaders to the glass to ensure a stress-free contact, Figure 6.7. I showed that very little local distortion results when using this procedure, Figure 6.8. The bonding procedure is described in Section 6.2.2.

- I described a simple technique for starting the actuation process right after the mirror is assembled. By setting the glass on three actuators, I was able to use symmetry to improve the mirror's figure. This technique is discussed in Section 6.3.1.

- I developed a software package to control the mirror's actuators. While this specific piece of software may not be useful for future projects, the features that I included should be an essential part of any future effort. A list of these features is described in Section 6.3.2.

References

[1] Roger Angel, B. Martin, S. Miller, J. Burge, P. Hinz, and N. Woolf. NGST as a fully assembled 6-m telescope, using a monolithic MARS mirror. *NASA White Paper*, 1997.

[2] Dave Baiocchi, James H. Burge, and Brian Cuerden. Demonstration of a 0.5-m ultralightweight mirror for use at geosynchronous orbit. In H. Philip Stahl, editor, *Optical Manufacturing and Testing IV*, volume 4451 of *Proc. SPIE*, pages 86–95, 2001.

[3] William P. Barnes. Optimal design of cored mirror structures. *Applied Optics*, 8(6):1191–1196, June 1969.

[4] William P. Barnes. Hexagonal vs triangular core lightweight mirror structures. *Applied Optics*, 11(12):2748–2751, December 1972.

[5] James H. Burge, Dave Baiocchi, and Brian Cuerden. Ultralightweight active mirror technology at the University of Arizona. In M. A. Kahan, editor, *Optomechanical Engineering 2000*, volume 4198 of *Proc. SPIE*, pages 230–241, 2000.

[6] James H. Burge, B. Cuerden, S. Miller, R. C. Crawford, R. W. Wortley, and D. G Sandler. Manufacture of a 2-m mirror with a membrane facesheet and active rigid support. In H. P. Stahl, editor, *Optical Manufacturing and Testing III*, volume 3782 of *Proc. SPIE*, pages 123–133, 1999.

[7] James H. Burge, Scott T. DeRigne, James Roger P. Angel, Brian Cuerden, S. Clapp, G. Rivlis, Patrick M. Woida, Paul Gohman, Steve Bell, and R. Kingston. NGST mirror system demonstrator from the University of Arizona. In H. Philip Stahl, editor, *Optical Manufacturing and Testing IV*, volume 4451 of *Proc. SPIE*, pages 27–38, 2001.

[8] Brian E. Catanzaro, Dan Keane, Steven J. Connell, Dave Baiocchi, James H. Burge, Arup K. Maji, and Michael K. Powers. Ultralite/glass composite hybrid mirror. In James B. Breckinridge and Peter Jakobsen, editors, *UV, Optical and IR Space Telescopes and Instruments*, volume 4013 of *Proc. SPIE*, pages 663–671, 2000.

[9] Ronald Florence. *The Perfect Machine: Building the Palomar Telescope*. HarperCollins, 1994.

[10] Jack D. Gaskill. *Linear Systems, Fourier Transforms, and Optics*. John Wiley & Sons, 1978.

[11] John G. Greivenkamp. *Optical Shop Testing*, chapter Phase Shifting Interferometry, pages 501–598. Wiley-Interscience, second edition, January 1992.

[12] John W. Harris and Horst Stocker. *Handbook of Mathematics and Computational Science*. Springer, 1998.

[13] Eugene Hecht. *Optics*. Pearson Addison Wesley, fourth edition, August 2001.

[14] Russell C. Hibbeler. *Mechanics of Materials*. Macmillan Publishing Company, first edition, 1991.

[15] Steve E. Kendrick, David Chaney, and Robert J. Brown. Optical characterization of the beryllium semi-rigid AMSD mirror assembly. In H. Philip Stahl, editor, *Optical Manufacturing and Testing V*, volume 5180 of *Proc. SPIE*, pages 180–187, 2004.

[16] Daniel Malacara. *Optical Shop Testing*. Wiley-Interscience, second edition, January 1992.

[17] Hubert M. Martin, Richard G. Allen, James H. Burge, Lee R. Dettmann, Dean A. Ketelsen, Stephen M. Miller III, and Jose M. Sasian. Fabrication of mirrors for the Magellan Telescopes and the Large Binocular Telescope. In Jacobus M. Oschmann and Larry M. Stepp, editors, *Large ground-based telescopes*, volume 4837 of *Proc. SPIE*, pages 609–618, 2003.

[18] Pravin K. Mehta and Paul B. Reid. Mathematical model for optical smoothing prediction of high-spatial-frequency surface errors. In Eddy A. Derby, Colin G. Gordon, Daniel Vukobratovich, Jr. Paul R. Yoder, and Carl H. Zweben, editors, *Optomechanical Engineering and Vibration Control*, volume 3786 of *Proc. SPIE*, pages 447–459, 1999.

[19] J. L. Meriam. *Statics*, volume 1. John Wiley & Sons, 1980.

[20] Jerry E. Nelson, Jacob Lubliner, and Terry S. Mast. Telescope mirror supports: plate deflections on point supports. In Lawrence D. Barr and Geoffrey Burbidge, editors, *Advanced Technology Optical Telescopes I*, volume 332 of *Proc. SPIE*, pages 212–228, 1982.

[21] John W. Pepi. Design considerations for mirrors with large diameter to thickness ratios. In Paul R. Yoder, editor, *Optomechanical Review*, volume CR43 of *SPIE Critical Reviews*, pages 207–231, 1992.

[22] Ralph M. Richard and A. J. Malvick. Elastic deformation of lightweight mirrors. *Applied Optics*, 12(6):1220–1226, June 1973.

[23] Simon C. F. Sheng. Lightweight mirror structures best core shapes: a reversal of historical belief. *Applied Optics*, 27(2):354–359, January 1988. This paper argues that Barnes's 1972 paper (Hexagonal vs Triangular Core Lightweight Mirror Structures) came to an incorrect conclusion about the ideal geometry.

[24] S. Timoshenko. *Strength of Materials Part I: Elementary Theory and Problems*. D. Van Nostrand Company, third edition, 1955.

[25] S. Timoshenko. *Strength of Materials Part II: Advanced Theory and Problems*. D. Van Nostrand Company, third edition, 1956. The derivation of flexural rigidity is on page 77.

[26] Michael Thomas Tuell. Novel tooling for production of aspheric surfaces. Master's thesis, The University of Arizona, Tucson AZ, 2002.

[27] Daniel Vukobratovich. Rugged yet lightweight: How can we achieve both in optical instruments. In Paul R. Yoder, editor, *Optomechanical Review*, volume CR43 of *SPIE Critical Reviews*, pages 18–60, 1992.

[28] Daniel Vukobratovich, Bijan Iraninejad, Ralph M. Richard, Q. M. Hansen, and R. Melugin. Optimum shapes for lightweighted mirrors. In Paul R. Yoder, editor, *Advanced Technology Optical Telescopes*, volume 332 of *Proc. SPIE*, pages 419–423, 1982.

[29] Chunyu Zhao and James H. Burge. Vibration-compensated interferometer for measuring cryogenic mirrors. In H. P. Stahl, editor, *Optical Manufacturing and Testing III*, volume 3782 of *Proc. SPIE*, pages 399–406, 1999.

Appendix A

Glossary of terms, acronyms, and abbreviations

AMSD Advanced Mirror System Demonstration. A precursor to the NGST mirror, the AMSD mirrors were built as technology demonstrations as part of an early phase of the NGST prime contractor selection. Two competing AMSD mirrors were built: Ball Aerospace's is a 1.2 m beryllium mirror and Kodak's is a 1.4 m (point-to-point) ULE passive mirror with active support.

AO Adaptive Optics. AO systems use deformable mirrors to correct for aberrations in real time. Astronomers use AO to remove the effects of atmospheric turbulence while the telescope is in use. (This is done by placing a deformable mirror somewhere in the telescope. The atmosphere is measured using a wavefront sensor, and the (negative) wavefront shape is fed into deformable mirror. In this way, the atmosphere's turbulence is effectively subtracted from the beam path before the star light ever reaches the CCD.) Good AO systems are complicated and expensive. However, the University of Arizona's recently-upgraded Multiple Mirror Telescope is a prime example that AO systems are going to change the state of telescope instrumentation.

areal density A metric used by the mirror community to describe the total mass as related to the mirror's clear aperture. The areal density is calculated by taking the mirror's mass and dividing by the surface area. The Hubble's primary has an areal density of 180 kg/m^2. Arizona's mirrors have an areal density in the range of 5 - 25 kg/m^2.

aspect ratio The aspect ratio (as it pertains to mirrors) refers to the ratio of the diameter to the width. Conventional passive mirrors have an aspect ratio of 5 or 10. The UA glass facesheets have aspect ratios near 500 or 1000.

Be beryllium. A metal used for mirror substrates. It has an unusually high specific stiffness.

blank, mirror The blank is a solid piece of glass that gets generated, ground, and polished to form a mirror (or a lens). Put another way, the blank is the piece of raw material that will eventually become the mirror.

blocking body A rigid body used during the glass fabrication process. The substrate is attached to the blocking body before it is ground and polished such that it remains rigid throughout the fabrication process. The substrate is removed from the blocking body when the optical finishing is complete. The process of attaching the two pieces is called "blocking", and the parts are separated by "deblocking" them.

CCD Charged Coupled Device. Basically, a CCD is a video camera. Each pixel converts incident photons to a proportional charge. In most circumstances, all of the charges are converted to a digital signal by a computer, and the resulting image is displayed on a monitor for the user to view.

centroidal axes The centroidal axes intersect at the center of mass.

COI Composite Optics, Inc. Located in San Diego CA, COI fabricated all of the composite support structures used in the Univ. of Arizona MARS-type demonstrations.

CTE Coefficient of Thermal Expansion, α. Most materials expand when heated and contract when cooled. The CTE is a way of quantifying this effect. It typically has units of parts-per-million per degree Celsius. For example, optical glass has a CTE of $\sim$ 7 ppm/^{o}C. A meter-long bar of glass would therefore expand by 7 millionths of a meter if heated by 1^{o} C. See Section 2.2.

deblocking The process of removing the polished glass facesheet from the blocking body. For small (< 0.5 m) mirrors, the faceheet and blocking body are placed in an oven, and the glass is carefully slid off the blocking body. See Figure 6.4.

E6 E6 is an optical glass made by OHara in Japan. It's a favorite glass at the University of Arizona for a few reasons. It has a very low coefficient of thermal expansion (1.61×10^{-6} parts/°F). OHara makes large quantities of this glass, and their process is maintained such that the chemical properties of each batch are nearly identical. (This is important if several batches of glass are all melted down into one solid piece, as they do at the Steward Mirror Lab.)

generation The first step in the polishing process. The optician can use a grinding tool to remove excess glass, but this can be very time consuming if several millimeters must be removed. Instead, the optician can use a generating machine: this uses a diamond cutting tool to quickly remove excess glass from the blank. Often times, the diamond tool leaves a series of small grooves (like a record player), and these are ground out in subsequent operations.

geo orbit See **geosynchronous orbit**.

geosynchronous orbit Geo orbit is located 35,793 km (22,241 miles) above the Earth's surface. (Compare this to 320 - 800 kilometers for low Earth orbit.) This orbit is ideal for Earth-imaging systems because the satellite remains permanently fixed over the same location on the ground. The long distances involved present advantages and disadvantages. An advantage is that fewer satellites are necessary to image the entire globe. A big disadvantage is that significantly larger apertures are required to achieve the same resolution as a satellite in low Earth orbit.

HeNe Helium-Neon. In optics, this abbreviation refers to a helium neon laser. While HeNe lasers can operate at many wavelengths, the most common is 632.8

nanometers. The abbreviation HeNe is usually used to clarify a metrological quantity. For example, a surface might be reported to be good to 0.75 waves RMS (HeNe). Since 'waves' is a unit that is dependent on wavelength, it is appropriate to list the wavelength at which the part was measured. In this case, it was measured with a helium neon laser (632.8 nm). To complete the conversion, 0.75 of one wavelength is as follows: $0.75 \times 632.8\,\mathrm{nm} = 474.6\,\mathrm{nm}$. Thus, saying that something is 0.75 waves at HeNe is equivalent to 474.4 nanometers.

HST Hubble Space Telescope.

inflection point The point where a curve changes concavity. For example, the curve would be concave up on one side of the curve and concave down on the other. Inflection points occur where the second derivative of the curve is equal to zero.

interference fringes/interferogram Simply put, an interferogram can be thought of as a contour map that shows the shape change between a test surface and a reference surface. Interference fringes are a result of the wave-like nature of light: just as waves in a swimming pool can destructively and constructively interfere, so can light.

Invar Invar is a composite metal that has nearly zero CTE. It is expensive, dense, and difficult to machine.

IR Infrared. Infrared radiation generally refers to electromagnetic waves that have a wavelength from 1 - 30 microns. These wavelengths are not part of the visible spectrum.

JPL Jet Propulsion Lab. Run for NASA by CalTech and located in Pasadena CA.

JWST James Webb Space Telescope. The new name of the NGST.

LEO See **low Earth orbit**.

low Earth orbit (LEO) LEO satellites are located anywhere from 320 - 800 kilometers (200 - 500 miles) above the Earth's surface. Because they are located so close, they must travel very quickly to remain in orbit. This results in a very short period of revolution: the average LEO satellite takes about 90 minutes to complete one revolution around the Earth.

LS Least squares. An algorithm used to simultaneously solve for several variables at once. See Section 5.3.

LW'd lightweighted.

MSFC Marshall Space Flight Center. One of NASA's administrative offices, located in Huntsville AL. Marshall is the home of the space optics directorate.

neutral axis The line (or plane) of fibers that do not experience strain during bending. For pure bending, the neutral axis contains the section's centroid. [24]

NGST Next Generation Space Telescope. The original name of the telescope scheduled to replace the Hubble. The current launch date is August 2011.

NMSD NGST Mirror System Demonstration. A precursor to the NGST mirror, the NMSD mirrors were built as full-scale technology demonstrations. Two NMSD mirrors exist: the Univ. of Arizona's glass/composite mirror and Composite Optics's full composite mirror. Neither system was ever finished to NASA's initial specifications. See Chapter 5 for more information about the University of Arizona NMSD.

OSC Optical Sciences Center.

passive mirror A passive mirror depends on its thickness to maintain its stiffness. Oftentimes, passive mirrors are supported on an array of actuators to correct for errors with a large spatial period. These mirrors are referred to as "passive mirrors with active supports." Modern primary mirrors are passive mirrors with active supports. For example, the Multiple Mirror Telescope's primary on Mt. Graham is 6.5 m in diameter, and it's supported by 160 actuators. These actuators can't correct for errors on the order of a few inches: they're spaced too far apart to do this. Instead, they are used to correct for gross astigmatism or trefoil caused by self-weight or wind loading.

pitch A derivative of pine tar that is used in the optics shop. Pitch's most useful property is that it is a *very* viscous liquid. (It is a liquid, yet it shatters if a cylinder of it is dropped on the floor.) This allows it to take the shape of whatever it's placed upon, without any internal stresses. This makes it an ideal candidate for use on polishing tools and for blocking two objects together.

Poisson's ratio, ν A measure of how much a material expands in one axis when a force is exerted along another axis. For example, imagine a 1" rubber cube sitting on a table. If you exert a force on the cube down towards the table, the rubber will squish out in a direction tangent to the table top. The Poisson Ratio quantifies this effect. Steel has a small value of ϵ; rubber has a large value. See Section 2.1.3.

PV Peak-to-valley. This is usually referred to when quoting a linear distance measurement. For example, if one wanted to measure the peak-to-valley height of Mt. McKinley, the result would be $20,320$ feet. This is the distance from the base of the mountain to its peak. This number is useful because it provides a scale of the overall size, but it does not mention anything about any of the many canyons or meadows contained with the measurement. For this purpose, an RMS measurement would be more telling.

PZT Piezo electric transducer. A PZT is a ceramic which changes dimension when a voltage is applied across it.

reaction structure The reaction structure, or support structure, is what provides the MARS mirrors with their stiffness. The role of the support structure is illustrated in Figure 1.3.

rms Root-Mean-Square. For a set of N data points x_i the rms is

$$\sqrt{\frac{\sum_i^N x_i^2}{N}}.$$

rss Root-Sum-Square. For a set of N data points x_i the rss is

$$\sqrt{\sum_i^N x_i^2}.$$

RTV Room Temperature Vulcanizing. RTV commonly refers to **RTV epoxy**, which is a rubbery adhesive.

SAFIR Single Aperture Far Infrared Telescope.

seeing Seeing refers to the optical quality of the atmosphere above a telescope. A site with good seeing means that the atmospheric turbulence above the site is comparably small to other locations on Earth. There is a mathematical quantity that quantifies seeing.

self-weight deflection Self-weight is something that all objects experience when they are subjected to gravity. Self-weight deflection refers to the shape change that occurs due to an object's own weight. For example, Figure 4.2 shows the (exaggerated) self-weight deflection for an I-beam.

shear stiffness The shear stiffness is a quantity that tells how likely a material will be to shear when an outside shear force is exerted upon it. See Equation 3.21.

shell A curved plate.

SIRTF Space Infrared Telescope Facility. The last of NASA's Great Observatories to be launched, the SIRTF telescope was placed in orbit on 24 August 2003. It has since been renamed the Spitzer Space Telescope.

specific stiffness Specific stiffness is E/ρ, where E is Young's modulus and ρ is the mass density (m/V). Ideally, lightweight mirrors should be constructed from something that has a large E (takes lots of stress with little strain) and a low mass density. Large values of specific stiffness are ideal for building lightweight, stiff mirrors.

Spitzer Space Telescope See **SIRTF**.

Steward Observatory/Mirror Lab Steward Observatory is the professional research organization of the University of Arizona's astronomy department.

strain, ϵ A strain is a measure of how something reacts to an outside stress (or pressure). See Equation 2.3.

stress, σ A stress is simply a pressure: it's a force per unit area. See Equation 2.2.

substrate In the context of this work, a substrate refers to the glass (or metal, etc) facesheet that supports the reflective coating. For the Arizona MARS mirrors, the substrate is the glass facesheet shown in Figure 1.3.

TPF Terrestrial Planet Finder.

tpi Threads per inch. A standard machine screw has roughly twenty threads per inch; a higher precision screw typically has 80 threads per inch.

UA The University of Arizona.

ULE Ultra-low Expansion glass. Made by Corning, ULE is a special glass that has a very small (0.4 ppb/^{o} C) coefficient of thermal expansion.

Young's modulus A constant that relates stress exerted to how much something will yield (the strain). Rubber has a small Young's modulus compared to that of steel. See Section 2.1.2.

Index